PHOTONICS INSIGHTS

Advanced manufacturing of dielectric meta-devices

Wenhong Yang,[a] Junxiao Zhou,[b] Din Ping Tsai,[b,c,d,*] and Shumin Xiao[a,e,*]

[a]Key Lab of Micro-Nano Optoelectronic Information System, Ministry of Industry and Information Technology, Guangdong Provincial Key Laboratory of Semiconductor Optoelectronic Materials and Intelligent Photonic Systems, Harbin Institute of Technology, Shenzhen, China
[b]Department of Electrical Engineering, City University of Hong Kong, Hong Kong, China
[c]The State Key Laboratory of Terahertz and Millimeter Waves, City University of Hong Kong, Hong Kong, China
[d]Centre for Biosystems, Neuroscience, and Nanotechnology, City University of Hong Kong, Hong Kong, China
[e]Pengcheng Laboratory, Shenzhen, China

Abstract. Metasurfaces, composed of two-dimensional nanostructures, exhibit remarkable capabilities in shaping wavefronts, encompassing phase, amplitude, and polarization. This unique proficiency heralds a transformative paradigm shift in the domain of next-generation optics and photonics, culminating in the development of flat and ultrathin optical devices. Particularly noteworthy is the all-dielectric-based metasurface, leveraging materials such as titanium dioxide, silicon, gallium arsenide, and silicon nitride, which finds extensive application in the design and implementation of high-performance optical devices, owing to its notable advantages, including a high refractive index, low ohmic loss, and cost-effectiveness. Furthermore, the remarkable growth in nanofabrication technologies allows for the exploration of new methods in metasurface fabrication, especially through wafer-scale nanofabrication technologies, thereby facilitating the realization of commercial applications for metasurfaces. This review provides a comprehensive overview of the latest advancements in state-of-the-art fabrication technologies in dielectric metasurface areas. These technologies, including standard nanolithography [e.g., electron beam lithography (EBL) and focused ion beam (FIB) lithography], advanced nanolithography (e.g., grayscale and scanning probe lithography), and large-scale nanolithography [e.g., nanoimprint and deep ultraviolet (DUV) lithography], are utilized to fabricate high-resolution, high-aspect-ratio, flexible, multilayer, slanted, and wafer-scale all-dielectric metasurfaces with intricate nanostructures. Ultimately, we conclude with a perspective on current cutting-edge nanofabrication technologies.

Keywords: dielectric; meta-devices; meta-optics; metasurface; nanofabrication; nanotechnology; nanophotonics; large/wafer-scale nanofabrication.

Received Apr. 26, 2024; revised manuscript received Jun. 7, 2024; accepted Jun. 11, 2024; published online Jun. 30, 2024.

© The Authors. Published by CLP and SPIE under a Creative Commons Attribution 4.0 International License. Distribution or reproduction of this work in whole or in part requires full attribution of the original publication, including its DOI.

[DOI: 10.3788/PI.2024.R04]

1 Introduction

Nanofabrication technology is an exhilarating and swiftly advancing area that can produce exceedingly diminutive structures, operating at scales ranging from 1 to 100 nm. This innovative technology has brought about a revolution in the field of nanophotonics, particularly within the realm of metasurfaces. Metasurfaces are two-dimensional (2D) metamaterials that consist of ultrathin subwavelength structure arrays that are so-called meta-atoms[1–10]. Through specific design and artificial arrangement, metasurfaces demonstrate a remarkable ability to manipulate the wavelength, amplitude, phase, and polarization of electromagnetic waves. This versatility finds applications in diverse fields such as metalenses[11–20], metaholograms[21–26], structural colors[27–34], optical vortex generation[35–40], spectrometers[41–44], imaging[44–47], sensing[48–55], and beam manipulation[56–61]. Metasurfaces can be broadly categorized into two types based on the materials of their unit cells: plasmonic[62,63] and dielectric [64] metasurfaces. Initial studies predominantly

*Address all correspondence to Shumin Xiao, shumin.xiao@hit.edu.cn, Din Ping Tsai dptsai@cityu.edu.hk

focused on plasmonic metasurfaces, consisting of planar arrays of metallic nanoantennas, typically made of noble metals like gold or silver. These structures exhibit plasmonic resonance when illuminated, driven by the collective oscillation of free electrons at the metal–dielectric interface, known as localized surface plasmon resonance (LSPR)[65], wherein the electromagnetic field couples to the electron plasma of a conductor. However, the plasmonics faces inherent ohmic losses associated with the free electron response, and incompatibility with complementary metal–oxide semiconductor (CMOS) fabrication processes poses a significant challenge, limiting both the optical device's working and fabrication efficiency, which is a determining factor for whether metasurfaces can achieve further application. To address this limitation, the all-dielectric resonator has emerged as a promising alternative. Comprising high refractive index and low-loss dielectric nanoblocks, such as titanium dioxide (TiO_2)[66–72], silicon (Si)[73,74], silicon nitride (Si_3N_4)[75–77], and gallium arsenide (GaAs)[78,79], all-dielectric metasurfaces can support electric and magnetic multipole modes based on Mie resonance theory with negligible absorption loss. This characteristic enables efficient manipulation of optical responses and the creation of high-efficiency photonic devices. The Mie resonance in dielectric meta-atoms depends on the material and dimensions, allowing convenient engineering of scattering characteristics[80]. The tuning of resonances and their spectral positions is achieved by finely tailoring the geometry parameters of nanoparticles. Therefore, the tolerance and roughness control in nanofabrication play a crucial role in determining the performance of dielectric optical devices, especially in achieving resonances with ultranarrow linewidths, such as bound states in the continuum (BICs)[81–87].

For the precise production of dielectric metasurface nanoblocks, various established nanofabrication techniques have been proposed, such as electron beam lithography (EBL)[88–91], focused ion beam (FIB) lithography[92], and laser-based nanomanufacturing[93], among others. While these advancements are exciting, the challenge of fast, large-scale, and cost-effective metasurface fabrication remains[94]. The low cost of mass-production techniques is essential for bringing metasurfaces from laboratories to our daily lives. Efforts have been directed toward reducing the cost and enhancing the throughput of dielectric metasurfaces through methods such as nanoimprinting[95–97], molecular self-assembly[98], roll-to-roll[99], and deep ultraviolet (DUV) lithography[100] processes. It is noteworthy that novel nanofabrication techniques have facilitated groundbreaking discoveries, as evidenced by the development of high-aspect-ratio[101], flexible[102], multilayer[103], and slanted nanostructures[104]. Numerous reviews have been published to summarize the realm of all-dielectric metasurfaces and their corresponding nanofabrication technologies. These include reviews on the development of dielectric metasurfaces[64], the fundamentals and applications of dielectric metasurfaces[80,105–107], and the fabrication of metasurfaces[108,109] encompassing both plasmonic and dielectric materials, among others. However, the majority of these works primarily review fundamental principles and common manufacturing processes, often overlooking the critical aspect of advanced fabrication techniques for dielectric metasurfaces. Given that dielectric metasurfaces are considered one of the most promising platforms for advancing meta-optics toward commercialization, a specific review focusing on the advanced manufacturing of dielectric meta-devices is both necessary and timely. This review comprehensively explores recent progress in cutting-edge nanofabrication technologies for all-dielectric metasurfaces, covering standard nanolithography techniques to extreme nanofabrication. In Secs. 1 and 2, we present diagrams illustrating the fabrication and properties of dielectric materials (Figs. 1 and 2). Moving to Sec. 3 we delve into the standard nanolithography method specific to dielectric materials and additionally introduce advanced and scalable nanofabrication techniques. Section 4 lists recent advancements in extreme fabrication techniques, leading to novel physical discoveries and applications. Finally, the article concludes in Sec. 5 with a perspective on the challenges and future directions in nanofabrication techniques for dielectric metasurfaces.

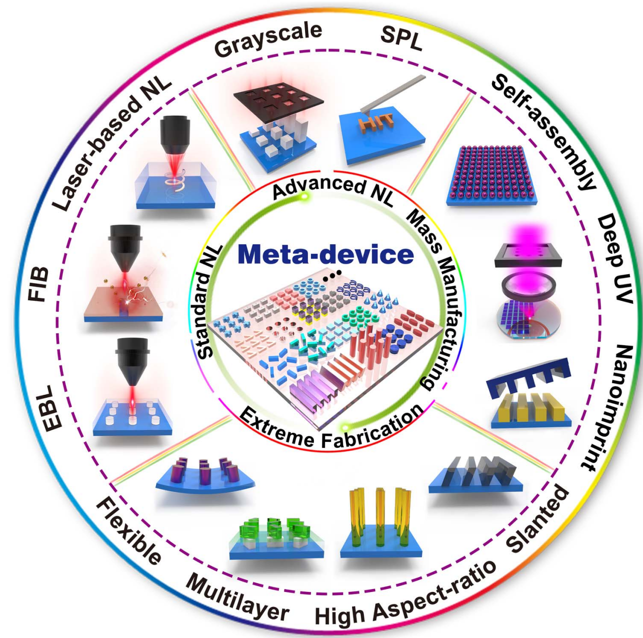

Fig. 1 The schematic diagram illustrates typical fabrication techniques for all-dielectric metasurfaces, categorized into four parts. The first part encompasses standard nanolithography (NL) methods, specifically EBL, FIB lithography, and laser-based nanomanufacturing. The second part shows advanced NL techniques, such as grayscale lithography and scanning probe lithography (SPL). The third part explores mass manufacturing technologies, including molecular self-assembly, DUV lithography, and nanoimprint lithography. The fourth part delves into extreme nanofabrication techniques tailored for high-aspect-ratio, slanted, flexible, and multilayer nanostructures, respectively.

2 Resonant in All-Dielectric Metasurface

Commencing from Mie scattering as a starting point, ongoing research into the prevalent scattering phenomena in artificial micro-nanostructures has been actively advancing. The physics of light scattered by sub-wavelength particles typically involves Rayleigh scattering or surface plasmon interactions. These interactions are solely contingent on the properties of the material and not on the particle's shape. In contrast, Mie resonance, also known as morphology-related resonance, depends on the particle's size and geometric shape[110]. Particularly for dielectric nanodisks, incident light induces a substantial electromagnetic response. Specifically, the incident light couples with the circular displacement current of the electric field, leading to strong

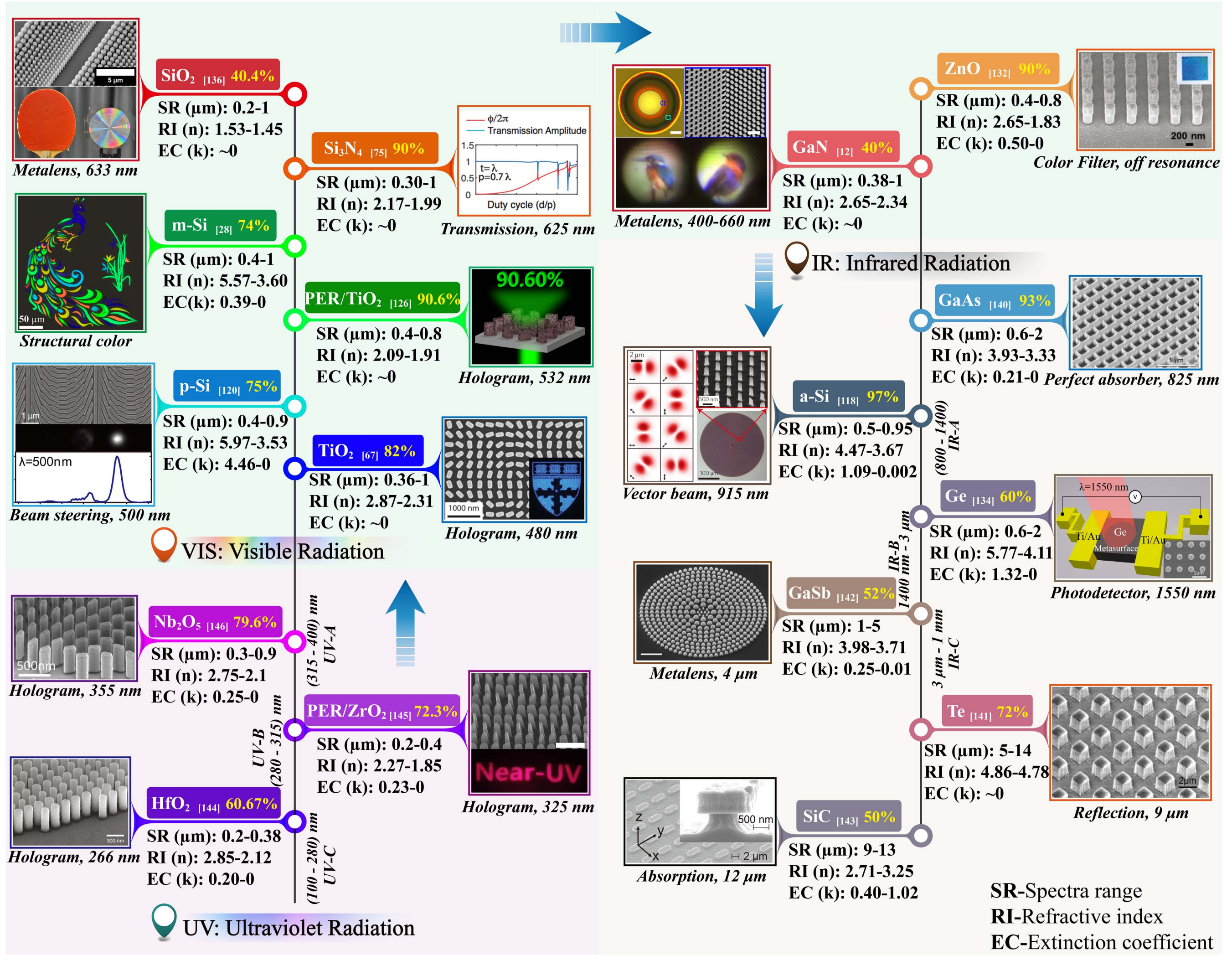

Fig. 2 Comparison of the optical properties of different dielectric materials and their high-efficiency applications across the UV to IR spectrum.

magnetic dipole (MD) resonance. Additionally, the wavelength of incident light must be comparable to the spatial dimensions of the particle, i.e., $2R \approx \lambda_{\mathrm{MD}}/n$, where n is the refractive index of the nanomaterial, R is the radius of the nanodisk, and λ is the wavelength of resonance. Hence, materials exhibiting a high refractive index possess the potential to reduce the dimensions of optical devices. The realization of MD resonance within the visible spectrum can be achieved by employing high-refractive-index nanoparticles with dimensions ranging from 100 to 200 nm. Electric dipole and MD moments are excited along the corresponding components of the incident field and are mutually perpendicular.

To accurately describe and thoroughly explain the phenomenon of uniform particle scattering equivalent to the wavelength, the Mie solution is employed to analyze the scattering field in the near-field and far-field regions, as well as the total scattering cross-section (C_{sca}). C_{sca} can be expanded into an infinite series of spherical harmonics (Mie expansion):

$$C_{\mathrm{sca}} = \frac{2\pi}{k^2}\sum_{m}^{\infty}(2m+1)(|a_m|^2 + |b_m|^2),$$

where a_m and b_m are the Mie coefficients for the mth order electric and magnetic multipole modes, respectively, and k is the wave number. Electric dipole (ED, a_1^2), magnetic dipole (MD, b_1^2), electric quadrupole (EQ, a_2^2), and magnetic quadrupole (MQ, b_2^2) constitute the first four terms in the Mie expansion.

Through the engineering of mode coupling in multiple dipole modes, the spectral overlap of various Mie modes can be harnessed to manipulate electromagnetic waves, enhance light–matter interaction, and control the directionality of the scattered field at a subwavelength scale[105]. This includes both single and arrays of dielectric structures, as well as hybrid dielectric–metallic systems that can support Mie resonance-based leak modes (also known as quasi-normal modes)[111,112], waveguide modes[113–115], and lattice modes[116,117], thereby governing the optical properties of the metasystem. These types of resonances directly depend on the refractive index. Therefore, it is crucial to select the right material with suitable optical properties at desired wavelength ranges. The optical properties of the constituent materials are characterized by the complex refractive index as $\tilde{n} = n + ik$. The high refractive index ensures the strong confinement of incident light in the nano resonators and a full

manipulation of the wavefront. The extensive library of dielectrics, such as silicon (Si), gallium arsenide (GaAs), gallium nitride (GaN), and titanium dioxide (TiO_2), among others, empowers researchers and scientists to design high-performance metaphotonics (also known as meta-optics). These devices feature well-fabricated nanostructures capable of operating across a wide range of wavelengths, from ultraviolet (UV) to infrared (IR), thereby demonstrating attractive mechanisms and promising applications, as illustrated in Fig. 2. In the visible to near-IR (NIR) spectra, silicon [amorphous silicon (a-Si), monocrystalline (m-Si), and polycrystalline (p-Si)] has emerged as the predominant dielectric material. Its popularity stems not only from extensive use in the semiconductor industry but also due to its mature fabrication process and compatibility with modern CMOS technologies, aligning seamlessly with mass-manufacturability requirements. Silicon-based optical devices exhibit exceptional stability, leveraging their high refractive index and low losses in the visible range, near-zero losses in the IR region, and widespread application in meta-device design[73,118–120]. Despite efficiency challenges, particularly in the short wavelength range (around 250–450 nm), sophisticated nanostructure designs, such as adding a refractive index matching layer, offer the potential to mitigate losses and enhance performance[28,121]. TiO_2 stands out as another promising material, displaying intriguing characteristics of a high refractive index and negligible optical losses in the visible to NIR range. It has found extensive use in high-efficiency all-dielectric metasurface design[67,101,122–125]. TiO_2 is a CMOS-compatible material capable of addressing the absorption limitations of silicon, essential for cost-effective nanofabrication. Recent developments, such as synthesizing UV-curable polymer resist (PER) and TiO_2 nanoparticles, have resulted in a nanoparticle-embedded resist exhibiting optical properties similar to pure TiO_2. Combined with nanoimprinting lithography, metasurfaces can be rapidly replicated from a master mold directly onto a substrate[126–128]. Other materials, including silicon nitride (Si_3N_4)[75,129], GaN[11,2,130,131], zinc oxide (ZnO)[132,133], germanium (Ge)[134,135], silicon dioxide (SiO_2)[136–138], and GaAs[139-140], are also attractive options widely used in visible to NIR applications. For middle-IR applications, narrowband semiconductors like tellurium (Te)[141], gallium antimonide (GaSb)[142], and polar crystals such as silicon carbide (SiC)[143] have already been implemented for all-dielectric meta-devices operating with Mie resonances. Furthermore, the UV range presents an intriguing field in nanophotonics, with the development of novel materials such as hafnium oxide (HfO_2)[144], zirconium dioxide (ZrO_2)[145], and niobium pentoxide (Nb_2O_5)[146]. These materials enable metasurfaces to contribute to the UV region, demonstrating high efficiency, ranging from 60% to 80%, as demonstrated by metahologram generation. Therefore, to achieve the intended optical function, it is crucial to select a dielectric material with suitable optical parameters in the UV to IR region and an available production method.

3 Nanofabrication Techniques of All-Dielectric Metasurfaces

The creation of metasurfaces is primarily grounded in lithography, a process that can be divided into two cases, as depicted in Fig. 3. The predetermined pattern of metasurfaces is initially transferred to a resist (photosensitive polymer) through exposure to specific energy radiation, such as photons, electrons, or ions, followed by the development process. Subsequently, the organized resist pattern serves as either the hard mask or the inverse pattern for the subsequent etching (left process flow in Fig. 3) or deposition processes (right process flow in Fig. 3). Depending on the dielectric material and specific application, various lithography techniques can be employed in the fabrication process. In this section, we provide a comprehensive summary of recent key lithography nanofabrication techniques for the fabrication of all-dielectric metasurfaces. This section will categorize these techniques into three types: standard nanolithography, advanced nanolithography, and large-scale nanolithography. While each technology comes with its inherent advantages and disadvantages, the overarching goal is to attain superior results, focusing on aspects such as high resolution, high speed, cost-effectiveness, and mass manufacture.

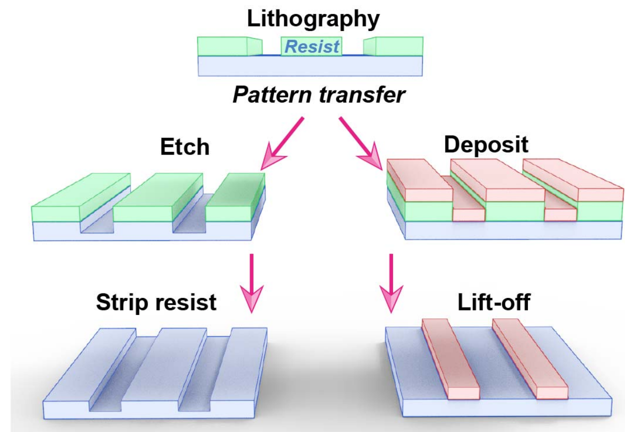

Fig. 3 The illustration clarifies the pattern transfer through the lithography process. Following the exposure of the resist film to a specific radiation source (such as photons, electrons, or ions), the intended pattern is transferred to the resist film through the developer. Subsequently, the pattern is transposed onto the dielectric materials, encompassing two cases. In the first case, the pattern is transferred through etching techniques; after the etching process, the final step involves stripping the resist through chemical or physical methods. In the second case, the dielectric material is deposited into the exposed and developed areas, followed by the lift-off process.

3.1 Standard nanolithography techniques

The standard nanolithography process employed by the semiconductor industry incorporates EBL and FIB lithography[147,148]. These methods have found extensive use in dielectric fabrication, as illustrated in Figs. 1 and 2, marking a significant milestone in its evolution. In response to the challenges of cost-prohibitive and time-consuming processes over large scales, laser lithography has undergone substantial development. Table 1 presents a comparative analysis of these nanofabrication technologies.

3.1.1 Electron beam lithography

EBL, a pivotal nanofabrication technique, precisely sculpts the electron beam resist at the nanoscale based on a computer-generated pattern. Acknowledged for its remarkable properties—high resolution, extensive design flexibility, and reliable

Table 1 The Comparison of Three Main Standard Nanolithography Technologies

Feature	Electron Beam Lithography	Focused Ion Beam Lithography	Laser Lithography
Resolution	Extremely High (Sub-nanometer)	High (Nanometer to Sub-nanometer)	High (Nanometer to Micrometer)
Speed	Slow	Slow	Moderate to high
Material Selectivity	Good Material Selectivity	Good Material Selectivity	Material Dependent
Throughput (wafer-scale)	Limited	Limited	Limited-Moderate
Cost	High	Moderate	Moderate to low
Complexity of Setup	Complex	Moderate	Moderate
Dimension/Shape Design	Ideal for Complex Geometries and Small Features	Suitable for Planar Structures	Suitable for Complex 3D Structures

repeatability—EBL has emerged as the predominant technique for dielectric fabrication in recent decades[149]. Commercial EBL systems, typically operating within the 30 to 100 KeV energy range, are well-suited for fabricating sub-wavelength nanoantennas. The transfer techniques following exposure and development vary based on the specific dielectric material design and application. They are categorized into the bottom-up or top-down approach, with corresponding etching or lift-off processes. These approaches are grounded in film deposition methods, encompassing electron beam (E-beam) evaporation, sputtering deposition, chemical vapor deposition, and atomic layer deposition (ALD). The fundamental EBL process commences with the spin coating of a radiation-sensitive resist onto a designated substrate. The pattern is then delineated into the resist through high-energy electron radiation. In positive-type resist, the exposed area becomes soluble during development, while in negative-type resist, a cross-linking reaction in the exposed region renders it insoluble, and the background dissolves away. In the bottom-up approach, film deposition precedes lift-off to construct desired structures. Conversely, the top-down approach initiates with film deposition to achieve the dielectric layer at the desired thickness on the substrate before engaging in the EBL process, culminating the entire procedure with etching.

In the standard EBL fabrication procedure depicted in Fig. 4(a), monocrystalline silicon metasurfaces are crafted using the EBL technique, followed by a metal lift-off and dielectric etching process. Among these two approaches, the lift-off method utilizes a hard mask constructed with Cr, serving as a protector for subsequent etching. Yang *et al.* conducted experiments on commercially available silicon on the sapphire wafer, fabricating nanodisks with varying parameters of diameter/period arrays, showcasing high-performance structural color[28]. This approach exhibits advantages in terms of a broad gamut, high saturation, brightness, and resolution. The high-resolution scanning electron microscope (SEM) images in Fig. 4(b) reveal a roughness smaller than 10 nm. Due to its precise control over geometric precision, EBL stands out as the most widely used process for defining functional nanostructures with unique shapes. As depicted in Fig. 4(c), Gao *et al.* proposed C-shaped Si nanoantennas, demonstrating high-efficiency cyan and blue third-harmonic generation (THG) holograms[22]. This efficiency is achieved by introducing abrupt phase changes from 0 to 2π to the C-elements, precisely controlled by the outer radius, inner radius, and opening angle. The mature and highly reproducible CMOS-compatible fabrication technology of silicon allows for the efficient production of nanostructures, both horizontally and vertically. Figure 4(d) illustrates the smooth sidewall of silicon rectangle pillars, with an angle of nearly 90° in the vertical direction after reactive ion etching (RIE)[150]. This showcases the successful demonstration of a tunable full-color vectorial hologram with metamolecules.

However, due to the persistent ohmic losses in silicon materials[152–154], especially at shorter wavelengths, TiO_2 has emerged as a promising alternative in recent years and holds the potential to replace silicon in the field of dielectric metasurfaces[155–157]. TiO_2 boasts a transparency window in the visible spectrum and a sufficiently high refractive index (2.87–2.31) for robust light–matter interactions. In the initial stages, Capasso's group demonstrated high-efficiency TiO_2 metasurfaces in the form of holograms for red, green, and blue wavelengths. The fabrication procedure, as illustrated in Fig. 4(e), involves using EBL to form reverse nanofins in resist, filling the exposed region with amorphous TiO_2 through ALD, and then subjecting it to blanket RIE[67]. The remaining electron beam resist is subsequently stripped, resulting in TiO_2 nanofins with a roughness of less than 1 nm, as shown in the top image in Fig. 4(f). Additionally, they fabricated metalenses for the visible range [bottom image in Fig. 4(f)] with efficiencies as high as 86%[15]. The geometrical parameters of the metalenses, defined by the resist, lead to the attainment of nearly 90° vertical sidewalls. However, current TiO_2 metasurface fabrication techniques heavily rely on the ALD method, which is relatively slow and restricts thickness to values below 600 nm. In recent years, high-quality TiO_2 films have been successfully formed using E-beam evaporation. In comparison to ALD, E-beam evaporation has proven to be more cost- and time-efficient[158]. Xiao's group showcased the application of TiO_2 metasurfaces in dielectric full-color printing through EBL and a straightforward lift-off process, as illustrated in Fig. 4(g)[30]. The nanostructures were constructed using E-beam evaporation to fill TiO_2 into the reverse model. After a successful transfer of the reversed nanostructures onto the TiO_2 film, TiO_2 metasurfaces were ultimately formed through the lift-off process. The roughness of the TiO_2 film measured at 0.66 nm signifies the achievement of an ultra-smooth surface. However, the lift-off method typically struggles to maintain perfect geometry due to the proximity effect during EBL. The cross-section of each subunit appears as a trapezoid rather than a rectangle in the vertical direction, as seen in Fig. 4(g). To address this issue, the researchers developed RIE technology for

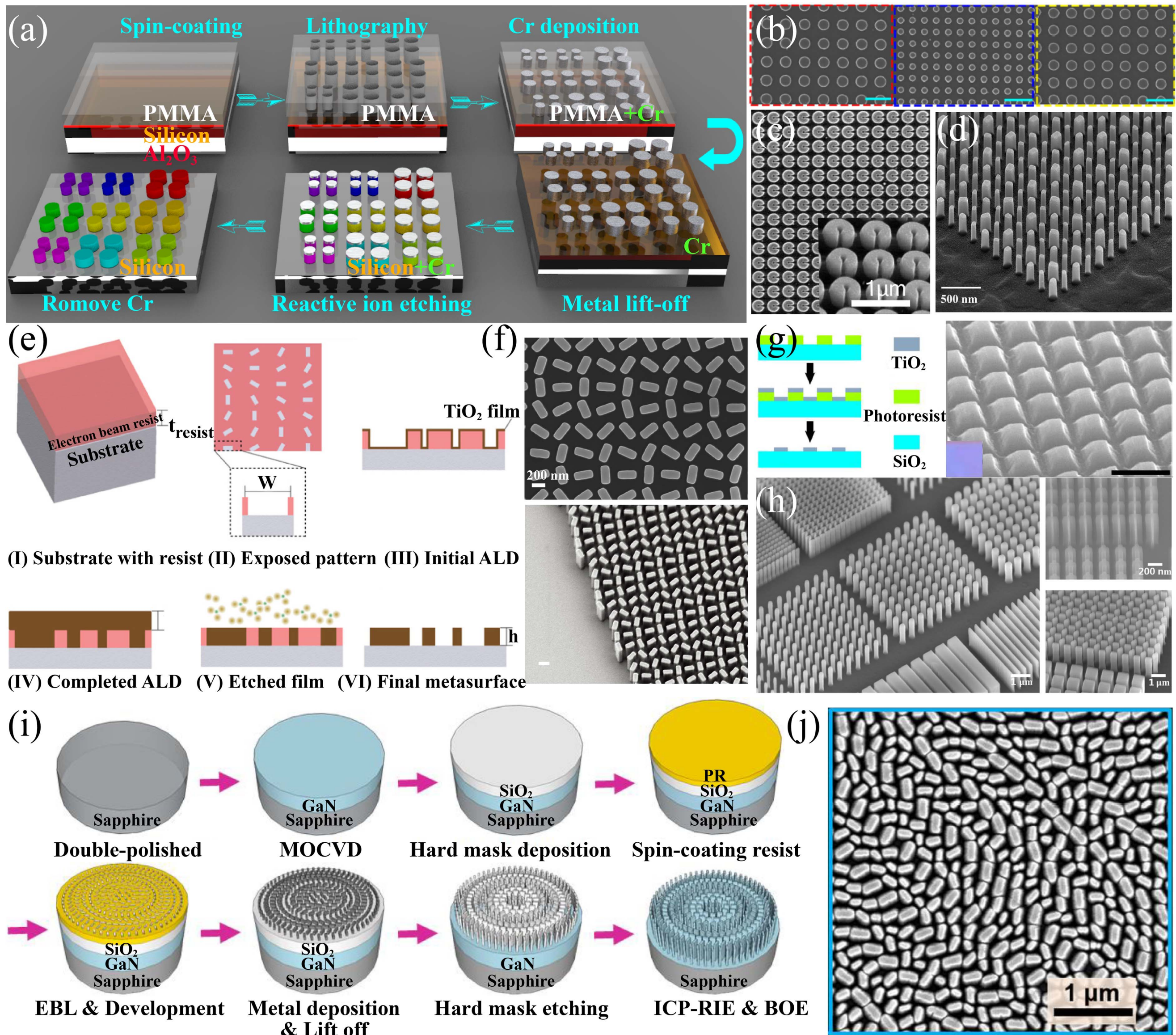

Fig. 4 The utilization of EBL in the fabrication of all-dielectric metasurfaces. (a) The schematic depicts the fabrication process of silicon-based structural color utilizing EBL.[28] Initially, a PMMA resist film is spin-coated onto the silicon-coated sapphire substrate. Subsequently, the resist is exposed to an electron beam and developed to form PMMA nanostructures. The sample is then transferred to an E-beam evaporator and coated directly with Cr films. After a lift-off process involving immersion in acetone, the PMMA is removed, and the nanostructures are effectively transferred to Cr. The silicon is later etched away using reactive ion etching with CHF_3 and SF_6 gases. Finally, Si metasurfaces are obtained by immersing the sample in chromium etchant. (b) The top-view SEM image of silicon nanodisks for color printing. The diameters and periods of these three colors are 170/320, 90/200, and 160/300 nm, respectively. The scale bar is 500 nm.[28] (c) The top-view SEM image displays the C-shaped silicon nanoantenna from nonlinear holographic all-dielectric metasurfaces. The insets include zoomed-in images showing high-resolution side-view SEM images.[22] (d) The SEM image with a tilted view of 45° presents the fabricated silicon rectangle pillars used for tunable full-color vectorial meta-holography.[150] (e) Fabrication process of high-efficiency TiO_2 metasurfaces[67]: (I) Application of the resist on fused silica. (II) Recording of the reversed metasurface pattern into the resist using EBL. (III) Deposition of TiO_2 through atomic layer deposition (ALD) into the exposed substrate. (IV) Formation of the final thick TiO_2 film, exceeding half the width of the maximum feature size after ALD. (V) Removal of residual TiO_2 and resist via reactive ion etching with a mixture of Cl_2 and BCl_3 ions. (VI) Completion of the final metasurface after eliminating remaining resist. (f) The top and side-view SEM image of fabricated ALD-based TiO_2 metalenses at visible wavelengths (scale

bar, 300 nm)[15]. (g) The fabrication process (left) of the TiO_2 metasurface with lift-off technology[30]: Top: Patterning of the photoresist with EBL. Middle: Formation of TiO_2 film through electron-beam evaporation technology. Bottom: Elimination of the photoresist through lift-off. Corresponding SEM image (right) of one metasurface (scale bar, 500 nm). (h) Tilt view SEM images of the etched TiO_2 nanostructures, including circular pillars, crosses, rectangle pillars, crosses, and rectangle pillars.[101] (i) Fabrication flow of the GaN-based structures for a broadband achromatic metalens in the visible spectra.[12] (j) SEM image of the on-axis focusing GaN-based metalens, applied in CMOS image sensor.[151]

the TiO_2 film fabricated by E-beam evaporation. Figure 4(h) demonstrates that the nanopillars exhibit nearly perfect vertical sidewalls, with a measured tilt angle of sidewalls around 89°–90°, effectively replacing the lift-off method[101]. Apart from TiO_2, GaN stands out as another promising dielectric material with a high refractive index and negligible loss in the visible range[159]. It can be deposited using chemical vapor deposition. Tsai's group has pioneered a top-down approach to creating a GaN metalens, as depicted in Fig. 4(i)[12]. Employing integrated resonance unit elements within a metasurface framework, the successful demonstration of a flawless achromatic lens has been achieved[12]. The fabrication process initiates with EBL, followed by an etching process to shape the nanostructures. Figure 4(j) provides a top-view SEM image of a GaN metalens after the etching process[151]. While EBL possesses extraordinary advantages and has demonstrated numerous new concepts in metaphotonics, it is worth noting that it still grapples with disadvantages. These include limited area coverage, high expenses, and a complicated, time-consuming process. Additionally, there are costs associated with the purchase and maintenance of the EBL system.

3.1.2 Focused ion beam lithography

FIB lithography stands as a potent and versatile instrument based on the intricate interactions between ions and solids. With capabilities extending beyond mere nanofabrication, FIB integrates functions for both fabrication and characterization. The ion beam, typically derived from a liquid metal tip such as gallium (Ga), replaces electrons to directly pattern features onto the target film without the requirement of a photomask[160,161]. Through selective material removal or deposition, FIB enables the precise fabrication of planar micro/nano or three-dimensional (3D) structures, employing either the bottom-up or top-down approach[162–164]. These effects emerge from the dynamic exchanges of energy and momentum between the incident ions and target atoms. FIB techniques are analogous to SEM, allowing for simultaneous milling and observation of the surface in the work area, a configuration known as the dual-beam system. It has become one of the most advanced fabrication platforms for dielectric metasurfaces.

Garg *et al.* utilized FIB for direct milling of nanoholes on a silicon substrate, showcasing a wide color palette achieved through variations in nanohole diameter. Due to the Gaussian profile of the Ga ion beam, the nanoholes exhibited a tapered morphology, as depicted in the inset and bottom SEM images in Fig. 5(a)[165]. In comparison to alternative lithography techniques for color generation, the FIB process is notably simpler, requiring only a single step.

In-depth exploration into the sophisticated 3D structures using FIB etching has been undertaken by Gorkunov *et al*. The researchers engineered a chiral, 4-fold rotationally symmetric monocrystalline silicon metasurface on sapphire through precise digital FIB patterning, as illustrated in Fig. 5(b)[166]. This meticulously crafted metasurface demonstrates exceptional transparency within the visible spectrum while concurrently manifesting robust optical chirality. Moreover, FIB technology finds application in the fabrication of all-dielectric phase-change materials. Illustrated in Fig. 5(c), a nanograting array is precisely milled by FIB onto the phase-change medium, germanium antimony telluride (GST)[167]. This method attains high-quality resonance and optical switchable all-dielectric metasurfaces in the NIR spectrum. Due to the FIB's independence from material selectivity, it extends beyond the fabrication of dielectric materials from the visible to NIR region[173,174], enabling the fabrication of materials in the UV region, such as ZnO, as demonstrated by FIB in Fig. 5(d) for the nonlinear optical generation of vacuum UV light at a wavelength of 197 nm[168]. Moreover, the FIB not only demonstrates proficiency in handling single-layer dielectric films but also exhibits the capability to etch multilayer structures, as depicted in Fig. 5(f)[170]. In this instance, an Nb_2O_5 layer is interposed between two SiO_2 cladding layers to form a symmetric slab waveguide design. The creation of a high-quality structure is achieved through optimized FIB parameters, including the ion beam current, area dose, and a number of process loops, as illustrated in the SEM image on the right side of Fig. 5(f). However, deviations from optimal parameters result in increased surface roughness and deeper milling holes than desired, as evidenced in the inset of Fig. 5(f). It is noteworthy that FIB nanofabrication has emerged as a crucial and extensively employed technical tool in the production of 3D nanostructures and devices. Researchers have illustrated free-standing 3D bilayer structures fabricated through FIB, as depicted in the SEM images in Figs. 5(e), 5(g), and 5(h), respectively, showcasing the nano-cantilevers (polycrystalline silicon/indium tin oxide)[169], self-rolled multilayer metasurfaces (SiO_2/Au)[171], and 3D Archimedean spiral chiral structures (Si_3N_4/Au)[172], and they demonstrated the application of optical modulation. While FIB milling is the primary method for defining dielectric nanostructures, particularly the nanoholes in thick films, due to its maskless and resistless advantages, it comes with certain limitations. These include high cost, extremely low throughput, and poor geometric precision control caused by the redeposition effect during milling. Additionally, there are aspect ratio limitations and the potential for sample damage.

3.1.3 Laser-based nanomanufacturing

In comparison to EBL and FIB, laser-based nanomanufacturing distinguishes itself as a versatile and standard tool for mask-free fabrication techniques. It involves the utilization of lasers to selectively remove or modify material on a substrate, enabling the creation of intricate patterns or structures at the micro- or nanoscale. This process finds widespread application in the

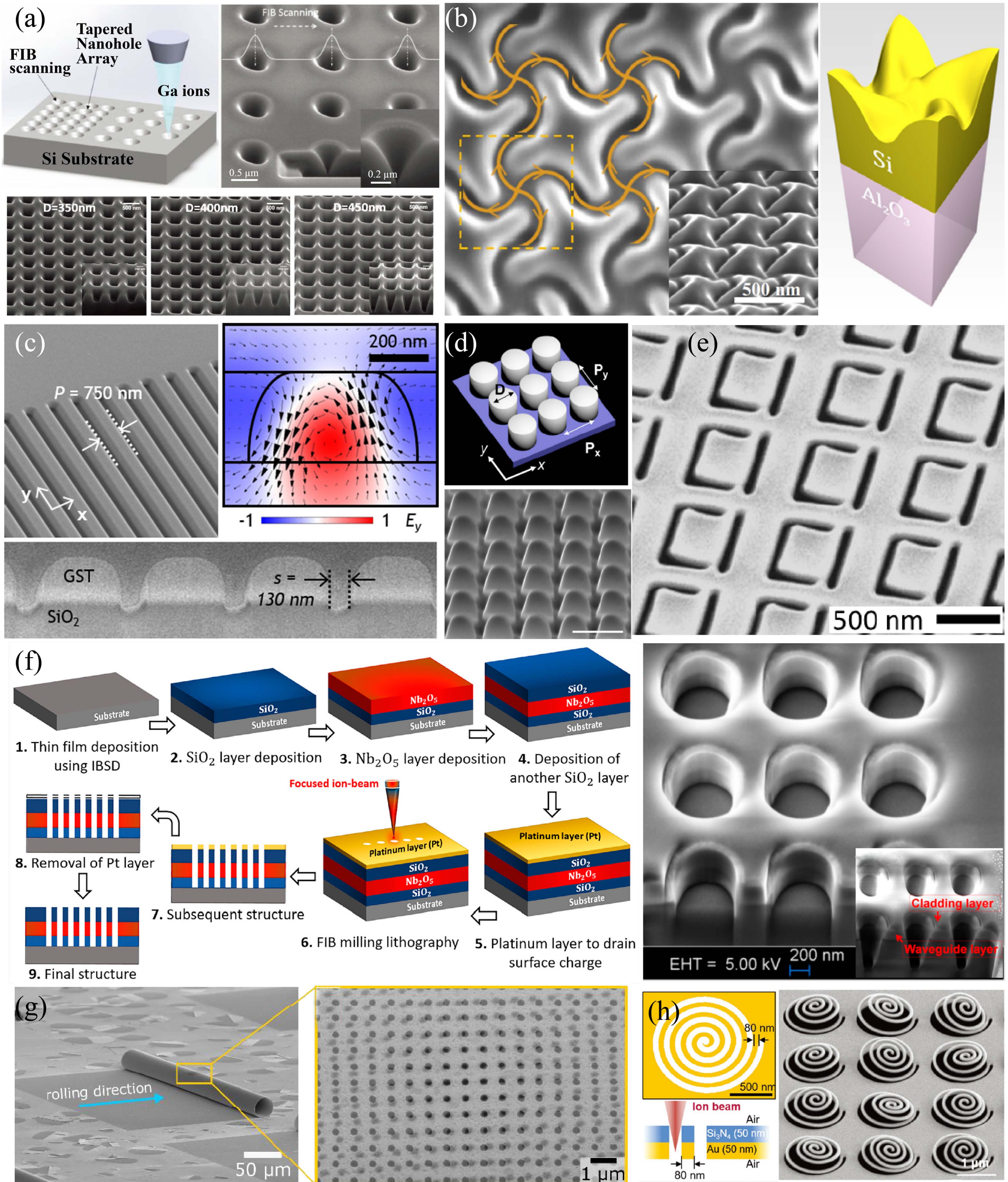

Fig. 5 The utilization of focused ion beam lithography in the fabrication of all-dielectric metasurfaces. (a) FIB gallium ion milling in a Gaussian profile for the direct fabrication of subwavelength nanoholes on silicon through scanning, enabling multicolor generation. The SEM image (right) displays the nanohole, with the corresponding enlarged cross-sectional view as an inset. SEM images (bottom) of color filter arrays, with the right corner in each image showing the cross-section SEM obtained by FIB cutting.[165] (b) Chiral visible light metasurface patterned in monocrystalline silicon on sapphire using FIB. The SEM image on the left includes FIB paths and directions (curved

arrows), and the inset is a tilted SEM image. The right image presents a 3D model of a unit cell.[166] (c) All-dielectric phase-change reconfigurable metasurface consisting of a period grating fabricated by FIB milling in an amorphous $Ge_2Sb_2Te_5$ (GST) film on silica. The SEM images depict tilt and cross-sectional views, shown on the left and bottom, respectively.[167] (d) Schematic of the ZnO metasurface (top) for coherent vacuum ultraviolet light generation. Titled SEM image (bottom) of the FIB milled metasurface with scale bar of 300 nm.[168] (e) The SEM image of a section of a silicon membrane nano-cantilever array from nanomechanically reconfigurable all-dielectric metasurfaces for sub-GHz optical modulation.[169] (f) The process involves the stepwise fabrication of a dielectric slab waveguide photonic crystal, as illustrated on the left. On the right, SEM images provide both a top view and a cross-sectional view of dielectric structures fabricated using FIB milling lithography.[170] (g) Side and top-view SEM images of self-rolled multilayer metasurfaces.[171] (h) The 3D Archimedean spiral chiral metasurface milled by the gallium FIB and tilted SEM (right) images of the freestanding Au/Si_3N_4 bilayer film.[172]

semiconductor industry for producing integrated circuits, microelectromechanical systems, and various nanodevices. Laser-based nanomanufacturing stands out for its high precision, offering an avenue for high-efficiency, cost-effective, and large-scale fabrication. It facilitates the development of extremely small and detailed 3D optical features. Different variations of laser-based lithography exist, including techniques like laser interference lithography (LIL)[175,176] and laser direct writing (LDW)[138,177–182], each with its specific advantages and applications. In this section, we delve into the recent advancements in LIL and LDW for dielectric metasurface fabrication. We explore the capabilities of LDW technology, encompassing laser-induced techniques[137,183,184], laser melting or ablating[185–188], and two-photon LDW[189–197].

LIL is emerging as an innovative nano-patterning method without using a mask. Its prominence stems from its higher efficiency compared to EBL or FIB technology, coupled with a wide workspace and low cost. In LIL, two or more coherent light beams incident from different directions overlap on the photoresist layer, creating interference patterns. The control of these patterns is achieved through parameters such as the exposure dosage, development time, light wavelength, and angle of incident beams. Furthermore, laser interference beams with high-power pulses can directly process the material surface, relying on photothermal or photochemical mechanisms. In Fig. 6(a), the interference patterns of light intensity distribution with 2, 3, 4, and 6 overlapping beams are revealed[198]. The simplest scenario involves the interference of two beams, where beams with the same phase and polarization direction are symmetrical, sharing the same angle (θ) and azimuthal angles (φ). In other instances, the overlap of 3 and 6 beams results in periodic structures arranged in a triangular lattice but with different periods. Particularly noteworthy is the interference pattern generated by the overlap of 4 beams, yielding a square array of intensity maxima. Leveraging this technology, researchers have devised various methods for constructing dielectric nanostructures. Chen *et al.* reported the fabrication of a 2D diffraction HfO_2 grating designed for achieving polarization-independent high-efficiency properties. This structure was created through twice orthogonal exposures by LIL, where two coherent laser beams overlapped in a negative-type photoresist. Subsequent to this, ion-beam etching technology was employed, as depicted in the SEM image in Fig. 6(b)[199]. Using the same procedures at positive photoresist, upon removal of the unexposed material, the pattern will change geometry from a nanodisk to a nanohole. Seo *et al.* introduced a large-area printed silicon hole array fabricated through LIL on a silicon-on-insulator (SOI) wafer designed for broadband reflectors. The corresponding SEM images are depicted in Fig. 6(c)[200]. In addition to transforming the physical structure into the photoresist using the spatial intensity distribution of the interfering beams, Berzinš *et al.* demonstrated the application of single-pulse LIL with a four-beam picosecond laser, featuring a pulse duration of 300 ps and a wavelength of 532 nm [refer to the left image of Fig. 6(d)]. This technique was employed for the direct patterning of an amorphous silicon film into an array of Mie resonators, each a few hundred nanometers in diameter. As illustrated in the middle image of Fig. 6(d)[93], the amorphous silicon film melted when exposed to sufficiently high temperatures, causing the continuous film to break into p-Si-based nanohole structures [Fig. 6(d), right top], referred to as the intermediate regime. If the laser energy density is further increased, it results in the formation of an array of Mie-resonant nanoparticles [Fig. 6(d), right bottom]. Moreover, LIL has faced challenges due to complex setups in multibeam lithography, leading to issues such as sensitivity and limited control over the fabricated structure. To address these concerns, researchers have introduced metasurface-mask-assisted LIL for 3D nanofabrication [left image of Fig. 6(e)]. This approach offers significant flexibility in patterning various periodic structures[201]. The diamond metasurface mask [middle SEM image of Fig. 6(e)] generates different diffraction orders that interfere to achieve a specific desired intensity pattern, ultimately realizing 3D structures in the photoresist [right SEM image of Fig. 6(e)].

Indeed, the use of multiple beams in LIL enables the simultaneous exposure of a large area, making it a faster and more cost-effective method for maskless massively parallel patterning. However, it faces challenges in achieving wafer-scale pattern uniformity and the freedom of pattern geometry, making it less competitive than e-beam lithography in these aspects. The limitations of LIL may stem from the absence of suitable large-area mirrors or other interference optics. Additionally, LIL operates as a batch process with constraints on producing only periodic patterns[202–204].

In contrast to the LIL technique, LDW employs a focused laser beam to directly pattern a substrate, making it well-suited for creating intricate, customized 2D or 3D functional structures. LDW, also known as direct printing and digital writing, operates as a serial process where the laser beam traverses the substrate, selectively exposing or modifying the material. Over the past decade, research efforts have intensified, leading to the development of new applications for dielectric metasurfaces using LDW. This technique utilizes laser melting or ablating, laser-induced methods, and two-photon LDW, providing a

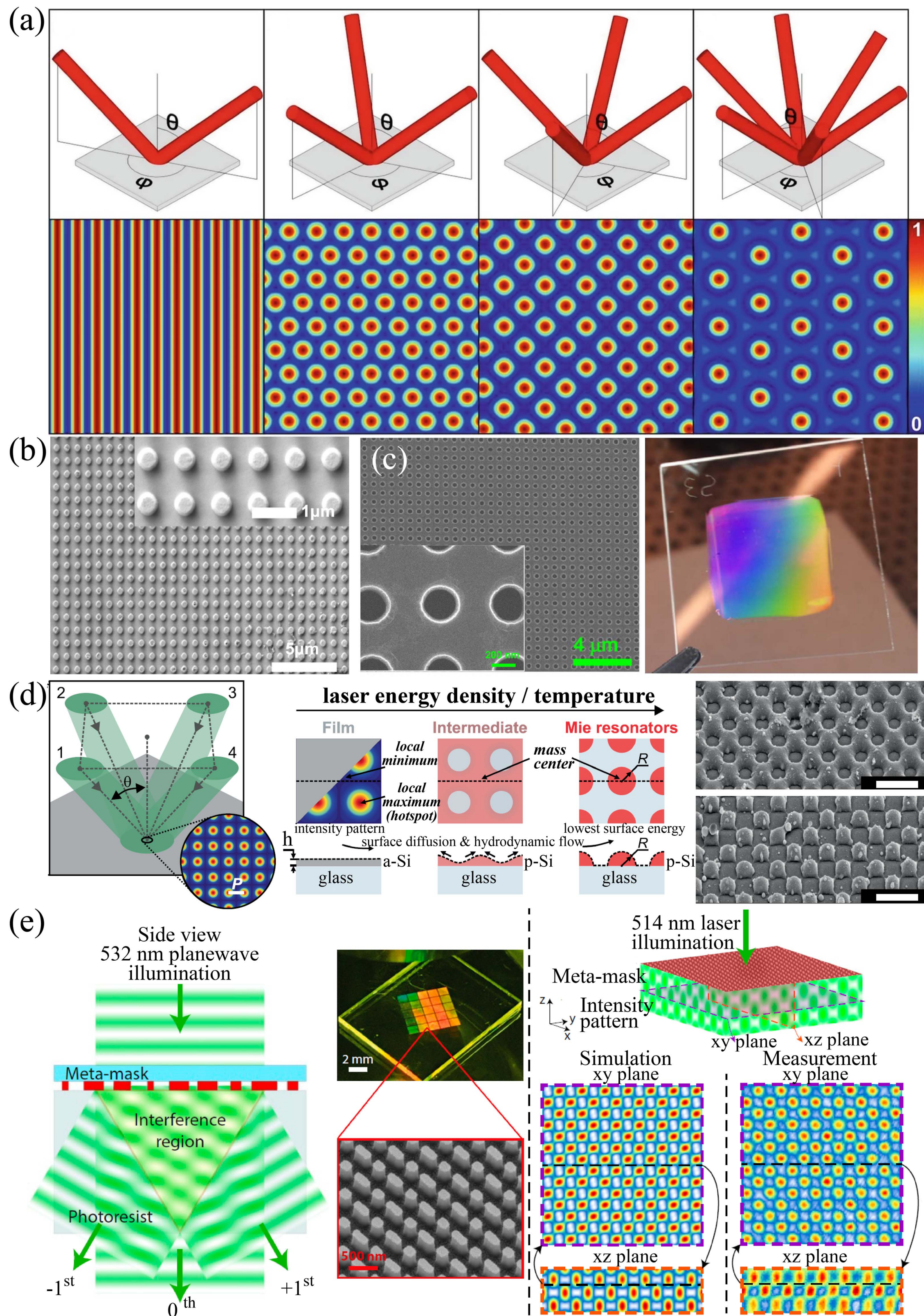

Fig. 6 The utilization of LIL in the fabrication of all-dielectric metasurfaces. (a) Schematic representation (top row) of the interference setup with two, three, four, and six overlapping beams, along with the corresponding light intensity patterns (bottom row)[198]. (b) Top-view SEM of polarization-independent two-dimensional diffraction metal–dielectric grating.[199] (c) SEM image (left) of the silicon nanohole array pattern on SOI substrate and the appearance (right) of large-area printed broadband membrane reflectors by LIL. The inset shows the enlarged SEM image.[200]

(d) Mie-resonant silicon-based metasurfaces via single-pulse LIL: Schematic (left) illustrating the four-beam interference setup and the resulting intensity distribution. Mechanism of silicon transformation (middle) utilizing the interference intensity pattern. Top view (right) SEM images of nanoholes (intermediate state, a-Si) and nanoparticles (Mie resonator state, p-Si) patterned from the Si film, respectively. Scale bar = 1 μm.[93] (e) Metasurface-generated complex 3D optical fields for LIL: Concept (left) of a metamask generating specific diffraction orders to create a desired 3D pattern in the photoresist. Optical image (middle) of the fabricated optimized diamond metamask. Simulated and measured cross-sections (right) of the captured 3D intensity pattern under 514 nm laser illumination.[201]

single-step, lithography-free, and cost-efficient approach for large-scale fabrication of both ordered and disordered structures. Notably, LDW eliminates the need for a clean room and vacuum chambers. Figure 7(a) illustrates the utilization of patterned pulse LDW lithography for the fabrication of metasurfaces comprising sub-wavelength structural units[205]. Employing the pulse LDW system depicted on the left im age of Fig. 7(a), the film undergoes ablation and recasting, forming fine H-shaped units [top right SEM image of Fig. 7(a)] as a result of the scanning of the patterned femtosecond laser (520 nm) achieved by the phase mask on the spatial light modulator (SLM). Subsequently, H-shaped arrays for dielectric metasurfaces are produced, with the etching process utilizing the nanopatterned films as hard masks [bottom image of Fig. 7(a)]. Furthermore, Bochek *et al.* experimentally demonstrated the direct fabrication of the tunable metasurfaces from $Ge_2Sb_2Te_5$ films by exploiting the LDW technique[206]. Figure 7(b) displays the SEM images of the metasurface fabricated by laser (780 nm) inscription on GST films deposited on glass and sapphire substrates. Another one-step LDW fabrication method is based on the laser-induced technique. Figure 7(c) illustrates the application of the laser-induced graphene technique for processing a complex amplitude-modulating metasurface device[207]. A 15 mm × 15 mm metasurface composed of C-shaped graphene antennas can be fabricated by one-step laser writing in 34 s [visible in the photograph and SEM image in Fig. 7(c) on the right]. More complex 3D structures can also be fabricated using the laser-induced method. Lu *et al.* introduced a polarization-directed chiral growth of dielectric materials ($PdO_2 - x$, CdS) induced by a laser with the vector beam[208]. As shown in the right image of Fig. 7(d), the 3D chiral unit of metasurfaces is induced in an inorganic precursor solution under continuous-wave laser irradiation with different vectors.

Another advanced LDW technology two-photon lithography, also referred to as two-photon polymerization, represents an advanced LDW technology for the fabrication of true 3D micro/nanostructures. This method exploits nonlinear photon absorption by photopolymers, enabling the construction of well-defined structures with sub-100-nm resolution. While standard photolithography is commonly employed for 2D structure fabrication, relying on one-photon absorption in a photosensitive medium, the two-photon process involves tightly focusing the beam of an ultra-fast laser inside the volume of a transparent material. This leads to the absorption of two photons, inducing local polymerization. In Fig. 8(a), the true 2D photonic structures or dielectric metasurfaces, along with their inverted counterparts featuring square C4v and hexagonal C6v lattice symmetry, are showcased. These structures are fabricated using two-photon LDW with femtosecond pulses at 780 nm. Experimental results demonstrate a transition from the multi-order diffraction regime characteristic of photonic crystals to the regime where only zero-order diffraction is observed, serving as a distinctive feature of metasurfaces[209]. Zhan *et al.* have introduced a computational inverse design method and implemented the fabrication of arrays of spherical Mie scatterers with the aim of generating 3D optical field patterns through two-photon lithography. The SEM image in Fig. 8(b) illustrates the outcome of this process, showcasing the arrays of scatterers. Notably, these scatterers exhibit a deviation from perfect spherical shapes[210]. Following this, a more intricate inverse-designed structure intended for a free-form NIR polarization beam splitter is produced through 3D printing using two-photon lithography. The SEM image of the device is depicted in Fig. 8(c)[211]. The device was printed layer by layer vertically on top of the fused silica substrate. Furthermore, two-photon lithography offers an exceptional opportunity for the direct printing of optical functional metasurfaces on a fiber tip, as compared to techniques such as EBL[212] and FIB[213]. Plidschun *et al.* employed two-photon lithography to create nanopatterns on the end faces of modified single-mode optical fibers for multi-focus holography [Fig. 8(d)][214]. Additionally, Hadibrata *et al.* achieved 3D printing of a metasurface consisting of a circular grating-like structure on an optical fiber tip for metalens applications [left SEM image of Fig. 8(f)][215]. Simultaneously, they employed a computational inverse-design method based on an objective-first algorithm to design this structure. They showcased the application of the fabricated metalens with a fiber tip using a homemade two-photon polymerization process, as depicted in the right image of Fig. 8(f), where the pattern "NU" is produced using the LDW setup. In Fig. 8(e), perfect absorber metasurfaces with a unique 3D helix-based dielectric architecture for the IR spectral range are presented using the LDW[216]. The fabricated samples showcase resonant absorption bands with peak absorbance exceeding 80% in the wavelength range of 6–11 μm. LDW is typically a slower process, involving the scanning of a focused laser beam point by point, especially in the context of 3D printing by two-photon lithography, making it unsuitable for wafer-scale fabrication. Nevertheless, despite these limitations, LDW continues to be a valuable technique in applications where high precision and resolution are paramount, such as in microelectronics, photonics, and biomedical devices.

3.2 Advanced nanolithography techniques

In recent years, in addition to the mentioned standard nanolithography techniques such as EBL, FIB, and laser-based lithography, innovative lithography methods have been well developed. These updated methods are based on the combination of EBL, FIB, and LDW, and they include grayscale lithography[217–220], multistep lithography[221–225], and the novel fabrication of scanning probe lithography (SPL) based on the atomic force microscope, which is also studied in dielectric metasurface

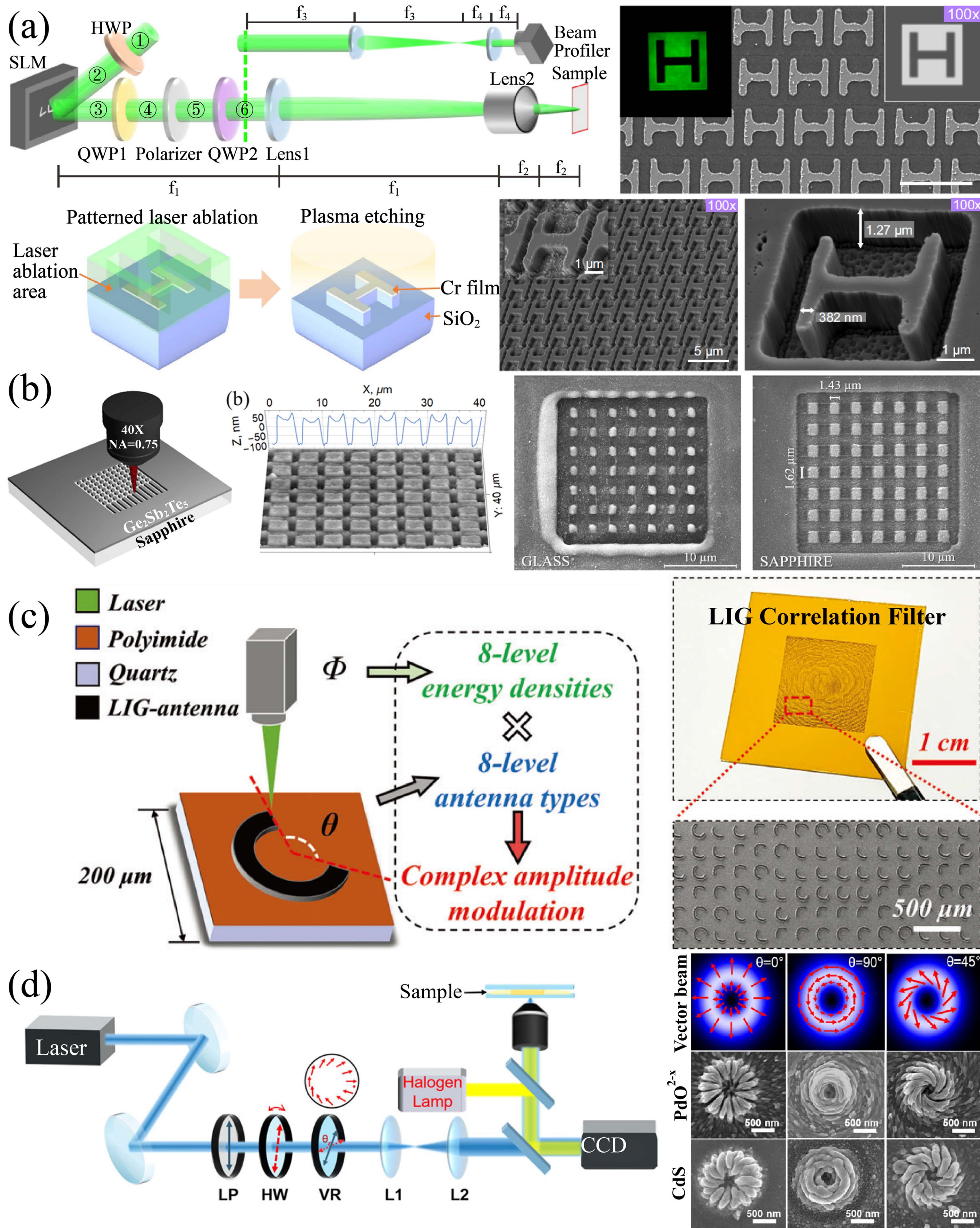

Fig. 7 The utilization of LDW in the fabrication of all-dielectric metasurfaces. (a) The patterned pulse LDW approach for creating sub-wavelength features. The schematic illustration (top) shows the pulse LDW system, and the SEM image of fabricated H-shaped arrays with sub-wavelength feature size is visible. Scale bars = 5 μm. Fabrication flow (bottom) of structures by etching after pulse LDW (Cr used as masks on fused silica substrate), along with SEM images of the H shapes.[205] (b) The fabrication process of $Ge_2Sb_2Te_5$ metasurfaces by LDW. The schematic on the left illustrates the laser casting process of a GST film through LDW. The AFM image in the middle showcases the fabricated metasurface with a square array, while the SEM images on the right depict the metasurface on glass and sapphire substrates, respectively.[206] (c) THz

optical pattern recognition enabled by a complex amplitude modulating metasurface through LDW: Schematic (left) of the fabrication of laser-induced graphene C-shaped antennas by LDW with different orientations and angles. Optical and SEM image (right) of the fabricated metasurface.[207] (d) Polarization-directed growth of spiral nanostructures by LDW with vector beams: Illustration of optical setup (left). Simulated beam profile with different vectors and SEM images of the chiral patterns formed with different vector beams (right).[208]

fabrication[226,227]. These approaches provide avenues for designing and fabricating more intricate nanostructures.

3.2.1 Grayscale lithography

Grayscale lithography stands out among advanced lithography methods, offering a novel approach to designing and fabricating intricate nanostructures. In contrast to nanolithography techniques like EBL, FIB, and laser lithography, which primarily focus on the fabrication of nanostructures with the same height, grayscale lithography introduces an additional level of control by enabling variable light intensity during the exposure process. This innovation addresses the limitation of these nanofabrication methods that often neglect the ability to vary the height of nanostructures on a single metasurface. In grayscale lithography, the intensity of light can be finely tuned, providing a continuum of exposure levels rather than a binary on-off state that achieves arbitrary structure control in the Z direction and X–Y direction simultaneously. This fine control empowers the creation of nanostructures with varying heights or depths, significantly enhancing the spatial regulation of nanostructures. This capability opens the door to the development of more sophisticated photonic devices with tunable height, including applications in color printing, multi/hyperspectral imaging, and metalenses[228–232]. EBL stands out as a compelling choice for grayscale nanopatterning. Geng *et al.* innovated a grayscale nanofabrication method using EBL and ALD, as illustrated in the schematic in Fig. 9(a)[233]. The process involves employing EBL to inscribe designed nanopatterns with varying irradiation doses, resulting in resist nanoholes with different depths that serve as a grayscale template. Subsequently, ALD is utilized to fill these nanoholes with TiO_2. Finally, TiO_2 nanostructures with diverse heights are constructed after removing the resist and the underlying TiO_2 film through etching. The SEM images depict a simultaneous structural change in three dimensions of the nanopillars along the X–Y–Z directions. Additionally, they proposed achieving structural color display through height modulation [as seen in the bottom image of Fig. 9(a)]. An alternative to EBL for grayscale nanolithography is FIB milling[234,235]. Hentschel *et al.* reported the fabrication of resonant Mie voids through FIB milling into silicon wafers. The top SEM image in Fig. 9(b) displays voids with varying diameters and depths. Furthermore, they explored applications in color printing using voids of constant diameter and varying depth, as depicted in the middle and bottom images of Fig. 9(b)[234].

Two-photon LDW presents a novel and alternative approach for grayscale nanolithography. Wang *et al.* explored color generation from nanopillars with varying heights, periodicities, and diameters in dielectric material using two-photon grayscale lithography [as depicted in the left image of Fig. 9(c)][236]. The SEM images of fabricated nanopillars with different heights are shown in the right image of Fig. 9(c). This method allows for the creation of arbitrary colorful and grayscale images by precisely controlling the parameters. In addition to these techniques, UV lithography can also be employed in grayscale lithography. As illustrated in Fig. 9(d), to showcase multispectral filter arrays in a single lithographic step across the visible to NIR spectrum, researchers combined grayscale lithography with metal–insulator–metal Fabry–Perot cavities, where the exposure dose controls cavity thickness. Initially, low-volume EBL grayscale lithography was employed, followed by the demonstration of large-volume UV mask-based photolithography using the binary mask approach[237].

3.2.2 Multistep lithography

Multistep lithography involves a sequence of lithographic processes aimed at creating intricate nanostructures. This strategy incorporates multiple patterning steps, each contributing to the final design. Multistep lithography is chosen when a single lithographic step proves insufficient for achieving the desired complexity. In Fig. 10(a), Lu *et al.* demonstrated the two-step lithography fabrication of a versatile silicon-based metasurface with superwettability for self-cleaning and dynamic color response[238]. This involved utilizing a Cr mask for the optical metasurface through EBL, followed by fabricating the resist mask for wettability-supporting structures using laser beam lithography. The process continued with plasma etching and mask removal, concluding with a treatment to achieve the desired wettability state. In another instance, researchers employed a combination of EBL and photolithography to fabricate a synthetic aperture metalens, as outlined in Fig. 10(b)[221]. This fabrication process included patterning a-Si nanopillar-based metalens and an aluminum (Al) mask to block unwanted light transmission outside the metalens aperture. The patterning steps were carried out through EBL and photolithography, respectively. Hybrid patterning techniques, combining various lithography methods, have been developed to realize metasurfaces with more complex nanostructures. Additionally, these techniques enable the creation of hybrid metasurfaces comprising both metal and dielectric materials with different geometries. In the left image of Fig. 10(c), Guo *et al.* investigated multipolar coupling in metal–dielectric metasurfaces, involving arrays of gold nanorods coupled to silicon nanodisks[222]. The fabrication process involved a two-step EBL process combined with a precision alignment step. The first step defined the silicon nanodisks through EBL and etching on an SOI wafer. In the second step, cross-shaped gold alignment marks were lithographically defined at the corners of the nanodisk arrays for fabricating plasmonic gold nanorods through EBL and lift-off. The resulting nanoantennas are depicted in the SEM image on the right side of Fig. 10(c).

3.2.3 Scanning probe lithography

SPL is another direct-write nanolithography technique that has emerged as an area of research in the field of atomic force microscopy. SPL employs a probe or tip in close proximity to a sample to directly pattern nanometer-scale features on the sample surface. This method offers high precision and flexibility in the creation of nanostructures. The interaction between

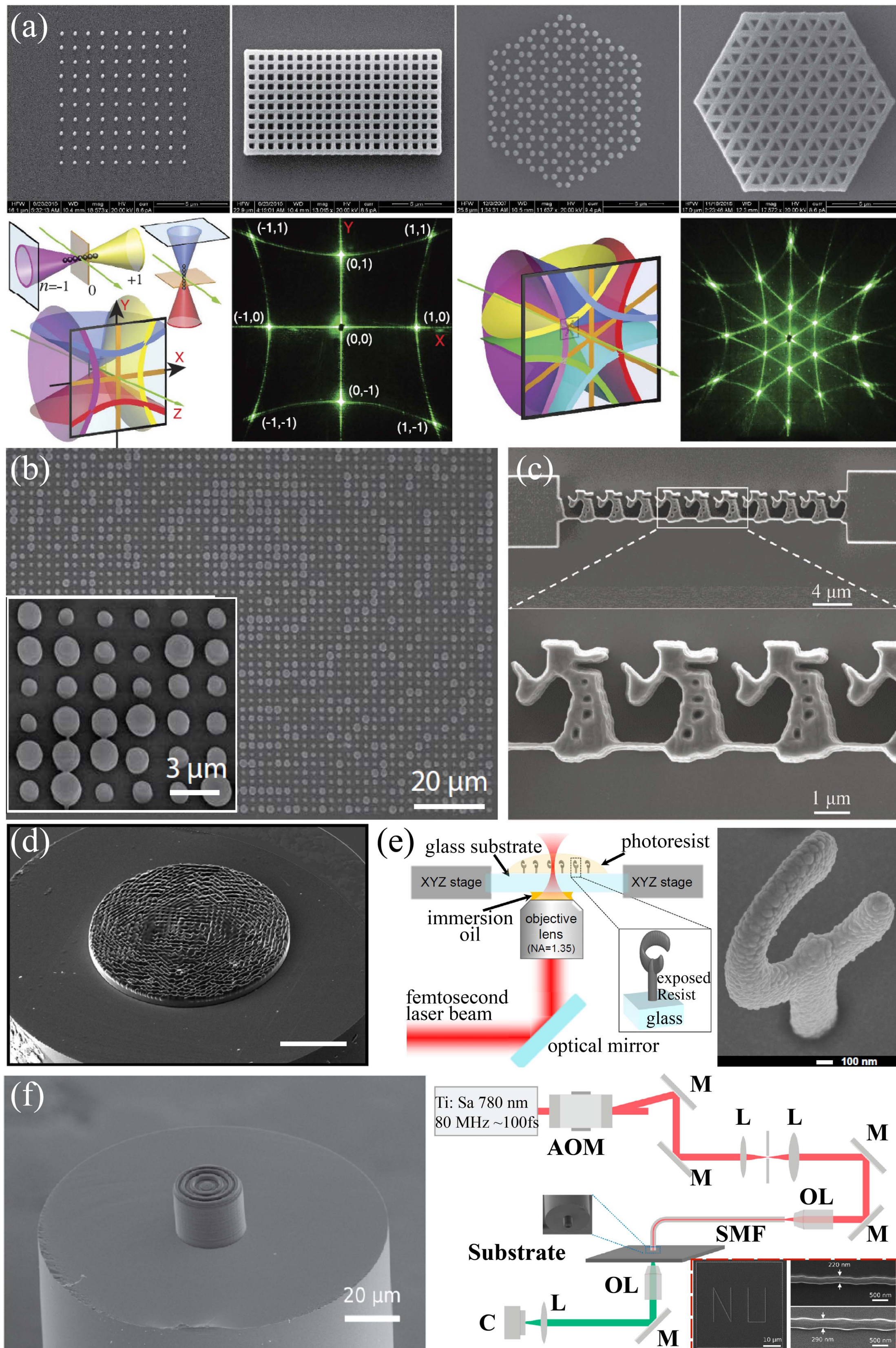

Fig. 8 The utilization of two-photon lithography in the fabrication of all-dielectric metasurfaces. (a) Dielectric metasurfaces in the optical diffraction with a fine structure: SEM images of fabricated dielectric particle/inverted counterpart structures and corresponding optical diffraction patterns.[209] (b) SEM images of the device for controlling 3D optical fields via inverse Mie scattering.[210] (c) SEM

images of an inverse-designed near-infrared polarization beam splitter fabricated by two-photon LDW.[211] (d) SEM image of a two-photon LDW-printed hologram on the single-mode fiber facet (scale bar is 20 μm).[214] (e) Realization of a helix-based perfect absorber for IR spectral range using two-photon LDW: Fabrication process (left) of dielectric templates. Zoom-in SEM image (right) of a single-turn metallic helix.[216] (f) Inverse design and 3D printing of a metalens on an optical fiber tip for two-photon LDW: SEM image (left) of the fabricated metalens on top of the fiber. Schematic of the homebuilt two-photon polymerization setup (right). The inset shows the SEM image of the pattern "NU" produced by the metalens using the homemade setup.[215]

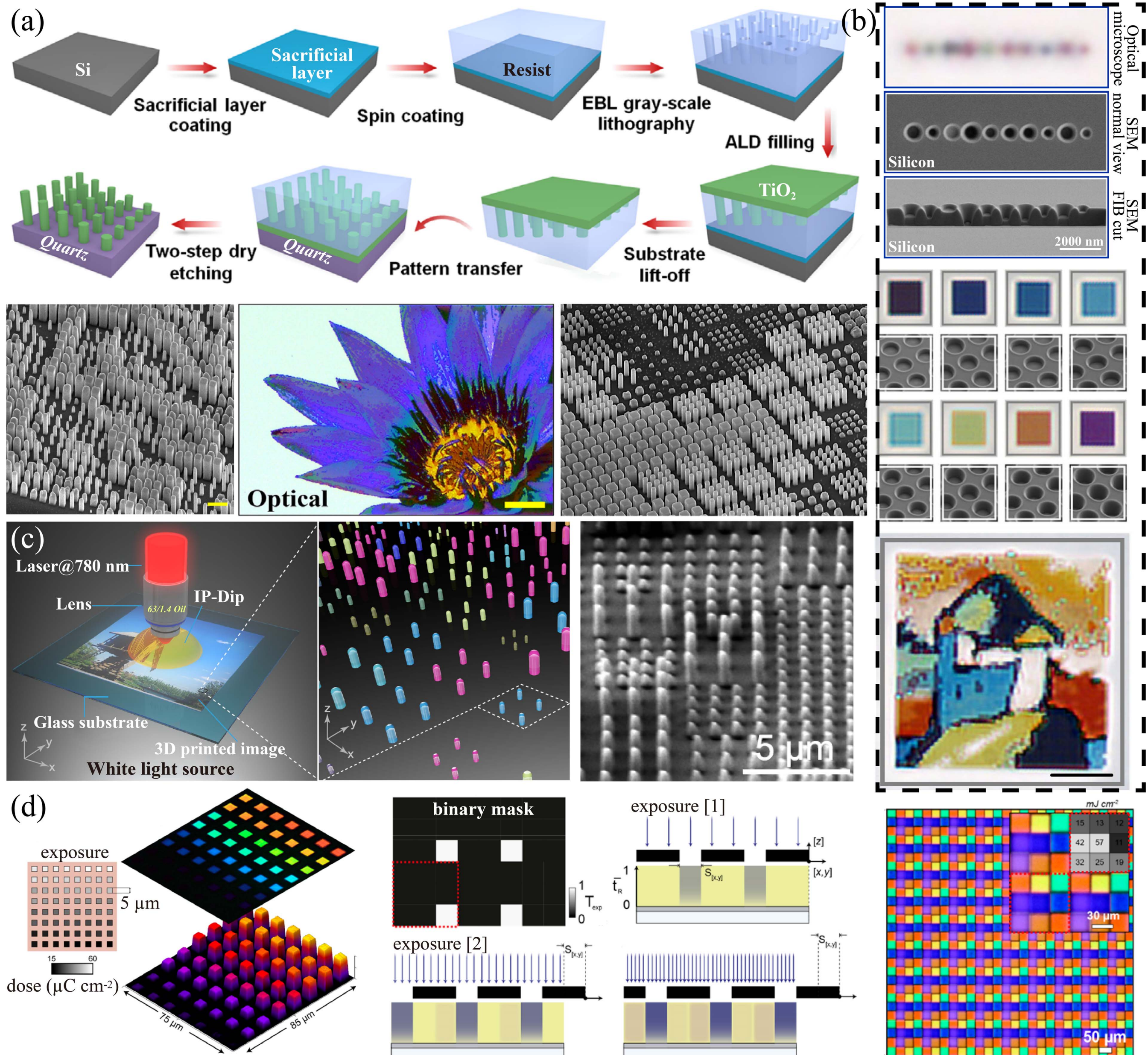

Fig. 9 The utilization of grayscale lithography in the fabrication of all-dielectric metasurfaces. (a) Grayscale lithography enables the creation of height-gradient-tunable nanostructure arrays, as illustrated in the schematic (top). This method utilizes grayscale EBL, ALD, and a transfer process for assembling nano-configurations with varying heights. The bottom row displays typical SEM images of TiO_2 nanopillars with height variations, showcasing the structural color metasurface after implementing height regulation.[233] (b) FIB grayscale lithography facilitates color printing using Mie voids in a silicon substrate. The top part illustrates conically shaped voids with varying diameters and depths in a bulk silicon wafer. In the middle, optical microscope and SEM images

showcase selected sizes and depths of Mie voids. The bottom section presents an optical microscope image of the color-printed image.[234] (c) Two-photon grayscale LDW is employed for 3D-printed low-index nanopillars, as outlined in the schematic of the fabrication process (left). The right side features a tilted view SEM of the 3D printed colorful painting, revealing pillars with varying heights, diameters, and periodicities.[236] (d) Custom multispectral filter arrays are fabricated using EBL and laser grayscale lithography. The left section demonstrates a dose-modulated pixel array by EBL, displaying the dose-modulated pattern, optical micrograph, and corresponding AFM data. The middle part outlines the fabrication flow of photolithography-based multispectral filter arrays using a binary photomask. The right side presents an optical micrograph (transmission) of a different region of the wafer, with a labeled equivalent exposure pattern (inset).[237]

the probe and surface is pivotal in the patterning process, and SPL can be categorized into various modes based on this interaction, including thermal, electrical, mechanical, and diffusive processes during the patterning operation. Figure 11(a) illustrates the SPL operation, depicting the intricate interactions involved in the process[239].

In thermal SPL, localized material modifications, such as crystallization, evaporation, and melting, are induced using thermal energy from a heated tip[242]. Lisunova *et al.* showcased high-aspect-ratio nanopatterning in silicon through combined thermal SPL and dry etching, as illustrated in Fig. 11(b)[240]. This method relies on the self-amplified depolymerization of a poly(phthalaldehyde) (PPA) thin film in contact with a heated probe. The SPL tool was utilized to inscribe patterns in the PPA thin film, which were then transferred into the SiO_2 hard mask through etching. In the final etching step, the SiO_2 pattern was further transferred into Si using deep RIE. The SEM images portraying the transferred patterns and the silicon sidewall are presented in the inset of Fig. 11(b), showcasing remarkable accuracy and uniformity, with a sidewall angle profile measuring approximately $87° \pm 2°$. SPL, grounded in a tip-induced electric field, emerges as a promising avenue for prototyping. Researchers have demonstrated a precise etching strategy for VO_2 by directly writing on a VO_2 film with a negative tip bias, followed by sonication removal of the written area. As depicted in the left image of Fig. 11(c), the results indicate that VO_2 can be etched layer by layer through alternately repeating tip modulation and sonication, allowing for the creation of arbitrary patterns[241]. Leveraging this approach, a metasurface was designed by arranging VO_2–gold nanoblocks with varying sizes and heights, enabling spectrally selective tunable reflectivity in the near- and mid-IR, as shown in the right image of Fig. 11(c).

These innovative lithography techniques, encompassing grayscale lithography, multistep lithography, and probe scanning lithography, broaden the horizons of nanostructure design and fabrication. Researchers and engineers can select the most fitting method according to the particular demands of their applications, providing enhanced flexibility in crafting intricate nanostructures. Nonetheless, it is essential to note that all of these methods are characterized by low throughput and high costs. Substantial enhancements are imperative to enable large-area patterning for widespread application in large-scale manufacturing processes.

3.3 Large-scale nanolithography techniques

Despite the rapid advancements in nanofabrication technology, most of these techniques remain in the laboratory stage and are far from practical application and commercialization. This is primarily due to extended processing times and the absence of mass production capabilities, which are crucial for semiconductor devices and integrated circuits. Industrial applications demand large-scale serial production of 2D microstructures, repeated tens of thousands of times, with silicon wafer surface areas ranging from 2 up to tens of inches. It is evidently imperative to develop large-area fabrication techniques with enhanced flexibility, high precision, and uniformity[94,243,244]. Several techniques have been proposed and studied to boost high-throughput productivity for larger-scale metasurface fabrication, incorporating methods such as UV lithography[245–251], nanoimprinting lithography[97,245,252–258], and self-assembly-based nanofabrication[259–265]. These approaches collectively contribute to the continuously evolving landscape of nanotechnology, paving the way for the cost-effective commercialization of metasurfaces.

3.3.1 UV lithography

Wafer-scale UV lithography employs UV light sources with specific wavelengths to pattern semiconductor wafers during the fabrication of integrated circuits. In semiconductor lithography, two types of photolithography tools are utilized in transferring patterns onto silicon wafers during the manufacturing process: the "stepper system" and the "scanner system"[266]. The stepper employs a step-and-repeat process, where the reticle (mask) and wafer remain stationary for each exposure, exposing one small part of the wafer at a time. The pattern is replicated across the wafer by repeatedly exposing and incrementally stepping the wafer position. On the other hand, the scanner utilizes a scanning system where the reticle and wafer move synchronously during the exposure process, exposing the entire wafer simultaneously.

Light is systematically scanned across the reticle, and the resulting exposed pattern is projected onto the entire wafer. Utilizing these systems, three UV lithography techniques are currently employed in metasurface fabrication: i-line ($\lambda = 365$ nm) stepper lithography, argon fluoride (ArF) DUV ($\lambda = 193$ nm) immersion scanner lithography, and krypton fluoride (KrF) stepper DUV ($\lambda = 248$ nm) lithography. The inherent planarity of metasurfaces aligns with fabrication processes directly compatible with the mature integrated circuit industry, providing opportunities for mass production. Employing i-line stepper lithography, as depicted in Fig. 12(a), researchers successfully fabricated a single 2-cm-diameter [refer to photograph in Fig. 12(a)] silicon-based NIR metalens, showcasing high-quality imaging and diffraction-limited focusing[267]. However, the large wavelength of i-line stepper lithography prevents the creation of nanostructures with smaller feature sizes suitable for working at visible wavelengths. Current state-of-the-art photolithography tools employ DUV light with wavelengths of 248 nm (KrF) and 193 nm (ArF). KrF DUV lithography

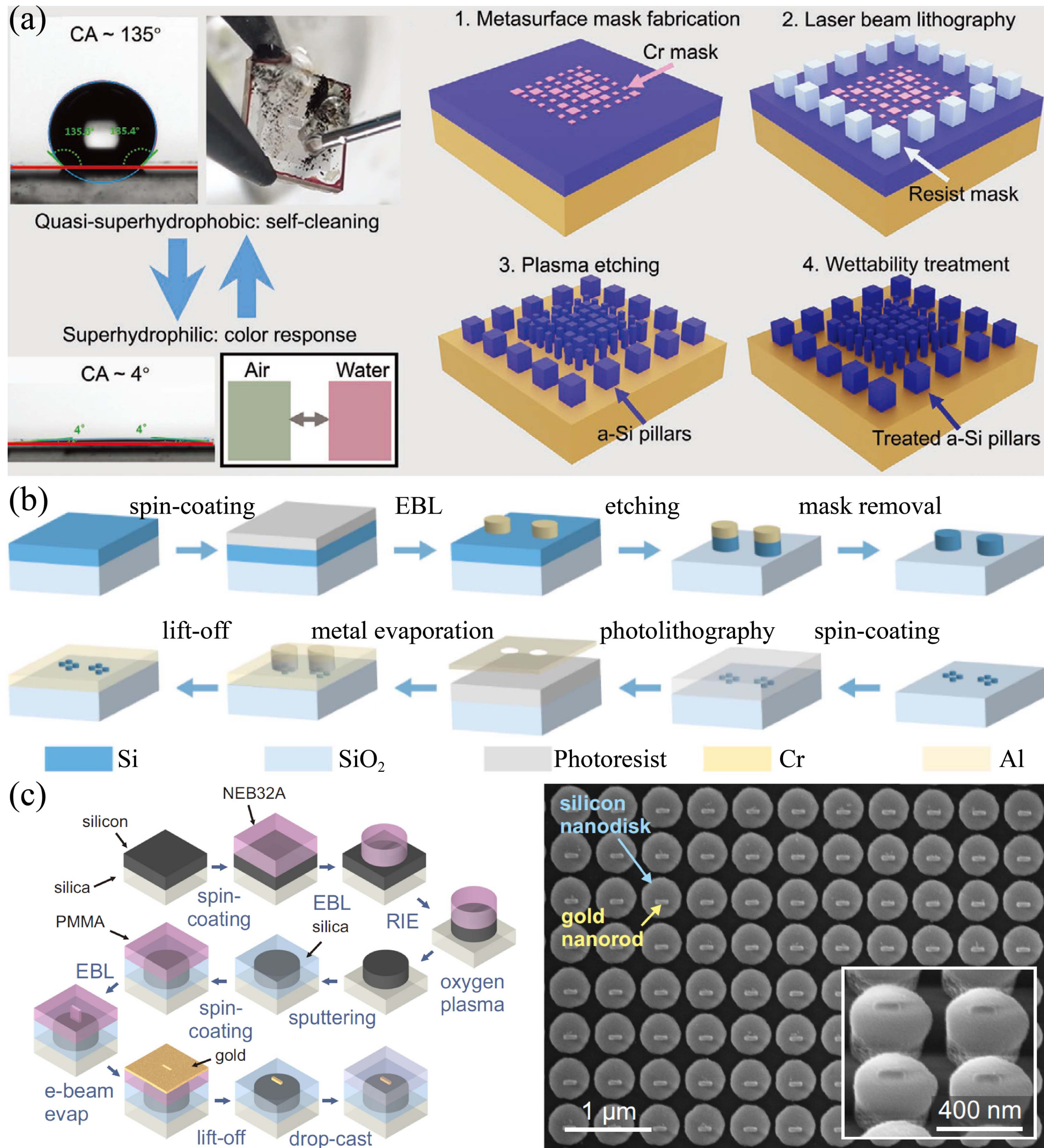

Fig. 10 The utilization of multistep lithography in the fabrication of all-dielectric metasurfaces. (a) A versatile metasurface with self-cleaning and dynamic color response, fabricated through EBL and laser lithography: Two super wettability states switchable with hydrophobic treatment or O_2 hydrophilic treatment (left).[238] Illustration of the multistep fabrication process for the sample (right). (b) Schematic of the fabrication process for the synthetic aperture metalens using EBL and photolithography.[221] (c) Hybrid metal–dielectric metasurfaces: Stepwise fabrication process of stacked hybrid nanoantenna metasurfaces (left). SEM images of the fabricated metasurfaces (right).[222]

has found applications in semiconductor manufacturing, striking a balance between resolution and cost-effectiveness for specific uses. As illustrated in Fig. 12(c), Park *et al.* presented centimeter-scale nanopillar-based metalenses made of glass fabricated using KrF DUV lithography, demonstrating the capability of focusing and imaging at visible wavelengths[268]. Furthermore, Leitis *et al.* employed KrF DUV lithography to introduce a versatile method for wafer-scale and cost-effective

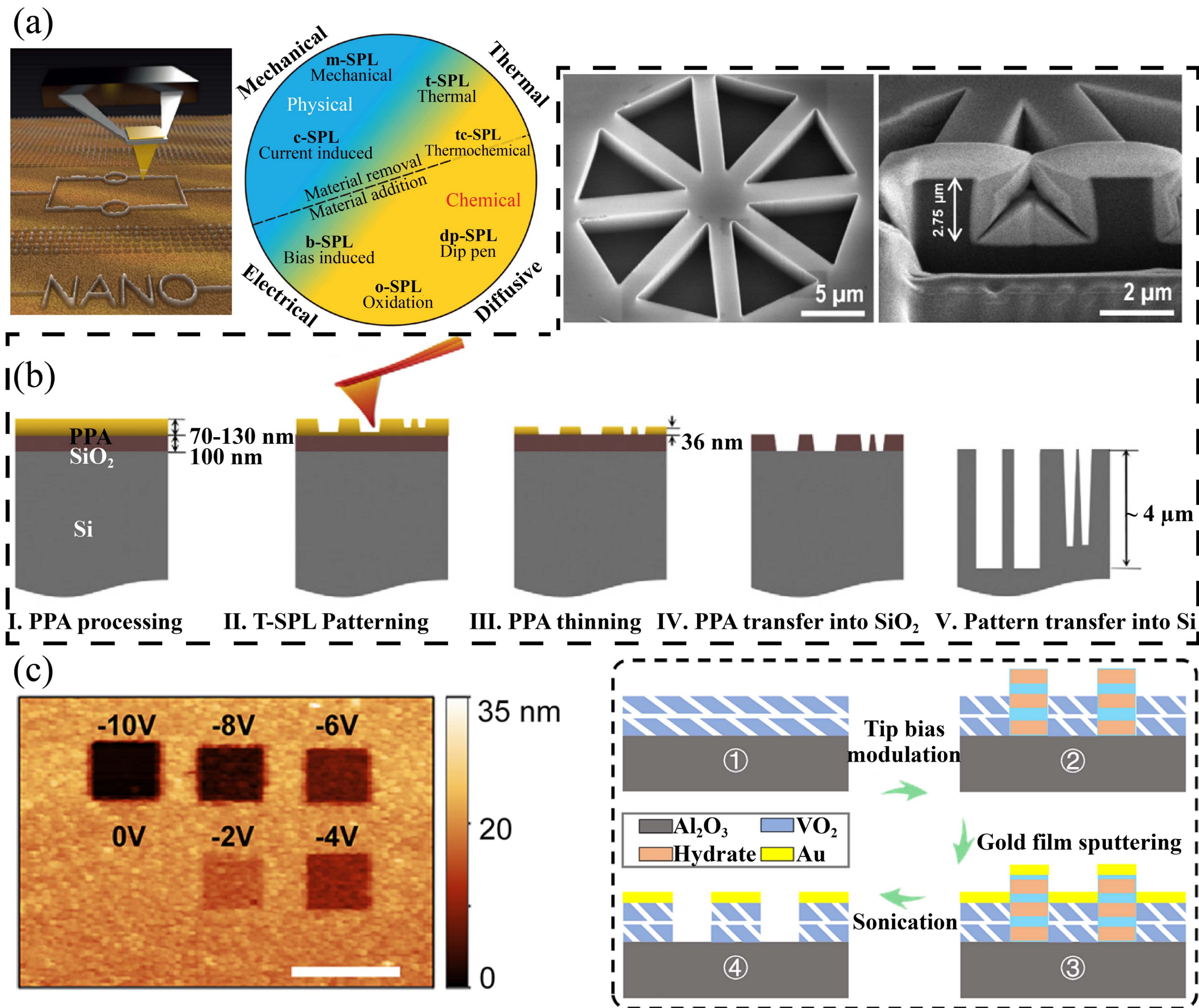

Fig. 11 The utilization of scanning probe lithography in the fabrication of all-dielectric metasurfaces. (a) SPL for imaging and patterning applications.[239] (b) Nanopatterning achieved through combined thermal SPL and dry etching, along with corresponding SEM images of silicon fabrication using a SiO_2 hard mask.[240] (c) Fabrication of a tunable metasurface based on VO_2 using electric-field SPL with precise depth control: Topography image of square patterns modulated by different tip bias voltages and followed by sonication. The scale bar is 2 μm (left). Schematic representation of the main steps in fabricating the designed metasurface (right).[241]

fabrication of Ge metasurfaces. This approach facilitates mid-IR photonics and biosensing in a high-throughput manner on silicon wafers, supporting optically transparent free-standing Al_2O_3 membranes [indicated by the blue color label in the SEM image of Fig. 12(b)][269]. ArF DUV lithography stands as a more sophisticated technology compared to i-line and KrF lithography, proving instrumental in the manufacturing of dielectric metasurfaces with reduced feature sizes. Xu *et al.* showcased the mass production of a Si nanopyramid-based metasurface polarizing bandpass filter on a 12 in. wafer. This achievement was realized through the utilization of 193 nm ArF DUV immersion lithography and direct inductively coupled plasma etching, strategically employed to manipulate polarization in the shortwave IR wavelength range[270]. Moreover, metasurface-based subtractive color filters have been manufactured on 12 in. glass wafer substrates utilizing 193 nm ArF DUV lithography. Through variations in pillar height and pitch, metasurfaces displaying different colors are attained, as illustrated in Fig. 12(e). It is noteworthy that the patterned a-Si layer is transferred from the Si wafer to a glass wafer via a bonding glue-assisted layer transfer process, as depicted in the bottom right of Fig. 12(e)[100,271]. They also showcased an a-Si metalens designed for fingerprint imaging operating at 940 nm. This metalens was fabricated on a 12 in. glass wafer using the 193 nm ArF DUV lithography. The enlarged optical image of the central die on the wafer is depicted in Fig. 12(f), highlighting the metalens, which is labeled by a red circle[272]. Most recently, Park *et al.* showcased an all-glass metalens with a diameter of 100 mm designed for operation in the visible spectrum, employing KrF DUV projection lithography as illustrated in the top panel of Fig. 12(g)[136]. A photograph and a tilted SEM image of the 100-mm-diameter metalens are presented in the bottom left

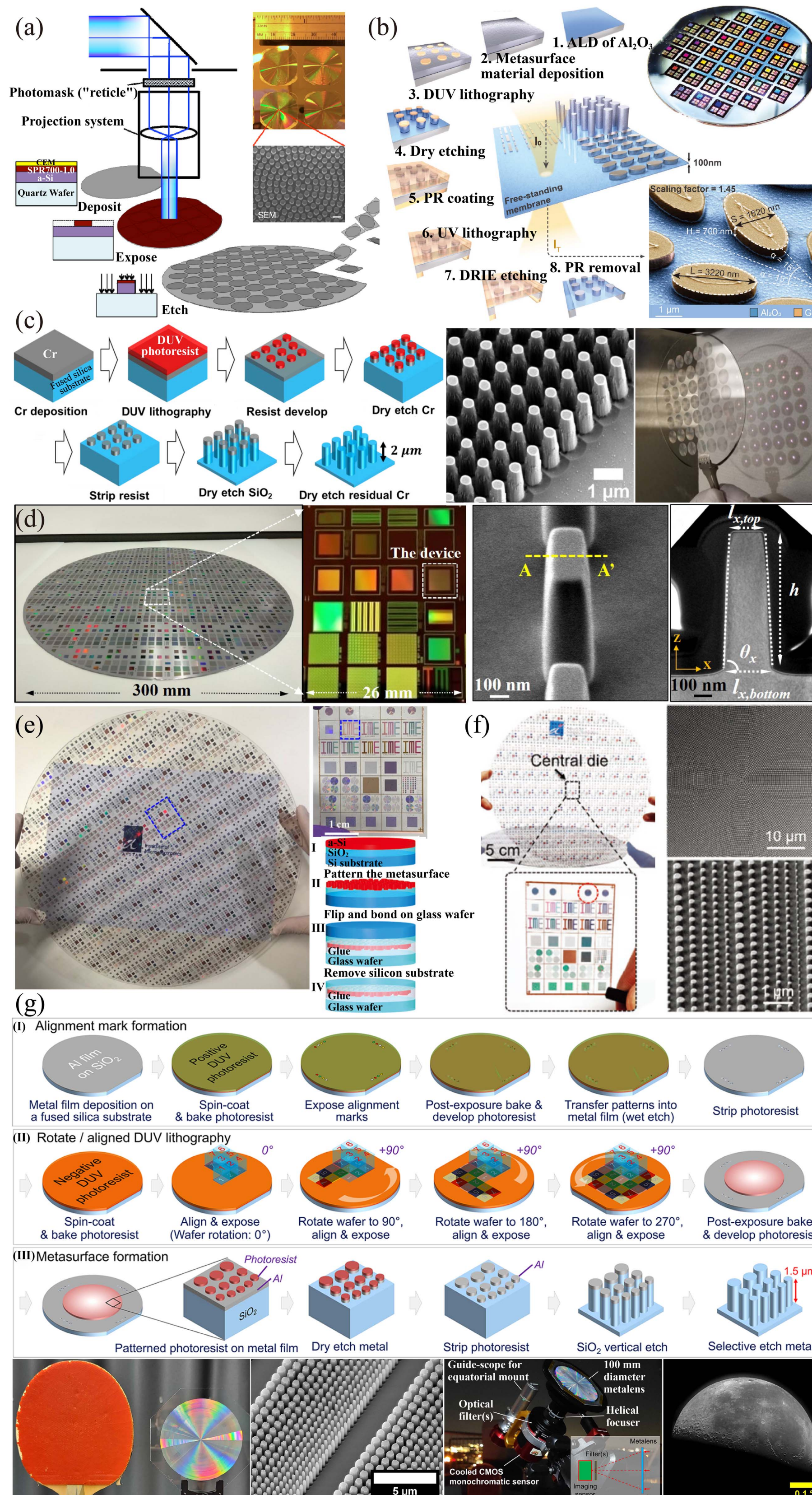

Fig. 12 The utilization of UV lithography in the fabrication of all-dielectric metasurfaces. (a) The schematic diagram illustrates the production of large-area metalenses utilizing photolithographic stepper technology. An accompanying photograph of the fabricated metalens (upper right) showcases a 2 cm diameter. A SEM image of the metalens center (center right) reveals the

nanocylinder constituting the metalens. Scale bar: 2 μm.[267] (b) The fabrication process of wafer-scale membrane-based metasurfaces for mid-infrared photonics and biosensing. In the top right photograph, a fully processed 4 in. silicon wafer is depicted, showcasing large-area metasurfaces. The bottom right provides a high-magnification SEM image of the metasurface unit cell, revealing the thin Al_2O_3 membrane in blue and the Ge resonators in orange.[269] (c) The left image illustrates the fabrication process of an all-glass, large metalens at visible wavelengths utilizing DUV projection lithography. On the right, zoomed-in SEM images showcase the nanopillars of the metalens, while a photograph displays the fabricated 1 cm metalenses on a 4 in. SiO_2 wafer.[268] (d) Photograph of the 12 in. silicon metasurface wafer, meticulously fabricated through the Multiple-Projects Wafer (MPW) line at Microelectronics IME for the production of polarizing band-pass filters. A detailed examination of the wafer center is presented in the zoomed-in view (left). Additionally, a tilted SEM image and a cross-sectional TEM image showcase a single silicon pyramid with intricate details (right).[270] (e) Image of a metasurface-based subtractive color filter crafted on a 12 in. glass wafer through a CMOS platform. In the top-right section, there are photo images of the central die subsequent to wafer dicing. The bottom-right segment illustrates the schematic of the fabrication process for layer transfer onto the glass wafer.[100, 271] (f) The left column depicts CMOS-compatible a-Si metalenses on a 12 in. glass wafer designed for fingerprint imaging, with the central circled region on the wafer highlighting the metalens. The right column showcases SEM images captured at both the central and outer zones of the metalens.[272] (g) The fabrication process of an all-glass 100-mm-diameter visible metalens for imaging the cosmos is depicted in the top panel. The bottom-left section features a photograph of the metalens, providing a size comparison with a table tennis racket, along with a SEM image showcasing the fused silica nanopillars constituting the metalens. In the bottom-right section, a photograph of the astro-imager is presented, consisting solely of a 100-mm-diameter metalens, an exchangeable optical filter, and a cooled CMOS monochromatic sensor. Additionally, an acquired image of the Moon is displayed.[136]

of Fig. 12(g), respectively. Furthermore, they successfully demonstrated direct astronomical imaging of the Moon at visible wavelengths, as depicted in the bottom right of Fig. 12(g).

Each of these lithography techniques signifies a milestone in the evolution of semiconductor manufacturing, with continuous endeavors to extend the boundaries of resolution and enhance the overall efficiency of the metasurface fabrication process.

3.3.2 Nanoimprint lithography

Nanoimprint lithography (NIL) has emerged as a pivotal tool in nanofabrication, providing a cost-effective, high-throughput, and large-scale production alternative to traditional photolithography techniques. In contrast to optical lithography, NIL is a nanofabrication technique that involves replicating patterns from a mold onto a resist-coated substrate, typically using a polymer material through physical deformation or curing. There are two main types of NIL based on the curing mechanism: thermal nanoimprint lithography (T-NIL) and ultraviolet nanoimprint lithography (UV-NIL)[273–276]. Thermal NIL relies on heating and cooling, wherein the resist material is softened or made molten by heating it to a temperature above its glass transition temperature. The mold is then pressed into the softened resist material, creating a replica of the mold pattern when its temperature is brought below the glass transition temperature. UV-NIL eliminates the need for heating and cooling processes using UV light to cure a UV-sensitive resist material. In comparison to T-NIL, UV-NIL is widely employed in metasurface fabrication due to its higher resolution and faster processing. Moreover, soft NIL, involving flexible molds made of polymeric materials like polydimethylsiloxane (PDMS), has been explored in the NIL process. This method, termed as soft NIL, enables the fabrication of metasurfaces on arbitrary surfaces[277,278]. The resist imprints the reverse structure from the original mold, not only serving as the hard mask but also directly functioning as the optical device. Yao *et al.* fabricated heterogeneous all-dielectric metasurfaces consisting of a-Si, Si_3N_4, and SiO_2, acting as an efficient ultra-broadband reflector through the NIL patterning process and etching. In the fabrication process illustrated in Fig. 13(a), the NIL-patterned resist is employed to create a Cr mask. Once the Cr mask is formed, RIE recipes are developed to etch the dielectric materials, resulting in a well-defined etching profile[279]. Moreover, the replication and transfer of nanostructured photoresist patterns onto the substrate can function as an etching mask for the final structure. As illustrated in Fig. 13(b), the primary stamp precisely transferred the master's pattern into the SU-8 photoresist. Subsequently, through optimized etching, well-controlled structures on the silicon can be obtained[280]. The conventional UV-NIL process typically employs the resist as the sole hard mask. However, to enhance the functional capabilities of the NIL resist, Yoon *et al.* pioneered the development of a TiO_2 nanoparticle-embedded UV-curable resin, illustrated in Fig. 13(c)[281]. Consequently, a dielectric metalens can be directly fabricated with a single step of UV-NIL, eliminating the need for secondary processes such as deposition or etching. In a subsequent investigation, Kim *et al.* introduced a metahologram crafted from a TiO_2 nanoparticle-embedded resist (PER), achieving a remarkable efficiency record of 90.6%. This metahologram was manufactured using a one-step NIL process, as depicted in Fig. 13(d)[126]. Furthermore, this one-step nanoimprinting facilitates transfer onto various substrates, ranging from flexible films to diverse hard surfaces like PC, PP, and curved glasses. To address issues such as warpage and breakage of nanostructures during mold detachment, Choi *et al.* innovatively replaced the detaching process with wet etching of a replica mold crafted from a water-soluble polymer, polyvinyl alcohol (PVA). The fabrication process for wet etching NIL is illustrated in Fig. 13(e)[282]. TiO_2 PER is applied to the PVA replica mold through spin coating. Following the curing of PER under

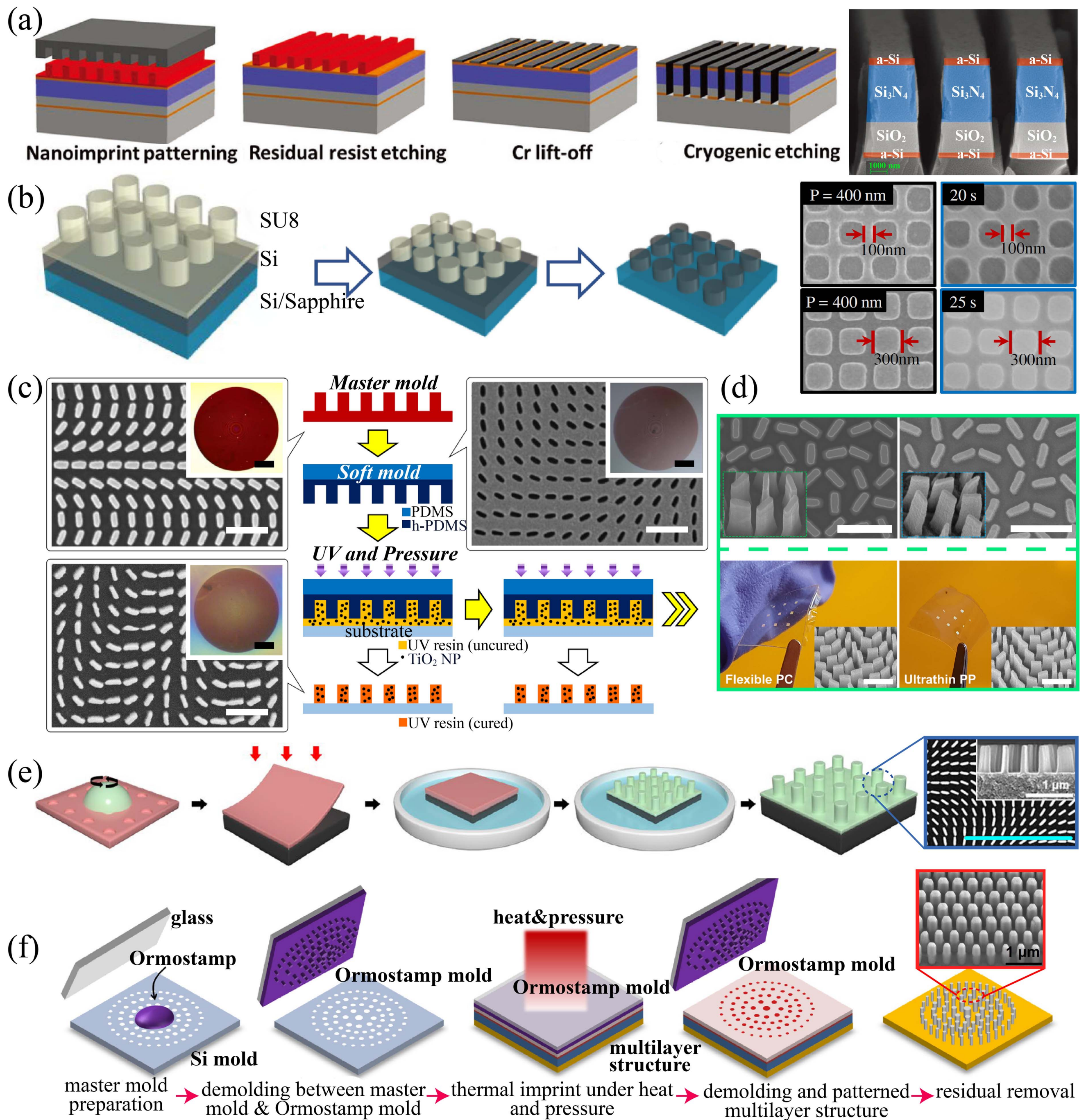

Fig. 13 The utilization of nanoimprint lithography in the fabrication of all-dielectric metasurfaces. (a) The fabrication process of an all-dielectric heterogeneous metasurface, designed as an efficient ultra-broadband reflector, is depicted on the left. The cross-sectional SEM image on the right provides a detailed view of the fabricated metasurface.[279] (b) Schematic representation of the fabrication process for silicon nanostructures with adjustable geometries through soft nanoimprint lithography and reactive ion etching (left). The initial imprinted SU8 nanostructure is presented in the first column before etching. The second column displays the results after well-controlled etching times, showcasing the tunable meta-atom geometries (right).[280] (c) Single-step manufacturing of hierarchical dielectric metalenses in the visible. SEM images depict the master mold, soft mold, and final plum pudding metalens, respectively. Scale bars: 1 μm. Scale bars of inset optical micrographs: 100 μm.[281] (d) The TiO_2 nano-PER metahologram is fabricated through a one-step process of nanoparticle-embedded-resin printing. The initial row showcases the SEM image of the master mold meticulously crafted using EBL on a silicon substrate. The subsequent image displays the intricate final structure of the printed TiO_2 nano-PER. In the second row, the successful

replication of the TiO_2 nano-PER metahologram is exhibited on diverse substrates, including flexible polycarbonate (PC) and ultrathin polypropylene (PP). Scale bars: 1 μm.[126] (e) Illustration depicting the achievement of high-aspect-ratio metalenses through nanoimprint lithography utilizing water-soluble stamps (left). SEM images showcasing the replicated metalens (right).[282] (f) Schematic illustration depicting the fabrication of a metalens through multilayer nanoimprint lithography and solution phase epitaxy. The inset images on the right showcase SEM images of the ZnO metalens.[283]

sufficient pressure and UV illumination, the substrate adheres to the PVA mold. As PVA is a water-soluble polymer, the PVA mold covering the substrate dissolves, leaving only the replicated TiO_2 nanostructures on the substrate. This method, unlike conventional NIL, avoids introducing shear stress in cured nanostructures, enabling the replication of various patterns without faults. Moreover, through the utilization of multilayer NIL and solution-phase epitaxy (SPE), high-aspect-ratio ZnO nanopillar-based metalenses are successfully demonstrated[283]. The main procedure, as illustrated in Fig. 13(f), involves initially replicating an OrmoStamp mold from the silicon mold. Subsequently, a nanoimprint resist is spin-coated on top of the multilayer structure, patterned by a thermal nanoimprint with the OrmoStamp mold, and followed by dry etching of the SiO_2 layer and the PMMA layer. The PMMA layer is fully etched to expose the ZnO seed layer. Finally, ZnO nanopillars are grown in a precursor solution, and the residual SiO_2 and resist layers are removed by dry etching, resulting in the acquisition of the ZnO metalens.

NIL offers the advantages of high resolution, large-area fabrication, and cost-effectiveness. The reusability of stamps further contributes to a substantial reduction in fabrication costs and environmental impact. However, it is important to note that this method still necessitates the fabrication of a mold using high-resolution equipment.

3.3.3 Self-assembly of nanostructures

Self-assembly (SA) is a process wherein smaller components spontaneously unite to create larger, well-defined, and stable aggregates[284]. Recently, it has emerged as a promising alternative to lithographic techniques for crafting features and structures at the nanometer scale. This approach provides a cost-effective and scalable method to achieve intricate structures, followed by subsequent etching or deposition processes. Self-assembled monolayers (SAMs) consist of single layers of molecules that autonomously organize into ordered lattices on the surface of a substrate. Various SAMs, formed using organic molecules, have found extensive application in the fabrication of dielectric metasurfaces. Zhang *et al.* presented a flexible, all-dielectric metasurface fabricated through nanosphere self-assembly, showcasing its potential applications in sensing[285]. The principal fabrication steps are illustrated in Fig. 14(a): initially, a thin layer of Si is deposited onto a polyethylene terephthalate (PET) substrate. Subsequently, a monolayer of polystyrene (PS) spheres self-assembles and is transferred onto the Si surface [top right SEM image in Fig. 14(a)]. Following this, plasma etching is employed to reduce the size of the PS spheres, serving as a mask for a second RIE procedure. This preserves the Si cylinder-based metasurface directly beneath the PS spheres. The SEM image of the Si cylinders is depicted in the bottom right of Fig. 14(a). Moreover, Valentine *et al.* elucidated the design and manufacturing of large-scale perfect reflectors using Si-based cylinder resonators on SOI substrate. The patterning was achieved through nanosphere lithography and RIE as illustrated in Fig. 14(b)[98]. The SEM images, coupled with the optical image, unequivocally showcase the capability of nanosphere lithography to produce high-quality dielectric resonators across a sizable area. In a subsequent investigation, a pioneering manufacturing technique was introduced, leveraging grayscale nanosphere lithography. This method enables the cost-effective and scalable fabrication of metasurfaces featuring arbitrary, nonperiodic phase profiles. To attain nonperiodic phase control, nanosphere lithography is integrated with illumination from an SLM, facilitating spatial control of the dose and exposure size, as illustrated in Fig. 14(c)[232]. To assess the efficacy of the technique, they produced large-scale metalenses operating at a wavelength of 1.7 μm. The fabricated metalenses showcased diffraction-limited focusing and achieved an impressive relative efficiency exceeding 83%. Moreover, Gupta *et al.* proposed a straightforward self-assembly fabrication method combined with nanoimprinting approaches, eliminating the need for nanospheres. They showcased the controlled dewetting of optical glass thin films to achieve all-dielectric metasurfaces over a large area. The self-assembly of various optical nanostructures with feature sizes down to ∼100 nm and interparticle distances as small as 10 nm is experimentally demonstrated. The fabrication approach is illustrated in Fig. 14(d)[286]. Soft lithography is initially employed to imprint a PDMS mask onto a thermoplastic or sol–gel layer through nanoimprinting [Fig. 14(d), top]. Subsequently, a thin layer of chalcogenide glass is deposited through evaporation. The annealing process induces dewetting of the glass layer, leading to its breakup into an array of well-dispersed and self-ordered nanoparticles, as depicted in the SEM images in Fig. 14(d). This approach is both simple and scalable, as underscored in the bottom of Fig. 14(d), where an EPFL logo has been created by embossing a $20 \times 11\ \mathrm{cm}^2$ polycarbonate sheet with nanostructured assembled PDMS molds. In addition to the aforementioned large-scale fabrication techniques, researchers have also demonstrated a novel method utilizing an anodized aluminum oxide (AAO) template combined with a TiO_2 metasurface[287]. Furthermore, they have explored the direct construction of larger-scale nanostructures on resist[288–290].

4 Extreme Fabrication and Application

Through the exploration and optimization of nanofabrication technology, various intricate nanostructures have been proposed through extreme fabrication techniques, encompassing multilayer fabrication[291–295], flexibility[296–298], slanted orientation[84,94,299,300], and high aspect ratios[301,302]. These innovative approaches introduce additional degrees of freedom for tailoring metasurface functionalities. The pursuit of extreme fabrication and the application of metasurfaces involve pushing the boundaries of conventional nanofabrication techniques to achieve structures with unprecedented properties and functionalities. The following provides a summary of recent advanced dielectric metasurface nanofabrication methods, covering multilayer to

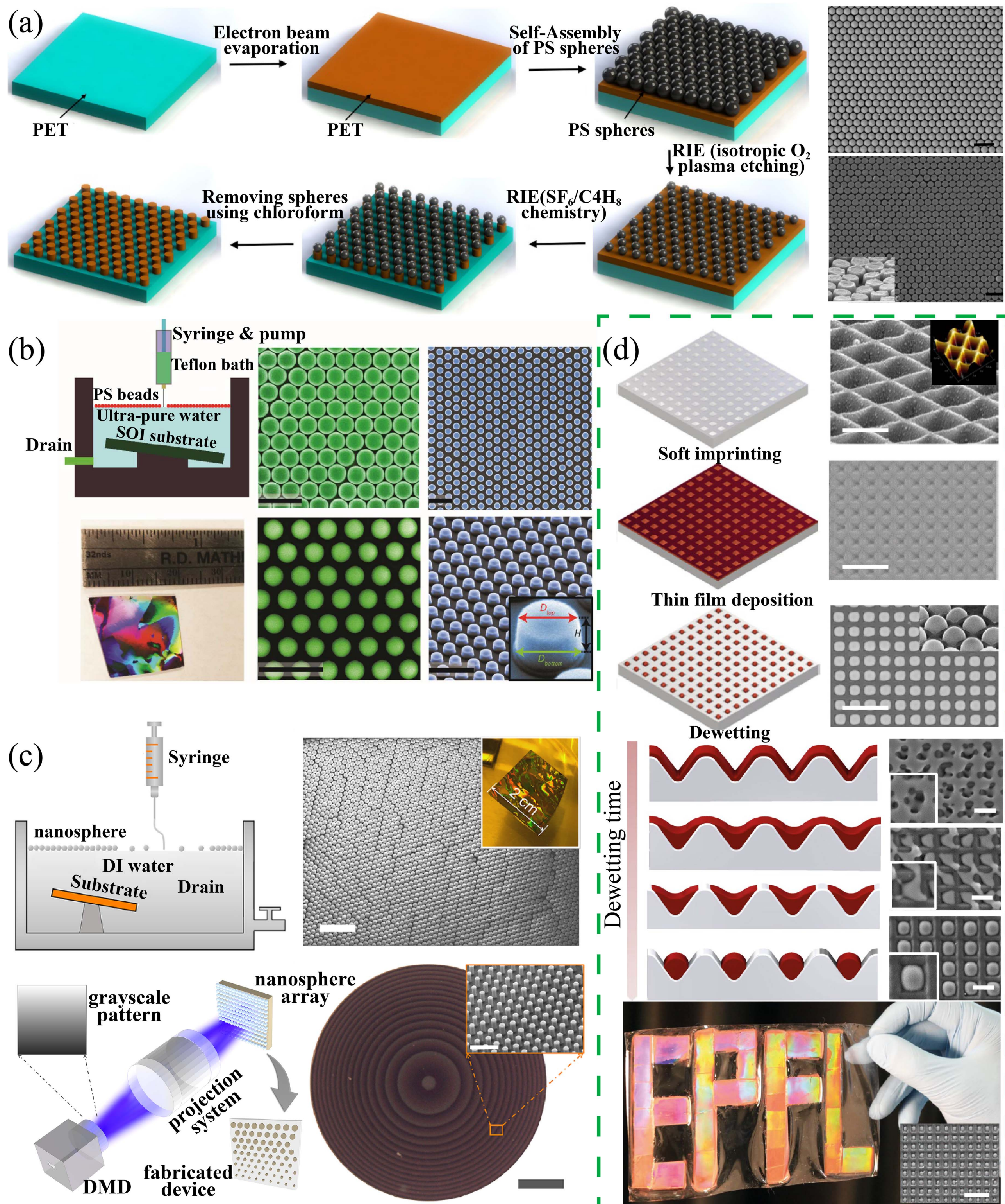

Fig. 14 The utilization of self-assembly in the fabrication of all-dielectric metasurfaces. (a) Illustration of the primary fabrication steps for the flexible, all-dielectric metasurface utilizing nanosphere lithography. The accompanying images on the right showcase SEM images of self-assembled polystyrene (PS) spheres (top) and Si cylinders (bottom) formed after RIE. Scale bars: 1 μm.[285] (b) Illustration of the self-assembly-based nanosphere lithography technique for the large-scale fabrication of all-dielectric metasurface perfect reflectors, accompanied by a camera image depicting the pattern of PS spheres on an SOI substrate (left column). SEM images showcase PS spheres with a diameter initially at 820 nm and subsequently downscaled to 560 nm

after etching (middle column). The top and tilted views exhibit the final metamaterial, comprising an array of Si cylinders. Scale bar: 2 μm.[98] (c) Image of large-scale metasurfaces created through grayscale nanosphere lithography. A grayscale pattern is produced by the DMD system utilizing a 365 nm I-line UV light source, transmitted through a projection system incorporating an objective lens. The schematic depicts the air–water interface for nanosphere self-assembly, while the SEM image showcases the close-packed nanosphere monolayer after self-assembly, with a scale bar of 5 μm. Additionally, an optical image of the fabricated metalens is presented. Scale bar: 200 μm.[232] (d) The left panel illustrates the schematic, while the right panel displays the SEM image of the self-assembly process of nanostructured glass metasurfaces through templated fluid instabilities. The fabrication initiates with thermal or ultraviolet nanoimprinting of the requisite pattern on a substrate, as shown in the top section (scale bar, 400 nm). Subsequently, a thin-film deposition of high-index optical glass is performed in the middle section (scale bar, 1 μm). The final step involves annealing to induce the dewetting process, depicted in the bottom section (scale bar, 1 μm). A schematic of the dewetting process is also provided. An optical photograph showcases a large area (20 cm × 11 cm) EPFL logo-shaped metasurface on a polymer substrate, with an inset SEM image revealing the corresponding nanostructure (scale bar, 1 μm).[286]

high-aspect-ratio fabrication. These extreme fabrication techniques enhance the capabilities of conventional methods, unlocking new possibilities for optical devices with superior performance and adaptability.

4.1 Multilayer dielectric metasurface nanofabrication

Multilayer dielectric metasurface nanofabrication involves creating dielectric metasurfaces with multiple layers of distinct structures or materials. Fabricating multilayer dielectric metasurfaces typically necessitates multiple lithographic and processing steps, which require precise alignment of the successive layers. Current advanced nanotechnology facilitates the use of lithography tools with a straightforward versatile alignment scheme and procedure. Alignment can be conducted either manually, targeting any visible feature on the surface of the wafer or chip, or automatically, utilizing well-defined and fabricated alignment marks. Moreover, the impact of misalignment on the optical response of the metasurface should be thoroughly considered. Any misalignment between the upper and lower layers within the achieved fabrication tolerances must be accounted to ensure optimal performance. Tanaka *et al.* conducted experimental demonstrations on bilayer chiral dielectric metasurfaces that exhibited multipolar resonances. Notably, they achieved a record-high circular dichroism of 0.7 at that time. The fabrication of bilayer silicon metasurfaces involved a two-step EBL procedure, as illustrated in Fig. 15(a)[303]. They used standard nanolithography to fabricate the first silicon metasurface on fused silica. Next, they embedded the silicon metasurface into a planar glass layer by depositing a SiO_2 layer and spin-coating a layer of polymer. To fabricate the second layer of the bilayer system, the previously described lithography process was repeated with precise alignment and etching steps. The top-view SEM and oblique-view SEM of the fabricated bilayer metasurfaces of different arrays are shown in the right SEM images in Fig. 15(a). Researchers have not only fabricated bilayer metasurfaces using identical dielectric materials but have also explored the creation of bilayers composed of different materials. Leveraging precise nanofabrication technology, Deng *et al.* introduced a bilayer metasurface designed to independently manipulate the phase of visible light in both reflection and transmission spaces. This innovative bilayer metasurface comprises two distinct anisotropic nanobricks, namely silicon and silver. The intricate fabrication process of these bilayer metasurfaces is detailed in Fig. 15(b)[103]. In the initial step, the first layer of the α-Si metasurface is crafted through the EBL and etching process. Subsequently, a negative photoresist film is subjected to exposure via a lithography machine. Following this, an Al_2O_3 film is deposited to safeguard the photoresist. Finally, the sample undergoes recoating with a PMMA resist, followed by exposure through an overlay EBL procedure. Upon the evaporation of Ag and subsequent lift-off, a bilayer metasurface emerges, comprising arrays of α-Si and Ag nanobricks. The SEM images of the meta-hologram sample are presented in Fig. 15(b) on the right. In addition to employing two-step lithography for fabricating multilayer metasurfaces, researchers have showcased independent phase modulation at multiple wavelengths by closely stacking dielectric metasurfaces embedded in PDMS. To experimentally validate this approach, a metalens doublet was fabricated through essential steps, as summarized in Fig. 15(c). The initial a-Si metalens was delineated utilizing EBL and RIE. Subsequently, a thin layer of PDMS was spin-coated to encapsulate the nano-posts, forming a slender spacer layer that enables the close stacking of the second layer. The second substrate underwent preparation involving the deposition of a Ge layer as the sacrificial layer, succeeded by a-Si growth on Ge. The silicon metalens was crafted through identical procedures, followed by embedding the lens in a substantial PDMS layer. Following the dissolution of the Ge layer for substrate release, the transferred layer was precisely aligned by the alignment marks and bonded to the initial layer. An SEM image of the silicon nano-posts is presented in Fig. 15(c) on the right. Essentially, the aforementioned methods can be extended to fabricate three or even more layers of metasurfaces by iteratively executing the steps of encapsulation and nanostructure fabrication. Furthermore, leveraging advanced 3D printer technology, multilayer nanostructures can be directly fabricated through multiphoton lithography, obviating the necessity for multistep lithography and etching processes. Balli *et al.* introduced a hybrid achromatic metalens using two-photon lithography. These hybrid achromatic metalenses integrate a phase plate and a metalens into a single thin element, as depicted in Fig. 15(d), demonstrating high focusing efficiency and chromatic aberration correction across a broad spectral range from 1000 to 1800 nm[304]. Moreover, employing a 3D printer, researchers introduced a novel design for multilayer achromatic metalens and multilayer meta-optics [depicted in Figs. 15(e) and 15(f)][305,306]. They utilized topology optimization and

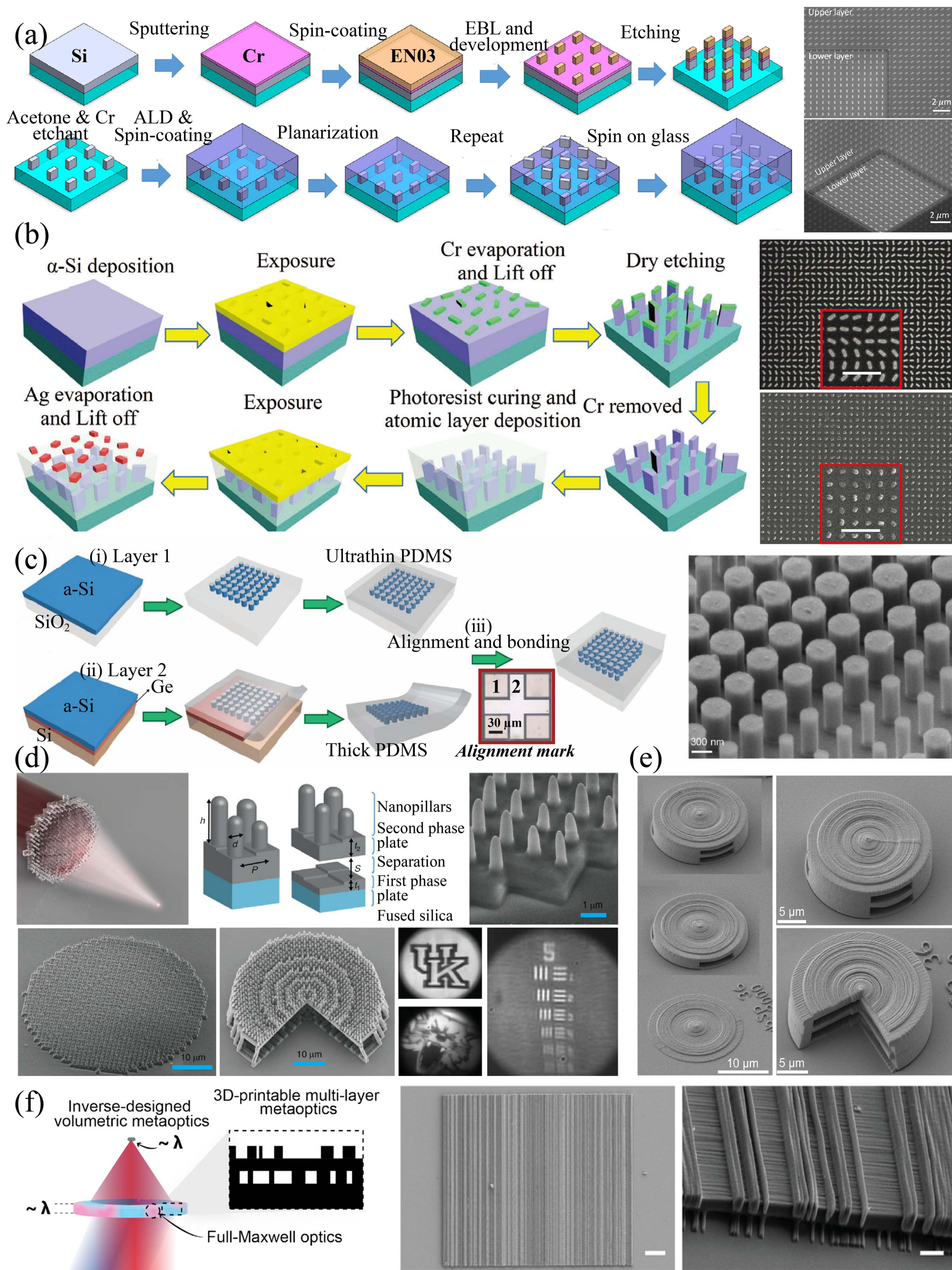

Fig. 15 Multilayer dielectric metasurface nanofabrication. (a) A depiction of the sequential steps involved in the fabrication of bilayer chiral silicon metasurfaces. The right image provides a perspective and an oblique-view SEM representation of the accomplished chiral metasurfaces.[303] (b) Bilayer metasurfaces for comprehensive light manipulation involve a meticulous fabrication process, as illustrated on the left. The SEM image on the right depicts the a-Si nanobrick array and the Ag nanobrick array, showcasing the intricate details. Scale bars: 1 μm.[103] (c) The fabrication process of multilayer non-interacting dielectric metasurfaces for multiwavelength

meta-optics is depicted on the left. The inset displays an optical microscope image of the alignment marks from the two layers. Scale bar: 30 μm. An SEM image of silicon nano-posts before PDMS spin coating is presented on the right. Scale bar: 300 nm.[307] (d) The hybrid achromatic metalens, composed of a phase plate and nanopillar, is designed for broadband, near-infrared imaging and fabricated using two-photon lithography.[304] (e) Multilayer achromatic metalenses (MAMs) with high numerical aperture produced through 3D printing. The left image presents a tilted view of the fabricated multilayer achromatic metalenses, showcasing deconstructed MAMs with single, double, and triple (full) layers. The right SEM image offers an enlarged view of the full MAM and sectioned MAM.[305] (f) Inverse-designed multilayered metaoptics using 3D printing, implemented in a low-index polymer. The SEM of the measured sample is displayed in the right panel.[306]

full-wave simulations for the inverse design of multilayer meta-optics, subsequently fabricating the structures in low-refractive-index materials through two-photon polymerization lithography.

4.2 Flexible dielectric metasurface nanofabrication

Flexible dielectric metasurface nanofabrication is dedicated to the creation of adaptable dielectric metasurfaces capable of conforming to curved or non-planar surfaces. The capacity to bend and stretch metasurface devices on flexible substrates introduces a new dimension to the manipulation of electromagnetic waves, offering the potential for innovative device designs and functionalities. Zhang *et al.* showcased a method for achieving a mechanically tunable all-dielectric metasurface with polarization insensitivity and a full-spectrum response in the visible range [Fig. 16(a)][308]. The structure of the TiO_2 metasurface is schematically depicted in the middle image of Fig. 16(a). It consists of an array of TiO_2 nanoblocks embedded in a PDMS substrate. The metasurfaces were fabricated using the EBL technique followed by lift-off and transfer processes, as shown in the left image of Fig. 16(a). An epoxy-based negative photoresist (SU-8) is spin-coated onto the copper foil substrate to decrease the surface roughness of the copper foil. Finally, a Cu/SU-8/Cu substrate serves as a sacrificial substrate for the fabrication and transfer of the TiO_2 metasurface. Furthermore, researchers demonstrated a highly tunable dielectric metasurface microlens based on silicon nano-posts encapsulated in thin PDMS, showcasing focal distance tuning from 600 μm to 1400 μm[309]. Figure 16(b) delineates the essential stages involved in the fabrication of a metasurface. Initially, a Ge sacrificial layer was evaporated onto a silicon wafer. The pattern was crafted using EBL and an etching process. Subsequently, PDMS was spin-coated onto the fabricated metasurface, and the embedded nano-posts within the PDMS were liberated by eliminating the Ge sacrificial layer. The SEM image of the nano-posts before the PDMS spin coating is displayed in the middle of Fig. 16(b), while the SEM image of the nano-posts embedded in PDMS is shown on the right. In a subsequent study, the researchers showcased a method for disentangling the optical properties of objects from their physical shape by employing thin and flexible dielectric metasurfaces [Fig. 16(c)]. These conformal metasurfaces consist of silicon nano-posts embedded in a PDMS substrate, fabricated through a process akin to the one depicted in Fig. 16(b)[102]. Conventional flexible substrates are susceptible to plasma damage and organic solvents. The utilization of EBL for fabricating dielectric metasurfaces typically entails plasma processes and organic solvents, rendering direct fabrication on a flexible substrate impractical. Researchers have showcased a straightforward nanoimprinting method for fabricating dielectric metasurfaces on a flexible substrate [Fig. 16(d), left][253], a process similar to the one depicted in Fig. 13(c). This approach circumvents the need for plasma processes and organic solvents and is also compatible with flexible substrates [Fig. 16(d) right]. In addition to nanoimprinting, the self-assembly technique can also be employed on flexible substrates, as demonstrated by the metasurface sample on a flexible PET substrate [Fig. 16(e)][285].

4.3 Slanted dielectric metasurface nanofabrication

Slanted dielectric metasurface nanofabrication involves the fabrication of dielectric metasurfaces with structures oriented at non-perpendicular angles to the substrate. Chen *et al.* introduced a novel paradigm of slant-perturbation metasurfaces and presented the experimental realization of genuine chiral response in resonant metasurfaces. The engineered slant geometry disrupts both in-plane and out-of-plane symmetries, leading to the first observation of intrinsic chiral BICs. This phenomenon exhibits near-unity circular dichroism of 0.93 and a high-quality factor exceeding 2663 for visible frequencies, as illustrated in the right column of Fig. 17(a)[84]. The metasurface comprises a square array of slanted trapezoid nanoholes in a TiO_2 film, positioned on a glass substrate and coated with PMMA [Fig. 17(a)]. This structure evolves from vertical square nanoholes through the introduction of two perturbations: an in-plane deformation angle α and an out-of-plane slant angle φ, effectively breaking all mirror symmetries. The fabrication of this metasurface is carried out using a modified slanted-etching system, which includes a wedged substrate and an Al_2O_3 screen with an aperture serving as an ion collimator. SEM images of the fabricated samples are depicted in the lower left of Fig. 17(a). The utilization of an ion collimator ensures that the left and right sidewalls exhibit nearly identical slant angles. Moreover, Liu *et al.*[104] have demonstrated novel slanted metagratings designed for large-angle and high-efficiency anomalous refraction in the visible spectrum. Through the introduction of out-of-plane asymmetry, the study reveals that meta-atoms with simple configurations exhibit comparable degrees of freedom as their topologically optimized counterparts. As a result, the slanted TiO_2 metagratings can effectively steer light to 80° with impressive relative efficiency (98.5%) and absolute efficiency (89.5%). Figure 17(b) illustrates the schematic of a TiO_2 metagrating, consisting of TiO_2 waveguides incorporating two types of asymmetries. In-plane asymmetry is introduced through the utilization of a conventional asymmetric dimer [top inset in Fig. 17(b)], strategically designed to govern intensity distributions among distinct diffraction orders. Simultaneously, out-of-plane asymmetry is achieved by tilting the sidewalls of gratings

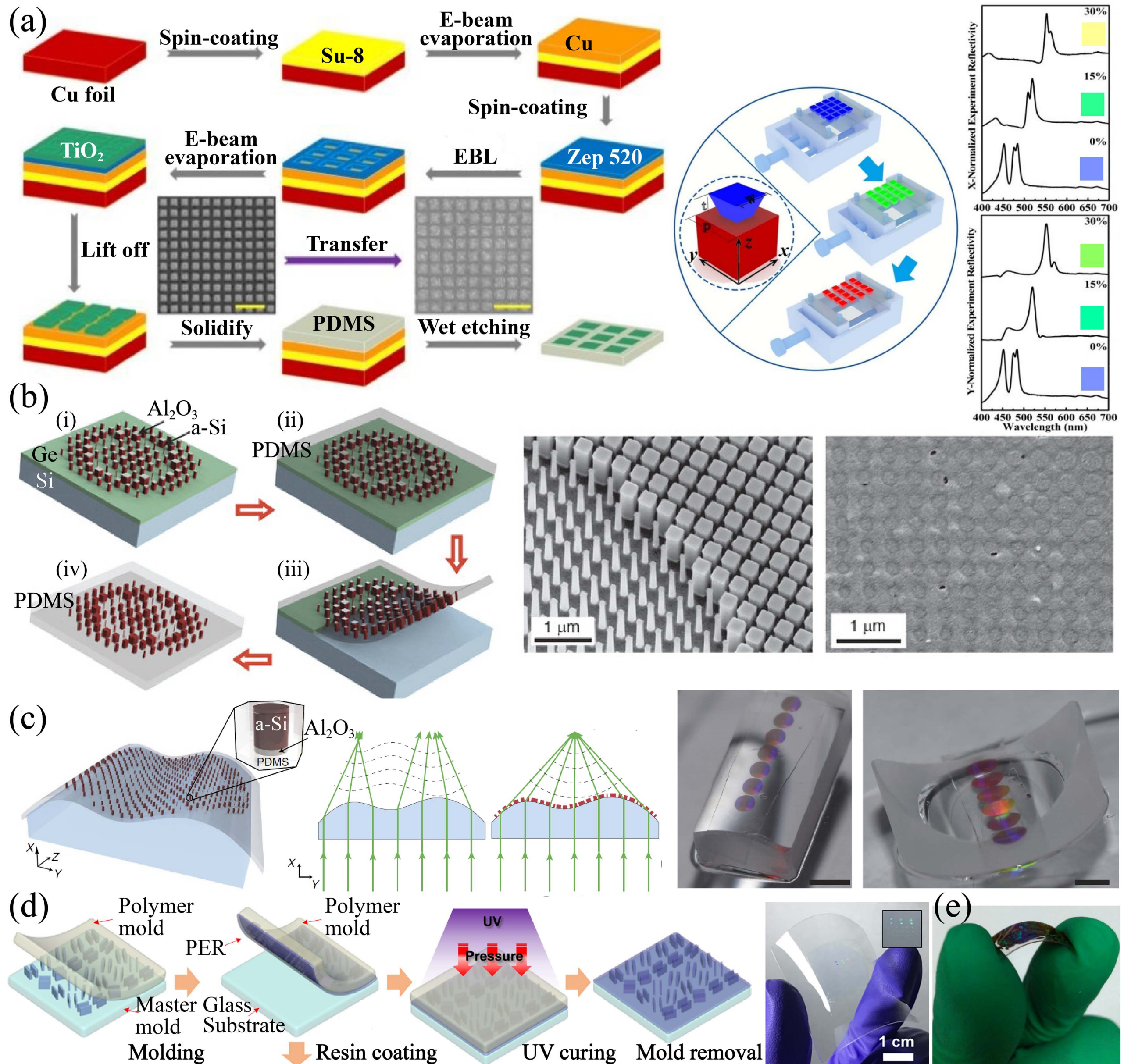

Fig. 16 Flexible dielectric metasurface nanofabrication. (a) Stretchable all-dielectric metasurfaces with polarization-insensitive and full-spectrum response are depicted in this study. The sample fabrication process is schematically illustrated on the left. The middle graphic portrays the conceptual image of the stretchable TiO_2 metasurface. The SEM images of the TiO_2 metasurface after the lift-off and transfer are provided as insets on the right. Scale bar: 1 μm. The reflection spectra as a function of strain. The insets show corresponding dynamic colors.[308] (b) The fabrication of highly tunable elastic dielectric metasurface lenses involves several key steps, as depicted in the schematic on the left. SEM images on the right provide a detailed view of the nano-posts before spin coating the initial PDMS layer and after they are embedded in PDMS.[309] (c) Decoupling the optical function from the geometrical form is achieved through conformal flexible dielectric metasurfaces. The schematic depicts a dielectric metasurface layer conforming to the surface of a transparent object with arbitrary geometry. The side view illustrates a thin dielectric metasurface layer altering its optical response to a desired one (middle). Optical images showcase two flexible metasurfaces conformed to a convex glass cylinder and a concave glass cylinder (right). Scale bar, 2 mm.[102] (d) The schematic on the left illustrates the nanoimprint procedure of dielectric metasurfaces with sub-100-nm resolution. On the right, the replication of the metasurface onto a flexible substrate.[253] (e) Flexible, all-dielectric metasurface fabricated via nanosphere lithography.[285]

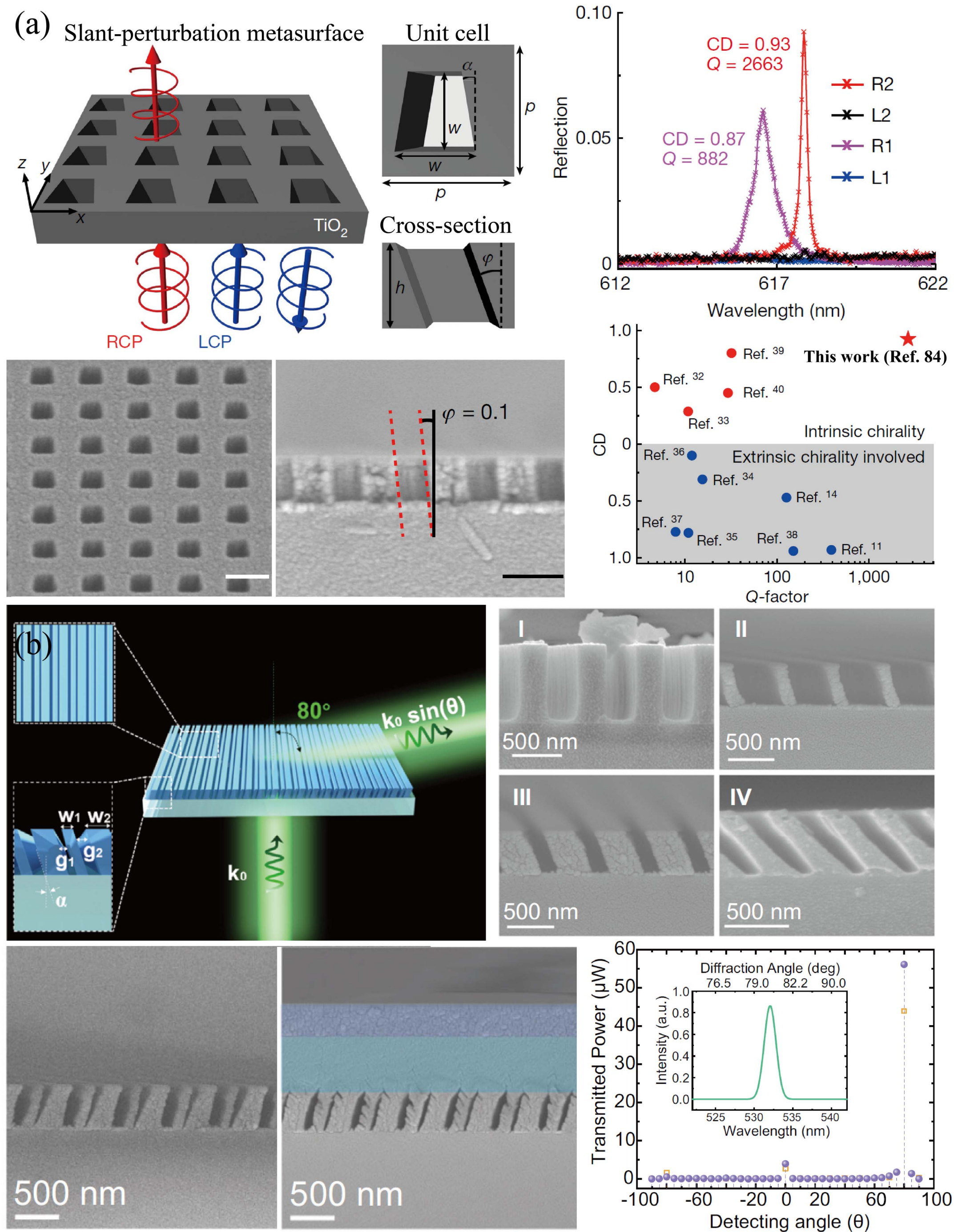

Fig. 17 Slanted dielectric metasurface nanofabrication. (a) Detection of intrinsic chiral bound states in the continuum (BICs). Schematic representation of the slant-perturbation metasurface designed to achieve intrinsic chiral BICs. Side-view (left) and cross-sectional (right) SEM images showcasing the fabricated metasurface. Scale bar: 300 nm. Reflection spectra measurements for two metasurface samples under LCP and RCP incidence, respectively (top right). Comparison of CDs and Q-factors between some typical experimental works and this work (right bottom).[84] (b) The illustration presents slanted TiO_2 metagratings designed for large-angle, high-efficiency anomalous refraction in the visible spectrum. The top left depicts the schematic of the slanted TiO_2 metagrating. In the top right, side-view SEM images showcase TiO_2 gratings with varying etching angles. The bottom section displays the improved TiO_2 metagrating, with SEM images depicting the structure before and after the re-deposition of the SiO_2/TiO_2 bilayer on the left. The right-bottom section provides experimentally recorded angle-dependent power distributions passing through the metagrating before (open squares) and after (dots) the redeposition.[104]

at an angle represented by α [bottom inset in Fig. 17(b)]. The lower left section of Fig. 17(b) presents side-view SEM images displaying the etched TiO_2 gratings with parallel sidewalls. This achievement is attributed to the utilization of a specially crafted angled aluminum holder featuring a tilting angle for sample mounting. Through the combined impact of this holder and a top aluminum net, the undesirable bending of the effective electric field near the sample surface has been successfully mitigated. This innovative setup facilitates the fabrication of high-quality slanted TiO_2 nanostructures. The lower right portion of Fig. 17(b) showcases tilt-view and side-view SEM images of the fabricated metagratings designed for anomalous refraction. Leveraging optimized etching and deposition technologies, a green laser has been deflected to an impressive 80° with a remarkably high absolute efficiency and relative efficiency of 83.6% and 94.0%, respectively, as depicted in the lower right section of Fig. 17(b). This methodology for creating slanted nanostructures represents a promising avenue in the realm of meta-devices and is poised to catalyze the development of new classes of high-performance nanophotonic systems.

4.4 High-aspect-ratio dielectric metasurface nanofabrication

High-aspect-ratio dielectric metasurface nanofabrication is dedicated to achieving high aspect ratios in dielectric structures, thereby enhancing their structural integrity and optical performance. While TiO_2 is widely employed in dielectric metasurface design and fabrication, most TiO_2 metasurface fabrication techniques rely on ALD, which is relatively slow and imposes limitations on the thickness and aspect ratio, typically below 600 nm and 15, respectively. Although the RIE process for TiO_2 has been under study for numerous years, the prior recipes only yield a sidewall with a tilt angle of $<75°$, significantly restricting applications in high-quality flat devices such as metalenses. In response to these challenges, Wang *et al.* introduced a top-down etching-based technology designed to create TiO_2 nanopillars with unprecedentedly high aspect ratios. This technology yields pillar heights of 1.5 μm and achieves approximately 90° vertical sidewalls. The researchers conducted experiments to demonstrate the effectiveness of this approach, showcasing a polarization-insensitive, broadband TiO_2 achromatic metalens tailored for applications in NIR biological imaging[101]. The demonstrated metalens exhibits that the spectral range of achromatism is substantially extended to the wavelength range of 650–1000 nm with an average efficiency of 77.1%–88.5% and a numerical aperture of 0.24–0.1 [right column of Fig. 18(a)]. Illustrated in the left image of Fig. 18(a), the fabrication process involves depositing a 1500-nm-thick TiO_2 membrane through E-beam evaporation, followed by EBL and RIE processes, to create TiO_2 nanostructures. The bottom SEM image of TiO_2 metalenses in Fig. 18(a) reveals that the nanopillars possess nearly perfect vertical sidewalls, with the measured tilt angle of sidewalls around 89°–90°. Additionally, Einck *et al.* presented a one-step additive manufacturing process for the fabrication of metalenses designed for visible wavelengths. This innovative approach utilizes NIL and a TiO_2 nanocrystal-based imprint material[310]. Nanostructures with aspect ratios exceeding 8 and critical dimensions smaller than 60 nm were successfully manufactured. The direct-imprint NIL process is illustrated in Fig. 18(b). It begins with the thermal curing of PDMS, after which the stamp is detached from the master and utilized directly for imprinting. Subsequently, metalenses are formed by imprinting a solution of TiO_2 nanocrystals and curing it using pulsed UV. Following UV curing, the stamp can be released. Cross-sectional SEM images in the inset of Fig. 18(b) reveal aspect ratios of up to 7.8 for the imprinted nano-posts. The predominant building blocks in metasurfaces, in general, are free-standing nanopillar meta-atoms. However, researchers have introduced an alternative metasurface geometry based on high-aspect-ratio via-holes, as illustrated in Fig. 18(c)[311]. They designed and characterized metalenses incorporating ultradeep via-holes in 5-μm-thick free-standing silicon membranes, achieving hole aspect ratios approaching 30:1. The fabrication process, as depicted in the bottom image of Fig. 18(c), utilizes EBL and RIE to pattern a SiO_2 hard mask on the device layer surface of a SOI chip, forming the desired holey metalens pattern. A deep Bosch process is subsequently employed to etch high-aspect-ratio holes into the device layer using the hard mask. SEM images of the sidewalls are displayed at the top of Fig. 18(c), while the cross-section of the fabricated metalens is presented in the middle of Fig. 18(c), demonstrating a tilt of the hole wall within 1°. Moreover, utilizing high-aspect-ratio silicon micropillars that exhibit wide transmission-phase tuning ranges with high transmission amplitudes, Wang *et al.* devised and manufactured a series of silicon metasurfaces to achieve efficient spin-multiplexed wavefront controls on THz waves[312]. The meta-atom is structured to include three layers [refer to the inset in Fig. 18(d)]: a high micro-pillar, a thick continuous substrate, and a micro-resonator. They constructed a metasurface comprising a periodic array of the designed meta-atoms, illustrated in Fig. 18(d), employing photolithography and deep RIE through the Bosch process on a thick silicon wafer. The desired patterns were transferred onto the wafer using the Bosch process, a time-multiplexed deep etching technique involving both etch and passivation phases. After carefully balancing these two phases, they successfully manufactured the desired metasurface, featuring high-aspect-ratio (approximately 20:1) microstructures with smooth surfaces, straight sidewalls, and precise alignment. The right column of Fig. 18(d) displays the top-view and bottom-view SEM images of the fabricated sample, respectively.

High-aspect-ratio nanostructures have also been demonstrated in GaAs[57] metagratings integrated on vertical-cavity surface-emitting lasers and HfO_2[144] metasurface optics down to the DUV region, among others.

5 Perspective and Outlook

In the past decade, metasurfaces, particularly dielectric metasurfaces, have experienced rapid development due to their lightweight and compact characteristics, driven by low absorption, low impedance, and absence of heat generation. The significant potential of high-performance dielectric metasurfaces lies in their ability to replace bulky optical elements, particularly metalenses in imaging systems. Researchers have developed highly efficient metalenses for the visible spectrum (e.g., GaN with efficiencies ranging from 50.6% to 91.6%)[151] and the NIR region (e.g., TiO_2 with efficiencies between 77.1% and 88.5%)[101]. Furthermore, using conventional chip fabrication methods such as DUV lithography, wafer-scale metalenses can be manufactured[268,324]. Compared to traditional optical element manufacturing, thousands of metalenses can be produced in a single batch, offering scalability and reduced costs. These metasurfaces also significantly reduce thickness and weight, resulting in

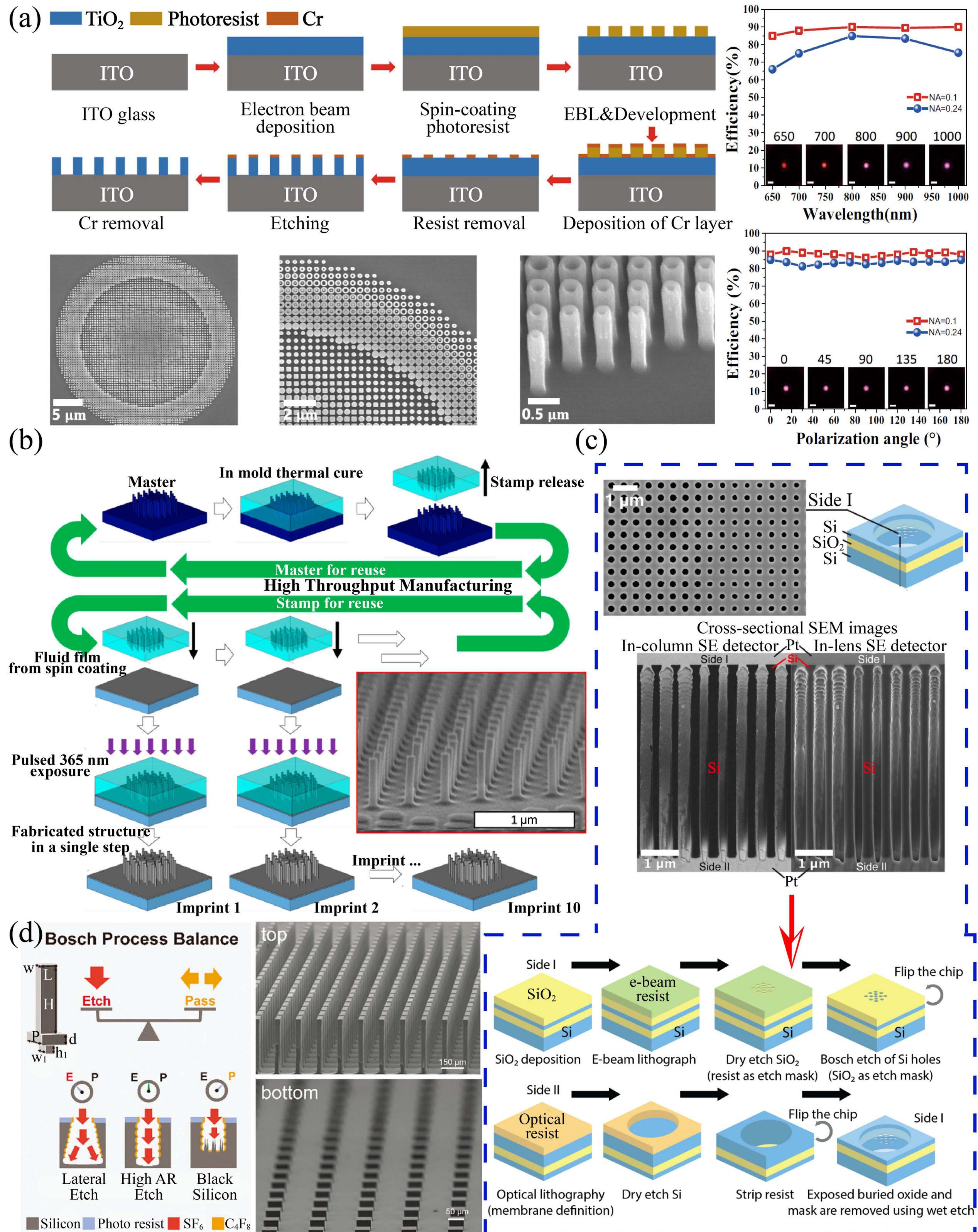

Fig. 18 High-aspect-ratio dielectric metasurface nanofabrication. (a) The diagram illustrates the fabrication process of a high-efficiency broadband achromatic metalens designed for near-infrared biological imaging. A highly directional etching process is employed to create TiO_2 nanostructures. The bottom-left images showcase SEM images of the achromatic metalens with varying resolutions, while the images on the right depict the focusing efficiencies of the developed TiO_2 metalenses.[101] (b) The nanoimprint lithography process is employed in the manufacturing

of high-aspect-ratio TiO_2 meta-atoms.[310] (c) A high-aspect-ratio inverse-designed holey metalens is depicted in the image. The top section displays an SEM image on the side I of the holey metalens. In the middle, cross-sectional SEM images offer a detailed view of a holey metalens. The bottom section outlines the fabrication workflow employed for the production of holey metalenses.[311] (d) Bifunctional manipulation is achieved through high-aspect-ratio dielectric metasurfaces. High-quality tri-layer meta-atoms with high aspect ratios (as shown in the inset) are produced using the Bosch process. The achievement of a high-aspect-ratio etch is only viable under these balanced conditions (depicted on the left). The top-view and bottom-view SEM images illustrate the fabricated metasurface (right).[312]

more compact and lightweight optical systems. Additionally, metalenses can be fabricated directly on top of CMOS chips due to their flat surfaces[325]. The integration based on commercial CMOS process will reduce production costs and improve yield. Figure 19 illustrates further advanced applications of dielectric metasurfaces. More detailed reviews about the applications of metasurfaces across various domains can be found in previous literature[326–329]. This miniaturization advantage of meta-devices has led to notable advancements in various applications, including aerial[330], terrestrial[331], and underwater[318,332] environments, particularly benefiting modern consumer optoelectronic devices such as augmented reality (AR), virtual reality (VR), and unmanned aerial vehicles[333], among others. In contrast to digital optoelectronic devices, there is considerable interest in optical analog signal processing due to the rising demand for extensive real-time data processing in the era of big data. For instance, one analog image processing method, edge detection based on dielectric metasurfaces, has been extensively studied in both classical optics[334–337] and quantum optics[338] due to its low power consumption and high-speed properties. In the realm of metasurfaces, materials serve as the cornerstone, manufacturing techniques form the framework, and applications constitute the outcomes. New materials are yet to be developed, which will pave the way for the advancement of additional manufacturing techniques based on these materials, thereby leading to the development of further applications.

5.1 Dielectric materials

This review explores the existing high-index dielectric materials and their associated nanofabrication technologies for high-performance applications. However, optical properties of meta-devices are still limited by the trade-off between refractive index and optical absorption. Further advancements in material science, particularly the creation of advanced dielectric materials exhibiting low loss and high refractive index across a broad

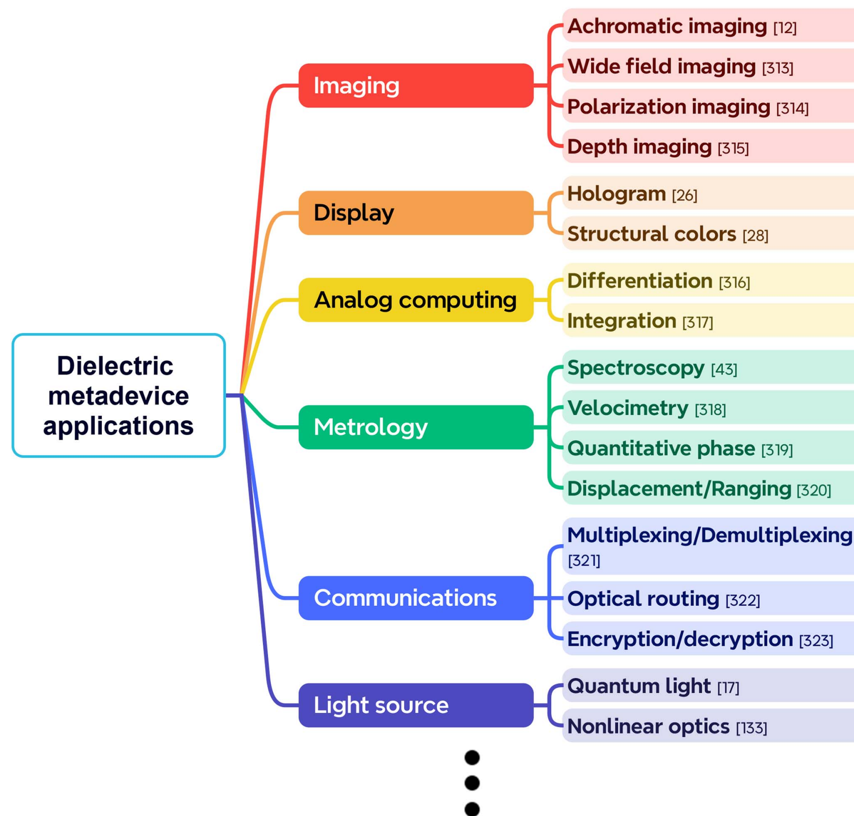

Fig. 19 Advanced applications, such as imaging[12, 313–315], display[26, 28], analog computing[316, 317], metrology[43, 318–320], communications[321–323], and light sources[17, 133] utilizing dielectric meta-devices, have emerged in the past years.

spectrum from UV to IR wavelengths, hold promise for enhancing metasurface performance. Furthermore, the emergence of multifunctional dielectric materials with tunable optical properties, including phase-change materials such as germanium antimony telluride ($Ge_2Sb_2Te_5$ or GST)[339], vanadium dioxide (VO_2)[340], and antimony trisulfide (Sb_2S_3)[341]; electro-optic materials like lithium niobate ($LiNbO_3$)[342]; and thermo-optic materials like silicon (Si)[343] and liquid crystals[344]; as well as electrical properties, such as ferroelectric materials like barium titanate ($BaTiO_3$)[345] and graphene[346]; magnetic properties, such as multiferroic materials like bismuth ferrite ($BiFeO_3$)[347]; and magneto-optic materials like yttrium iron garnet (YIG)[348], along with intensity-modulated nonlinear materials like metallic quantum wells[349–351], offers versatile options for metasurface fabrication and functionality enhancement. The combination of tunable properties in these materials has shown promising applications in dynamic, reconfigurable, and high-performance dielectric metasurfaces, including dynamic holograms[352], tunable imaging[353–355], active beam steering[356], and chirality tuning in several recent studies[341]. Simultaneously, hybrid structures that combine two or more distinct dielectric or metal materials allow for leveraging the advantages of both plasmonic and all-dielectric elements. For instance, they offer the strong field enhancement of plasmonic resonators along with the low-loss radiation channels of dielectric resonators, presenting an innovative approach to various nanophotonic applications. Compared with pure metallic and all-dielectric metasurfaces, the hybrid metasurface can expand the degrees of freedom for full-space light manipulation[103], optimize and enhance nonlinear light–matter interactions[357], engineer the meta-atom with a range of electromagnetic modes through the interplay between plasmon polaritons (SPP), MDs, and electric dipoles[222,292,358], and provide the high-performance multifunctionality for biosensors[359,360] and tunable optoelectronic devices[361]. Importantly, artificial-intelligence-driven design techniques can assist in overcoming the limitations of material properties in specific areas. We expect that advancements in high-index dielectric materials, characterized by high electro-optic coefficients, intrinsic nonlinearities, wide transparency windows, and compatibility with nanofabrication technologies, along with a deeper understanding of design principles, will facilitate the development of highly efficient optical devices and unlock new on-chip functionalities.

5.2 Nanofabrication techniques

The manufacturing processes of metasurfaces encompass various techniques, including standard nanolithography, advanced nanolithography, large-scale nanolithography, and extreme fabrication methods. Standard nanolithography, including EBL/FIB, remains pivotal in demonstrating innovative meta-optics concepts with intricate structures at an extreme scale level. It is essential for achieving breakthroughs in laboratory-based state-of-the-art fabrication techniques, such as multistep and grayscale lithography. However, advanced nanolithography alone is inadequate for commercial mass production. Consequently, researchers have developed alternative large-scale nanofabrication methods for dielectric metasurfaces, such as self-assembly, NIL, and DUV lithography. The favorability toward adopting automated wafer-scale lithography equipment, notably DUV scanners/steppers, has grown significantly, driven by their acknowledged cost-effectiveness and exceptional productivity. However, their spatial resolution is insufficient for defining the minute critical dimensions of visible metasurfaces operating at short wavelengths. Additionally, the fabrication expertise for DUV is currently limited to only a few research groups worldwide, which hinders the advancement of this promising technology. NIL, leveraging high-resolution master molds, represents a green wafer-scale lithography technology that offers high pattern fidelity and design flexibility. Exploring innovative processes, such as combining different preparation methods like photolithography and pattern transfer using master mold methods, holds promise for facilitating the preparation of more intricate nanostructures. This approach offers the potential for achieving more efficient and controllable nanostructure preparation.

The selection of a fabrication method depends on specific application requirements, including the desired pattern, resolution, and scalability. Each technique offers distinct advantages and is well-suited for particular nano-patterning tasks. Furthermore, optimizing existing nanofabrication methods to enhance production efficiency and material utilization and to reduce preparation costs remains the gold standard for metasurface fabrication. Undoubtedly, these advancements will propel metasurfaces toward widespread commercial applications and facilitate their broader accessibility within the academic and industrial communities.

5.3 Emerging technology and field

The journey from research to market represents one of the most promising emerging platforms for meta-optics, owing to its unique set of compelling properties: cost reduction, scalable manufacturing, reproducibility, and long-term stability of the technology, as well as the potential for compact integration of numerous components onto millimeter-sized chips. While some of the dielectric materials and nanofabrication technologies discussed in this review are still primarily in the realm of scientific research rather than serving as reliable commercial platforms for metasurfaces, there exists potential for advancement. With the collective effort of the scientific and industrial communities, we can envision that the establishment of a comprehensive, high-throughput, and cost-effective supply chain covering every aspect from materials to devices will facilitate the widespread integration of dielectric metasurfaces into commercial applications and fully unlock their potential.

Moreover, the transition from chip demonstration to wafer-scale production, or from wafer-scale production to the application of large-scale, small-volume chips, will emerge as the prevailing trend in the metasurface field. We believe that high-performance all-dielectric meta-devices/optics will emerge as a promising option for constructing near-future photonic platforms and will become a major driving force across various fields in the future, owing to the advancements in wafer-scale mass fabrication, as depicted in Fig. 20. These fields include display, optical sensors, aerospace, and others. For example, silicon metasurfaces with a high refractive index have demonstrated an increased gamut to around 181.8% of sRGB, 135.6% of Adobe RGB, and 97.2% of Rec.2020 (UHDTV)[28]. Combined with liquid crystals, TiO_2 metasurfaces have presented high-resolution (pixel size $\sim$1 μm) SLMs[362]. These advancements provide opportunities to develop the next generation of high-resolution, energy-efficient display technologies. Similarly, in optical sensor applications, particularly within the

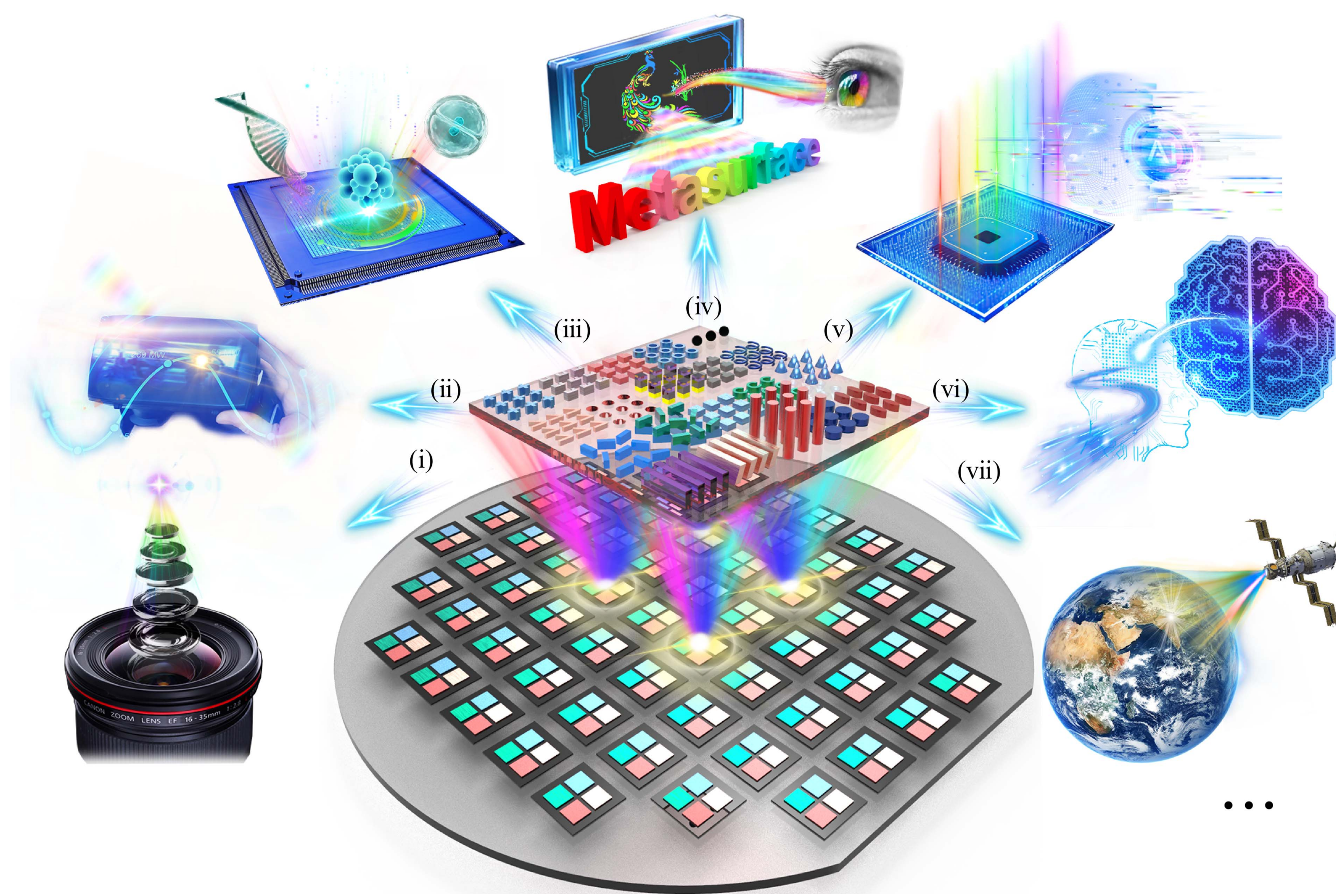

Fig. 20 Prospects for the bright future of all-dielectric metadevices/optics with wafer-scale mass fabrication, including (i) metalenses, (ii) AR and VR, (iii) optical sensors, (iv) color/holographic displays, (v) AI-based spectrometer/advanced imaging, (vi) telekinesis and telepathy, and (vii) satellite communications/LIDAR.

biosensor field, high-Q resonant a-Si-based dielectric metasurfaces combined with hyperspectral imaging have demonstrated an ultrasensitive label-free analytical platform for biosensing[47]. It is anticipated that the integration of dielectric metasurface-based optical sensor techniques with artificial intelligence (AI) will further enhance the capabilities and efficiency of detection. Furthermore, on-chip devices based on metasurfaces will facilitate the development of highly integrated and intelligent sensor platforms. When dielectric metasurfaces are combined with microfluidic technologies, integrated microfluidic chips gain the ability to manipulate both light and liquids, leading to significant advancements in biosensors[53] and display technologies[363]. Efficiently coupling light into and out of the metasurfaces within microfluidic channels is crucial and necessitates careful design of optical pathways, along with consideration of the refractive index matching between the metasurface, fluid, and substrate. Integrating metasurfaces into compact microfluidic devices without degrading their optical performance remains a significant challenge. Meanwhile, in the aerospace field, smart metasurfaces incorporating gyroscope sensors have shown potential for satellite communications[364]. Additionally, metasurface antennas for small satellites hold promise for providing high-speed data transmission and reception capabilities, reducing the size and weight of satellite communication systems, and lowering launch costs. These examples merely scratch the surface of the potential applications of metasurface technology. As technology progresses and innovates, the application domains of dielectric metasurfaces, particularly those fabricated on a wafer-scale, are anticipated to expand and deepen. This trend is expected to yield further surprises and breakthroughs across various fields.

Conflict of Interest

The authors declare no conflict of interest.

Acknowledgments

This work was supported by the National Key Research and Development Project of China (Nos. 2022YFA1404700, 2023YFB2806700, and 2021YFA1400802), National Natural Science Foundation of China (Nos. 6233000076, 12334016, 12025402, 62125501, 11934012, 12261131500, 92250302, and 62375232), Shenzhen Fundamental Research Project (Nos. JCYJ20210324120402006, JCYJ20220818102218040, and GXWD20220817145518001), and University Grants Committee/Research Grants Council of the Hong Kong Special Administrative Region, China (Project No. AoE/P-502/20; CRF Project Nos. C5031-22G and C1015-21E; GRF Project Nos. CityU15303521 and CityU11305223; and Germany/Hong Kong Joint Research Scheme: GCityU101/22),

and Project of City University of Hong Kong (Nos. 9380131, 9610628, and 7005867).

References

1. D. R. Smith, J. B. Pendry, and M. C. K. Wiltshire, "Metamaterials and negative refractive index," *Science* **305**, 788 (2004).
2. D. Schurig *et al.*, "Metamaterial electromagnetic cloak at microwave frequencies," *Science* **314**, 977 (2006).
3. S. Xiao *et al.*, "Loss-free and active optical negative-index metamaterials," *Nature* **466**, 735 (2010).
4. N. Yu *et al.*, "Light propagation with phase discontinuities: generalized laws of reflection and refraction," *Science* **334**, 333 (2011).
5. A. V. Kildishev, A. Boltasseva, and V. M. Shalaev, "Planar photonics with metasurfaces," *Science* **339**, 1232009 (2013).
6. N. Yu and F. Capasso, "Flat optics with designer metasurfaces," *Nat. Mater.* **13**, 139 (2014).
7. T. J. Cui *et al.*, "Roadmap on electromagnetic metamaterials and metasurfaces," *J. Phys.* to be published (2024).
8. H.-H. Hsiao, C. H. Chu, and D. P. Tsai, "Fundamentals and applications of metasurfaces," *Small Methods* **1**, 1600064 (2017).
9. Y. Yang *et al.*, "Integrated metasurfaces for re-envisioning a near-future disruptive optical platform," *Light Sci. Appl.* **12**, 152 (2023).
10. S. So *et al.*, "Revisiting the design strategies for metasurfaces: fundamental physics, optimization, and beyond," *Adv. Mater.* **35**, 2206399 (2023).
11. S. Wang *et al.*, "Broadband achromatic optical metasurface devices," *Nat. Commun.* **8**, 1 (2017).
12. S. Wang *et al.*, "A broadband achromatic metalens in the visible," *Nat. Nanotechnol.* **13**, 227 (2018).
13. W. T. Chen *et al.*, "A broadband achromatic metalens for focusing and imaging in the visible," *Nat. Nanotechnol.* **13**, 220 (2018).
14. L. Yu *et al.*, "Spin angular momentum controlled multifunctional all-dielectric metasurface doublet," *Laser Photon. Rev.* **14**, 1900324 (2020).
15. M. Khorasaninejad *et al.*, "Metalenses at visible wavelengths: diffraction-limited focusing and subwavelength resolution imaging," *Science* **352**, 1190 (2016).
16. C. Wang *et al.*, "Miniature two-photon microscopic imaging using dielectric metalens," *Nano Lett.* **23**, 8256 (2023).
17. L. Li *et al.*, "Metalens-array–based high-dimensional and multiphoton quantum source," *Science* **368**, 1487 (2020).
18. J. Zhou *et al.*, "Broadband photonic spin Hall meta-lens," *ACS Nano* **12**, 82 (2018).
19. M. K. Chen and T. Tanaka, "Metalenses for revolutionary imaging," *Photonics Insights* **2**, C01 (2023).
20. M. Zhao *et al.*, "Phase characterisation of metalenses," *Light-Sci. Appl.* **10**, 52 (2021).
21. G. Zheng *et al.*, "Metasurface holograms reaching 80% efficiency," *Nat. Nanotechnol.* **10**, 308 (2015).
22. Y. Gao *et al.*, "Nonlinear holographic all-dielectric metasurfaces," *Nano Lett.* **18**, 8054 (2018).
23. G. Qu *et al.*, "Reprogrammable meta-hologram for optical encryption," *Nat. Commun.* **11**, 5484 (2020).
24. X. Ni, A. V. Kildishev, and V. M. Shalaev, "Metasurface holograms for visible light," *Nat. Commun.* **4**, 2807 (2013).
25. J. Li *et al.*, "Addressable metasurfaces for dynamic holography and optical information encryption," *Sci. Adv.* **4**, eaar6768 (2018).
26. Z. Li *et al.*, "Dielectric meta-holograms enabled with dual magnetic resonances in visible light," *ACS Nano* **11**, 9382 (2017).
27. K. Kumar *et al.*, "Printing colour at the optical diffraction limit," *Nat. Nanotechnol.* **7**, 557 (2012).
28. W. Yang *et al.*, "All-dielectric metasurface for high-performance structural color," *Nat. Commun.* **11**, 1864 (2020).
29. W. Yang *et al.*, "Dynamic bifunctional metasurfaces for holography and color display," *Adv. Mater.* **33**, 2101258 (2021).
30. S. Sun *et al.*, "All-dielectric full-color printing with TiO_2 metasurfaces," *ACS Nano* **11**, 4445 (2017).
31. B. Yang *et al.*, "Ultrahighly saturated structural colors enhanced by multipolar-modulated metasurfaces," *Nano Lett.* **19**, 4221 (2019).
32. X. Duan, S. Kamin, and N. Liu, "Dynamic plasmonic colour display," *Nat. Commun.* **8**, 14606 (2017).
33. Y. Wu *et al.*, "Dynamic structural colors based on all-dielectric Mie resonators," *Adv. Opt. Mater.* **9**, 2002126 (2021).
34. Y. Li *et al.*, "Recent progress on structural coloration," *Photonics Insights* **3**, R03 (2024).
35. M. I. Shalaev *et al.*, "High-efficiency all-dielectric metasurfaces for ultracompact beam manipulation in transmission mode," *Nano Lett.* **15**, 6261 (2015).
36. R. C. Devlin *et al.*, "Arbitrary spin-to–orbital angular momentum conversion of light," *Science* **358**, 896 (2017).
37. F. Mei *et al.*, "Cascaded metasurfaces for high-purity vortex generation," *Nat. Commun.* **14**, 6410 (2023).
38. H. Zhang *et al.*, "All-dielectric metasurface-enabled multiple vortex emissions," *Adv. Mater.* **34**, 2109255 (2022).
39. J. Zhou *et al.*, "Generation of Airy vortex and Airy vector beams based on the modulation of dynamic and geometric phases," *Opt. Lett.* **40**, 3193 (2015).
40. Q. Chen *et al.*, "Highly efficient vortex generation at the nanoscale," *Nat. Nanotechnol.* (2024).
41. Z. Yang *et al.*, "Miniaturization of optical spectrometers," *Science* **371**, eabe0722 (2021).
42. G. Cai *et al.*, "Compact angle-resolved metasurface spectrometer," *Nat. Mater.* **23**, 71 (2024).
43. M. Faraji-Dana *et al.*, "Compact folded metasurface spectrometer," *Nat. Commun.* **9**, 4196 (2018).
44. C. Wu *et al.*, "Fano-resonant asymmetric metamaterials for ultrasensitive spectroscopy and identification of molecular monolayers," *Nat. Mater.* **11**, 69 (2012).
45. A. Tittl *et al.*, "Imaging-based molecular barcoding with pixelated dielectric metasurfaces," *Science* **360**, 1105 (2018).
46. A. E. Cetin *et al.*, "Handheld high-throughput plasmonic biosensor using computational on-chip imaging," *Light-Sci. Appl.* **3**, e122 (2014).
47. F. Yesilkoy *et al.*, "Ultrasensitive hyperspectral imaging and biodetection enabled by dielectric metasurfaces," *Nat. Photonics* **13**, 390 (2019).
48. A. Belushkin *et al.*, "Rapid and digital detection of inflammatory biomarkers enabled by a novel portable nanoplasmonic imager," *Small* **16**, 1906108 (2020).
49. F. U. Richter *et al.*, "Gradient high-Q dielectric metasurfaces for broadband sensing and control of vibrational light-matter coupling," *Adv. Mater.*, 2314279 (2020).
50. D. Rodrigo *et al.*, "Mid-infrared plasmonic biosensing with graphene," *Science* **349**, 165 (2015).
51. R. Adato *et al.*, "Ultra-sensitive vibrational spectroscopy of protein monolayers with plasmonic nanoantenna arrays," *Proc. Natl. Acad. Sci. USA* **106**, 19227 (2009).
52. H. Altug *et al.*, "Advances and applications of nanophotonic biosensors," *Nat. Nanotechnol.* **17**, 5 (2022).
53. Y. Jahani *et al.*, "Imaging-based spectrometer-less optofluidic biosensors based on dielectric metasurfaces for detecting extracellular vesicles," *Nat. Commun.* **12**, 3246 (2021).
54. N. Liu *et al.*, "Infrared perfect absorber and its application as plasmonic sensor," *Nano Lett.* **10**, 2342 (2010).
55. N. Liu *et al.*, "Nanoantenna-enhanced gas sensing in a single tailored nanofocus," *Nat. Mater.* **10**, 631 (2011).
56. J. Park *et al.*, "All-solid-state spatial light modulator with independent phase and amplitude control for three-dimensional LiDAR applications," *Nat. Nanotechnol.* **16**, 69 (2021).

57. M. Juodėnas *et al.*, "High-angle deflection of metagrating-integrated laser emission for high-contrast microscopy," *Light-Sci. Appl.* **12**, 251 (2023).
58. Y.-W. Huang *et al.*, "Gate-tunable conducting oxide metasurfaces," *Nano Lett.* **16**, 5319 (2016).
59. J. Zhou *et al.*, "A spin controlled wavefront shaping metasurface with low dispersion in visible frequencies," *Nanoscale* **11**, 17111 (2019).
60. J. Zhou *et al.*, "Spin-dependent manipulating of vector beams by tailoring polarization," *Sci. Rep.* **6**, 34276 (2016).
61. S. Sun *et al.*, "High-efficiency broadband anomalous reflection by gradient meta-surfaces," *Nano Lett.* **12**, 6223 (2012).
62. N. Meinzer, W. L. Barnes, and I. R. Hooper, "Plasmonic meta-atoms and metasurfaces," *Nat. Photonics* **8**, 889 (2014).
63. Q. Xu *et al.*, "Meta-optics inspired surface plasmon devices," *Photonics Insights* **2**, R02 (2023).
64. P. Genevet *et al.*, "Recent advances in planar optics: from plasmonic to dielectric metasurfaces," *Optica* **4**, 139 (2017).
65. E. Hutter and J. H. Fendler, "Exploitation of localized surface plasmon resonance," *Adv. Mater.* **16**, 1685 (2004).
66. Y. Wu *et al.*, "TiO_2 metasurfaces: from visible planar photonics to photochemistry," *Sci. Adv.* **5**, eaax0939 (2019).
67. R. C. Devlin *et al.*, "Broadband high-efficiency dielectric metasurfaces for the visible spectrum," *Proc. Natl. Acad. Sci. USA* **113**, 10473 (2016).
68. M. Khorasaninejad *et al.*, "Visible wavelength planar metalenses based on titanium dioxide," *IEEE J. Sel. Top. Quantum Electron.* **23**, 43 (2016).
69. J. Kim *et al.*, "Dynamic hyperspectral holography enabled by inverse-designed metasurfaces with oblique helicoidal cholesterics," *Adv. Mater.* **8**, 2311785 (2024).
70. S. Sun *et al.*, "Real-time tunable colors from microfluidic reconfigurable all-dielectric metasurfaces," *ACS Nano* **12**, 2151 (2018).
71. L. Jin *et al.*, "Dielectric multi-momentum meta-transformer in the visible," *Nat. Commun.* **10**, 4789 (2019).
72. S. Sun *et al.*, "All-dielectric meta-reflectarray for efficient control of visible light," *Ann. Phys. Berlin* **530**, 1700418 (2018).
73. Z. Zhou *et al.*, "Efficient silicon metasurfaces for visible light," *ACS Photonics* **4**, 544 (2017).
74. A. L. Holsteen, A. F. Cihan, and M. L. Brongersma "Temporal color mixing and dynamic beam shaping with silicon metasurfaces," *Science* **365**, 257 (2019).
75. A. Zhan *et al.*, "Low-contrast dielectric metasurface optics," *ACS Photonics* **3**, 209 (2016).
76. S. Colburn, A. Zhan, and A. Majumdar, "Metasurface optics for full-color computational imaging," *Sci. Adv.* **4**, eaar2114 (2018).
77. J. Kim *et al.*, "Photonic encryption platform via dual-band vectorial metaholograms in the ultraviolet and visible," *ACS Nano* **16**, 3546 (2022).
78. S. Liu *et al.*, "An all-dielectric metasurface as a broadband optical frequency mixer," *Nat. Commun.* **9**, 2507 (2018).
79. S. Liu *et al.*, "Resonantly enhanced second-harmonic generation using III–V semiconductor all-dielectric metasurfaces," *Nano Lett.* **16**, 5426 (2016).
80. A. I. Kuznetsov *et al.*, "Optically resonant dielectric nanostructures," *Science* **354**, aag2472 (2016).
81. M. V. Gorkunov, A. A. Antonov, and Y. S. Kivshar, "Metasurfaces with maximum chirality empowered by bound states in the continuum," *Phys. Rev. Lett.* **125**, 093903 (2020).
82. C. Huang *et al.*, "Ultrafast control of vortex microlasers," *Science* **367**, 1018 (2020).
83. X. Zhang *et al.*, "Chiral emission from resonant metasurfaces," *Science* **377**, 1215 (2022).
84. Y. Chen *et al.*, "Observation of intrinsic chiral bound states in the continuum," *Nature* **613**, 474 (2023).
85. K. Koshelev *et al.*, "Subwavelength dielectric resonators for nonlinear nanophotonics," *Science* **367**, 288 (2020).
86. Y. Liang *et al.*, "Bound states in the continuum in anisotropic plasmonic metasurfaces," *Nano Lett.* **20**, 6351 (2020).
87. J. Wang *et al.*, "Optical bound states in the continuum in periodic structures: mechanisms, effects, and applications," *Photonics Insights* **3**, R01 (2024).
88. S. M. Sze, *Semiconductor Devices: Physics and Technology* (John Wiley & Sons, 2008).
89. C. Wu *et al.*, "Spectrally selective chiral silicon metasurfaces based on infrared Fano resonances," *Nat. Commun.* **5**, 3892 (2014).
90. C. C. Chen *et al.*, "Uniaxial-isotropic metamaterials by three-dimensional split-ring resonators," *Adv. Opt. Mater.* **3**, 44 (2015).
91. V. R. Manfrinato *et al.*, "Resolution limits of electron-beam lithography toward the atomic scale," *Nano Lett.* **13**, 1555 (2013).
92. O. Rogov *et al.*, "FIB-fabricated complex-shaped 3D chiral photonic silicon nanostructures," *J. Microsc.* **268**, 254 (2017).
93. J. Berzins *et al.*, "Direct and high-throughput fabrication of Mie-resonant metasurfaces *via* single-pulse laser interference," *ACS Nano* **14**, 6138 (2020).
94. N. Bonod, "Large-scale dielectric metasurfaces," *Nat. Mater.* **14**, 664 (2015).
95. B. Leng, M. Chen, and T. Dinping,"Design, fabrication, and imaging of meta-devices," *Acta Opt. Sin* **43**, 11 (2023).
96. K.-J. Byeon and H. Lee, "Recent progress in direct patterning technologies based on nano-imprint lithography," *Eur. Phys. J. Appl. Phys.* **59**, 10001 (2012).
97. P. Molet *et al.*, "Large area metasurfaces made with spherical silicon resonators," *Nanophotonics* **9**, 943 (2020).
98. P. Moitra *et al.*, "Large-scale all-dielectric metamaterial perfect reflectors," *ACS Photonics* **2**, 692 (2015).
99. X. Yin *et al.*, "Roll-to-roll dielectric metasurfaces," in *Metamaterials, Metadevices, and Metasystems 2020* (SPIE, 2020) p. 114600S.
100. N. Li *et al.*, "Large-area pixelated metasurface beam deflector on a 12-inch glass wafer for random point generation," *Nanophotonics* **8**, 1855 (2019).
101. Y. Wang *et al.*, "High-efficiency broadband achromatic metalens for near-IR biological imaging window," *Nat. Commun.* **12**, 5560 (2021).
102. S. M. Kamali *et al.*, "Decoupling optical function and geometrical form using conformal flexible dielectric metasurfaces," *Nat. Commun.* **7**, 11618 (2016).
103. L. Deng *et al.*, "Bilayer-metasurface design, fabrication, and functionalization for full-space light manipulation," *Adv. Opt. Mater.* **10**, 2102179 (2022).
104. Y. Liu *et al.*, "Slanted TiO_2 metagratings for large-angle, high-efficiency anomalous refraction in the visible," *Laser Photon. Rev.* 2200712 (2023).
105. K. Koshelev and Y. Kivshar, "Dielectric resonant metaphotonics," *ACS Photonics* **8**, 102 (2020).
106. W. Liu *et al.*, "Dielectric resonance-based optical metasurfaces: from fundamentals to applications," *Iscience* **23**, 101868 (2020).
107. D. G. Baranov *et al.*, "All-dielectric nanophotonics: the quest for better materials and fabrication techniques," *Optica* **4**, 814 (2017).
108. V.-C. Su *et al.*, "Advances in optical metasurfaces: fabrication and applications," *Opt. Express* **26**, 13148 (2018).
109. B. Leng *et al.*, "Meta-device: advanced manufacturing," *Light Adv. Manuf.* **5**, 117 (2024).
110. G. Mie, "Beiträge zur Optik trüber Medien, speziell kolloidaler Metallösungen," *Ann. Phys. Berlin* **330**, 377 (1908).
111. L. Huang *et al.*, "Resonant leaky modes in all-dielectric metasystems: fundamentals and applications," *Phys. Rep.* **1008**, 1 (2023).
112. L. Huang *et al.*, "Ultrahigh-Q guided mode resonances in an all-dielectric metasurface," *Nat. Commun.* **14**, 3433 (2023).

113. D. Jeon and J. Rho "Quasi-trapped guided mode in a metasurface waveguide for independent control of multiple nonlocal modes," *ACS Photonics* **11**, 703 (2024).
114. Z. Li *et al.*, "Controlling propagation and coupling of waveguide modes using phase-gradient metasurfaces," *Nat. Nanotechnol.* **12**, 675 (2017).
115. L. Huang *et al.*, "Ultrahigh-Q guided mode resonances in an all-dielectric metasurface," *Nat. Commun.* **14**, 3433 (2023).
116. G. W. Castellanos, P. Bai, and J. G. Rivas, "Lattice resonances in dielectric metasurfaces," *J. Appl. Phys.* **125**, 213105 (2019).
117. V. E. Babicheva and A. B. Evlyukhin, "Multipole lattice effects in high refractive index metasurfaces," *J. Appl. Phys.* **129**, 040902 (2021).
118. A. Arbabi, M. Bagheri, and A. Faraon,"Dielectric metasurfaces for complete control of phase and polarization with subwavelength spatial resolution and high transmission," *Nat. Nanotechnol.* **10**, 937 (2015).
119. S. Divitt *et al.*, "Ultrafast optical pulse shaping using dielectric metasurfaces," *Science* **364**, 890 (2019).
120. D. Lin *et al.*, "Dielectric gradient metasurface optical elements," *Science* **345**, 298 (2014).
121. Z. Dong *et al.*, "Printing beyond sRGB color gamut by mimicking silicon nanostructures in free-space," *Nano Lett.* **17**, 7620 (2017).
122. P. Lalanne *et al.*, "Blazed binary subwavelength gratings with efficiencies larger than those of conventional échelette gratings," *Opt. Lett.* **23**, 1081 (1998).
123. M. Khorasaninejad *et al.*, "Polarization-insensitive metalenses at visible wavelengths," *Nano Lett.* **16**, 7229 (2016).
124. Y. Eliezer *et al.*, "Suppressing meta-holographic artifacts by laser coherence tuning," *Light-Sci. Appl.* **10**, 104 (2021).
125. G. Qu *et al.*, "All-dielectric metasurface empowered optical-electronic hybrid neural networks," *Laser Photon. Rev.* **16**, 2100732 (2022).
126. J. Kim *et al.*, "Metasurface holography reaching the highest efficiency limit in the visible via one-step nanoparticle-embedded-resin printing," *Laser Photon. Rev.* **16**, 2200098 (2022).
127. S. So *et al.*, "Multicolor and 3D holography generated by inverse-designed single-cell metasurfaces," *Adv. Mater.* **35**, 2208520 (2023).
128. M. A. Naveed *et al.*, "Single-step fabricable flexible metadisplays for sensitive chemical/biomedical packaging security and beyond," *ACS Appl. Mater. Interfaces* **14**, 31194 (2022).
129. A. Ji *et al.*, "Quantitative phase contrast imaging with a nonlocal angle-selective metasurface," *Nat. Commun.* **13**, 7848 (2022).
130. Y. Luo *et al.*, "Varifocal metalens for optical sectioning fluorescence microscopy," *Nano Lett.* **21**, 5133 (2021).
131. H. Ren *et al.*, "Metasurface orbital angular momentum holography," *Nat. Commun.* **10**, 2986 (2019).
132. H. Liu *et al.*, "Dielectric metasurface from solution-phase epitaxy of ZnO nanorods for subtractive color filter application," *Adv. Opt. Mater.* **9**, 2001670 (2021).
133. M. L. Tseng *et al.*, "Vacuum ultraviolet nonlinear metalens," *Sci. Adv.* **8**, eabn5644 (2022).
134. Z.-X. Zhou *et al.*, "Germanium metasurfaces with lattice Kerker effect in near-infrared photodetectors," *ACS Nano* **16**, 5994 (2022).
135. A. Leitis *et al.*, "Angle-multiplexed all-dielectric metasurfaces for broadband molecular fingerprint retrieval," *Sci. Adv.* **5**, eaaw2871 (2019).
136. J.-S. Park *et al.*, "All-glass 100 mm diameter visible metalens for imaging the cosmos," *ACS nano* **18**, 3187 (2024).
137. M. Sakakura *et al.*, "Ultralow-loss geometric phase and polarization shaping by ultrafast laser writing in silica glass," *Light-Sci. Appl.* **9**, 15 (2020).
138. Y. Lei *et al.*, "Efficient ultrafast laser writing with elliptical polarization," *Light Sci. Appl.* **12**, 74 (2023).
139. L. Hale *et al.*, "Perfect absorption in GaAs metasurfaces near the bandgap edge," *Opt. Express* **28**, 35284 (2020).
140. O. Mitrofanov *et al.*, "Perfectly absorbing dielectric metasurfaces for photodetection," *APL Phontonics* **5**, 101304 (2020).
141. J. C. Ginn *et al.*, "Realizing optical magnetism from dielectric metamaterials," *Phys. Rev. Lett.* **108**, 097402 (2012).
142. S. Zhang *et al.*, "Solid-immersion metalenses for infrared focal plane arrays," *Appl. Phys. Lett.* **113**, 111104 (2018).
143. B. Neuner *et al.*, "Efficient infrared thermal emitters based on low-albedo polaritonic meta-surfaces," *Appl. Phys. Lett.* **102**, 211111 (2013).
144. C. Zhang *et al.*, "Low-loss metasurface optics down to the deep ultraviolet region," *Light-Sci. Appl.* **9**, 55 (2020).
145. J. Kim *et al.*, "One-step printable platform for high-efficiency metasurfaces down to the deep-ultraviolet region," *Light-Sci. Appl.* **12**, 68 (2023).
146. K. Huang *et al.*, "Ultraviolet metasurfaces of ≈80% efficiency with antiferromagnetic resonances for optical vectorial anti-counterfeiting," *Laser Photon. Rev.* **13**, 1800289 (2019).
147. W. M. Moreau, *Semiconductor Lithography: Principles, Practices, and Materials* (Springer Science & Business Media, 2012).
148. Y. Chen and A. Pepin, "Nanofabrication: conventional and non-conventional methods," *Electrophoresis* **22**, 187 (2001).
149. C. Vieu *et al.*, "Electron beam lithography: resolution limits and applications," *Appl. Surf. Sci.* **164**, 111 (2000).
150. W. Wan *et al.*, "Tunable full-color vectorial meta-holography," *Adv. Opt. Mater.* **10**, 2201478 (2022).
151. B. H. Chen *et al.*, "GaN metalens for pixel-level full-color routing at visible light," *Nano Lett.* **17**, 6345 (2017).
152. W. Wan *et al.*, "Multiplexing vectorial holographic images with arbitrary metaholograms," *Adv. Opt. Mater.* **9**, 2100626 (2021).
153. Y. Bao *et al.*, "Full-colour nanoprint-hologram synchronous metasurface with arbitrary hue-saturation-brightness control," *Light-Sci. Appl.* **8**, 95 (2019).
154. W. Yue *et al.*, "Highly reflective subtractive color filters capitalizing on a silicon metasurface integrated with nanostructured aluminum mirrors," *Laser Photon. Rev.* **11**, 1600285 (2017).
155. Y. Wu *et al.*, "Self-cleaning titanium dioxide metasurfaces with UV irradiation," *Laser Photon. Rev.* **15**, 2000330 (2021).
156. P. Lalanne *et al.*, "Design and fabrication of blazed binary diffractive elements with sampling periods smaller than the structural cutoff," *JOSA A* **16**, 1143 (1999).
157. H. Sroor *et al.*, "High-purity orbital angular momentum states from a visible metasurface laser," *Nat. Photonics* **14**, 498 (2020).
158. V. Mikhelashvili and G. Eisenstein, "Effects of annealing conditions on optical and electrical characteristics of titanium dioxide films deposited by electron beam evaporation," *J. Appl. Phys.* **89**, 3256 (2001).
159. S. Khadir *et al.*, "Metasurface optical characterization using quadriwave lateral shearing interferometry," *ACS Photonics* **8**, 603 (2021).
160. S. Reyntjens and R. Puers, "A review of focused ion beam applications in microsystem technology," *J. Micromech. Microeng.* **11**, 287 (2001).
161. K. Arshak and M. Mihov, "State-of-the-art of focused ion beam nanolithography," *J. Optoelectron. Adv. Mater.* **7**, 193 (2005).
162. J. Li and Z. Liu, "Focused-ion-beam-based nano-kirigami: from art to photonics," *Nanophotonics* **7**, 1637 (2018).
163. P. Li *et al.*, "Recent advances in focused ion beam nanofabrication for nanostructures and devices: Fundamentals and applications," *Nanoscale* **13**, 1529 (2021).
164. D. Tua *et al.*, "Imaging-based intelligent spectrometer on a plasmonic rainbow chip," *Nat. Commun.* **14**, 1902 (2023).
165. V. Garg, R. G. Mote, and J. Fu, "Focused ion beam direct fabrication of subwavelength nanostructures on silicon for multicolor generation," *Adv. Mater. Technol.* **3**, 1800100 (2018).

166. M. V. Gorkunov *et al.*, "Chiral visible light metasurface patterned in monocrystalline silicon by focused ion beam," *Sci. Rep.* **8**, 11623 (2018).
167. A. Karvounis *et al.*, "All-dielectric phase-change reconfigurable metasurface," *Appl. Phys. Lett.* **109**, 051103 (2016).
168. M. Semmlinger *et al.*, "Vacuum ultraviolet light-generating metasurface," *Nano Lett.* **18**, 5738 (2018).
169. A. Karvounis *et al.*, "Nanomechanically reconfigurable all-dielectric metasurfaces for sub-GHz optical modulation," (2016).
170. Y. Khan *et al.*, "Fabrication and investigation of spectral properties of a dielectric slab waveguide photonic crystal based Fano-filter," *Crystals* **12**, 226 (2022).
171. E. Bermúdez-Ureña and U. Steiner, "Self-rolled multilayer metasurfaces," *ACS Photonics* **6**, 2198 (2019).
172. M. L. Tseng *et al.*, "Stress-induced 3D chiral fractal metasurface for enhanced and stabilized broadband near-field optical chirality," *Adv. Opt. Mater.* **7**, 1900617 (2019).
173. C. Wan *et al.*, "A selective metasurface absorber with an amorphous carbon interlayer for solar thermal applications," *Nano Energy* **26**, 392 (2016).
174. P. D. Terekhov *et al.*, "Enhanced absorption in all-dielectric metasurfaces due to magnetic dipole excitation," *Sci. Rep.* **9**, 3438 (2019).
175. S. R. Brueck, "Optical and interferometric lithography - nanotechnology enablers," *Proc. IEEE* **93**, 1704 (2005).
176. J.-H. Seo *et al.*, "Nanopatterning by laser interference lithography: applications to optical devices," *J. Nanosci. Nanotechnol.* **14**, 1521 (2014).
177. C. B. Arnold, P. Serra, and A. Piqué, "Laser direct-write techniques for printing of complex materials," *MRS Bull.* **32**, 23 (2007).
178. K. Hon, L. Li, and I. M. Hutchings, "Direct writing technology—advances and developments," *CIRP Annals* **57**, 601 (2008).
179. Y.-L. Zhang *et al.*, "Designable 3D nanofabrication by femtosecond laser direct writing," *Nano Today* **5**, 435 (2010).
180. M. Sakakura *et al.*, "Ultralow-loss geometric phase and polarization shaping by ultrafast laser writing in silica glass," *Light Sci. Appl.* **9**, 1 (2020).
181. Y. Lei *et al.*, "Ultrafast laser writing in different types of silica glass," *Laser Photonics Rev.* **17**, 2200978 (2023).
182. K.-T. Lin *et al.*, "Structured graphene metamaterial selective absorbers for high efficiency and omnidirectional solar thermal energy conversion," *Nat. Commun.* **11**, 1389 (2020).
183. J. Lin *et al.*, "Laser-induced porous graphene films from commercial polymers," *Nat. Commun.* **5**, 5714 (2014).
184. Z. Wang *et al.*, "Fast-printed, large-area and low-cost terahertz metasurface using laser-induced graphene," *Carbon* **187**, 256 (2022).
185. R. Kuladeep, C. Sahoo, and D. N. Rao, "Direct writing of continuous and discontinuous sub-wavelength periodic surface structures on single-crystalline silicon using femtosecond laser," *Appl. Phys. Lett.* **104**, 222103 (2014).
186. R. Drevinskas *et al.*, "Ultrafast laser-induced metasurfaces for geometric phase manipulation," *Adv. Opt. Mater.* 1 (2016).
187. S. Makarov *et al.*, "Self-adjusted all-dielectric metasurfaces for deep ultraviolet femtosecond pulse generation," *Nanoscale* **8**, 17809 (2016).
188. I. Sakellari *et al.*, "Femtosecond-laser-induced all-silicon dielectric metasurfaces assisted by wet chemical etching," *Ultrafast Sci.* **3**, 0019 (2023).
189. S. Juodkazis *et al.*, "Two-photon lithography of nanorods in SU-8 photoresist," *Nanotechnology* **16**, 846 (2005).
190. X. Wang *et al.*, "Dielectric geometric phase optical elements fabricated by femtosecond direct laser writing in photoresists," *Appl. Phys. Lett.* **110**, 181101 (2017).
191. S. Varapnickas *et al.*, "Birefringent optical retarders from laser 3D-printed dielectric metasurfaces," *Appl. Phys. Lett.* **118**, 151104 (2021).
192. G. E. Lio *et al.*, "Leveraging on ENZ metamaterials to achieve 2D and 3D hyper-resolution in two-photon direct laser writing," *Adv. Mater.* **33**, 2008644 (2021).
193. E. Furlani *et al.*, "Laser writing of multiscale chiral polymer metamaterials," *Adv. OptoElectron.* **2012**, 861569 (2012).
194. F. Ye *et al.*, "Multi-height metasurface for wavefront manipulation fabricated by direct laser writing lithography," *Nanophotonics* **12**, 3435 (2023).
195. G. Roberts *et al.*, "3D-patterned inverse-designed mid-infrared metaoptics," *Nat. Commun.* **14**, 2768 (2023).
196. Y. Liang *et al.*, "Full-stokes polarization perfect absorption with diatomic metasurfaces," *Nano Lett.* **21**, 1090 (2021).
197. Y. Liang *et al.*, "Hybrid anisotropic plasmonic metasurfaces with multiple resonances of focused light beams," *Nano Lett.* **21**, 8917 (2021).
198. A. F. Lasagni *et al.*, "Design of perfectly ordered periodic structures on polymers using direct laser interference patterning," in *Wrinkled Polymer Surfaces: Strategies, Methods and Applications* (2019), 157.
199. J. Chen *et al.*, "Polarization-independent two-dimensional diffraction metal-dielectric grating," *Appl. Phys. Lett.* **113**, 014905 (2018).
200. J.-H. Seo *et al.*, "Large-area printed broadband membrane reflectors by laser interference lithography," *IEEE Photonics J.* **5**, 2200106 (2013).
201. S. M. Kamali *et al.*, "Metasurface-generated complex 3-dimensional optical fields for interference lithography," *Proc. Natl. Acad. Sci. USA* **116**, 21379 (2019).
202. J. De Boor *et al.*, "Sub-100 nm silicon nanowires by laser interference lithography and metal-assisted etching," *Nanotechnology* **21**, 095302 (2010).
203. C. Chen *et al.*, "Large-area, low-cost near-infrared meta-surface reflector based on a pixelated two-dimensional silicon disk array," *Opt. Express* **28**, 38355 (2020).
204. H.-C. Lin *et al.*, "Deep ultraviolet laser direct write for patterning sol-gel InGaZnO semiconducting micro/nanowires and improving field-effect mobility," *Sci. Rep.* **5**, 10490 (2015).
205. L. Huang *et al.*, "Sub-wavelength patterned pulse laser lithography for efficient fabrication of large-area metasurfaces," *Nat. Commun.* **13**, 5823 (2022).
206. D. Bochek *et al.*, "Fabrication of $Ge_2Sb_2Te_5$ metasurfaces by direct laser writing technique," *Opt. Laser Technol.* **141**, 107124 (2021).
207. Z. Wang *et al.*, "4*f*-less terahertz optical pattern recognition enabled by complex amplitude modulating metasurface through laser direct writing," *Adv. Opt. Mater.* 2300575 (2023).
208. X. Lu *et al.*, "Polarization-directed growth of spiral nanostructures by laser direct writing with vector beams," *Nat. Commun.* **14**, 1422 (2023).
209. M. V. Rybin *et al.*, "Transition from two-dimensional photonic crystals to dielectric metasurfaces in the optical diffraction with a fine structure," *Sci. Rep.* **6**, 30773 (2016).
210. A. Zhan *et al.*, "Controlling three-dimensional optical fields via inverse Mie scattering," *Sci. Adv.* **5**, eaax4769 (2019).
211. H. Wei *et al.*, "Two-photon direct laser writing of inverse-designed free-form near-infrared polarization beamsplitter," *Adv. Opt. Mater.* **7**, 1900513 (2019).
212. C. Zhou *et al.*, "All-dielectric fiber meta-tip enabling vortex generation and beam collimation for optical interconnect," *Laser Photon. Rev.* **15**, 2000581 (2021).
213. J. Yang *et al.*, "Photonic crystal fiber metalens," *Nanophotonics* **8**, 443 (2019).
214. M. Plidschun *et al.*, "Fiber-based 3D nano-printed holography with individually phase-engineered remote points," *Sci. Rep.* **12**, 20920 (2022).
215. W. Hadibrata *et al.*, "Inverse design and 3D printing of a metalens on an optical fiber tip for direct laser lithography," *Nano Lett.* **21**, 2422 (2021).

216. I. Faniayeu and V. Mizeikis, "Realization of a helix-based perfect absorber for IR spectral range using the direct laser write technique," *Opt. Mater. Express* **7**, 1453 (2017).
217. J. Zhang *et al.*, "Grayscale-patterned metal-hydrogel-metal microscavity for dynamic multi-color display," *Nanophotonics* **10**, 4125 (2021).
218. Y. Wang *et al.*, "Stepwise-nanocavity-assisted transmissive color filter array microprints," *Research* **2018**, 8109054 (2018).
219. Y. Chen *et al.*, "Centimeter scale color printing with grayscale lithography," *Advanced Photonics Nexus* **1**, 026002 (2022).
220. Y. Hu *et al.*, "3D-integrated metasurfaces for full-colour holography," *Light-Sci. Appl.* **8**, 86 (2019).
221. F. Zhao *et al.*, "Synthetic aperture metalens," *Photonics Res.* **9**, 2388 (2021).
222. R. Guo *et al.*, "Multipolar coupling in hybrid metal–dielectric metasurfaces," *ACS Photonics* **3**, 349 (2016).
223. J. Li *et al.*, "Magnesium-based metasurfaces for dual-function switching between dynamic holography and dynamic color display," *ACS Nano* **14**, 7892 (2020).
224. M. Yoshida *et al.*, "Double-lattice photonic-crystal resonators enabling high-brightness semiconductor lasers with symmetric narrow-divergence beams," *Nat. Mater.* **18**, 121 (2019).
225. J. Li *et al.*, "A reusable metasurface template," *Nano Lett.* **20**, 6845 (2020).
226. A. A. Tseng, A. Notargiacomo, and T. P. Chen, "Nanofabrication by scanning probe microscope lithography: A review," *J. Vacuum Sci. Technol. B* **23**, 877 (2005).
227. A. A. Tseng, A. Notargiacomo, and T. P. Chen, "Nanofabrication by scanning probe microscope lithography: A review," *J. Vacuum Sci. Technol. B* **23**, 877 (2005).
228. Z. Yang *et al.*, "Microscopic interference full-color printing using grayscale-patterned Fabry–Perot resonance cavities," *Adv. Opt. Mater.* **5**, 1700029 (2017).
229. J. Zhu *et al.*, "Grayscale-patterned integrated multilayer-metal-dielectric microcavities for on-chip multi/hyperspectral imaging in the extended visible bandwidth," *Opt. Express* **31**, 14027 (2023).
230. X. Li, Z. J. Tan, and N. X. Fang, "Grayscale stencil lithography for patterning multispectral color filters," *Optica* **7**, 1154 (2020).
231. Y. Chen *et al.*, "Dynamic color displays using stepwise cavity resonators," *Nano Lett.* **17**, 5555 (2017).
232. H. Zheng *et al.*, "Large-scale metasurfaces based on grayscale nanosphere lithography," *ACS Photonics* **8**, 1824 (2021).
233. G. Geng *et al.*, "Height-gradiently-tunable nanostructure arrays by grayscale assembly nanofabrication for ultra-realistic imaging," *Laser Photon. Rev.* **17**, 2300073 (2023).
234. M. Hentschel *et al.*, "Dielectric Mie voids: confining light in air," *Light-Sci. Appl.* **12**, 3 (2023).
235. S. Shi *et al.*, "Asymmetric nanocavities with wide reflection color gamut for color printing," *Nanotechnology* **34**, 025201 (2022).
236. H. Wang *et al.*, "Full color and grayscale painting with 3D printed low-index nanopillars," *Nano Lett.* **21**, 4721 (2021).
237. C. Williams *et al.*, "Grayscale-to-color: scalable fabrication of custom multispectral filter arrays," *ACS Photonics* **6**, 3132 (2019).
238. J. Lu *et al.*, "A versatile metasurface enabling superwettability for self-cleaning and dynamic color response," *Adv. Opt. Mater.* **10**, 2101781 (2022).
239. R. Garcia, A. W. Knoll, and E. Riedo,"Advanced scanning probe lithography," *Nat. Nanotechnol.* **9**, 577 (2014).
240. Y. Lisunova *et al.*, "High-aspect ratio nanopatterning via combined thermal scanning probe lithography and dry etching," *Microelectron. Eng.* **180**, 20 (2017).
241. W. Zhang *et al.*, "Fabrication of a VO_2-based tunable metasurface by electric-field scanning probe lithography with precise depth control," *ACS Appl. Mater. Interfaces* **15**, 13517 (2023).
242. S. T. Howell *et al.*, "Thermal scanning probe lithography—a review," *Microsyst. Nanoeng.* **6**, 21 (2020).
243. J. Seong *et al.*, "Cost-effective and environmentally friendly mass manufacturing of optical metasurfaces towards practical applications and commercialization," *Int. J. Precision Eng. Manuf. Green Technol.* **11**, 685 (2023).
244. N. Li *et al.*, "Large-area metasurface on CMOS-compatible fabrication platform: driving flat optics from lab to fab," *Nanophotonics* **9**, 3071 (2020).
245. V. J. Gómez *et al.*, "Wafer-scale nanofabrication of sub-100 nm arrays by deep-UV displacement Talbot lithography," *Nanotechnology* **31**, 295301 (2020).
246. S. Ansaryan *et al.*, "High-throughput spatiotemporal monitoring of single-cell secretions via plasmonic microwell arrays," *Nat. Biomed. Eng.* **7**, 943 (2023).
247. M. Keil *et al.*, "Large plasmonic color metasurfaces fabricated by super resolution deep UV lithography," *Nanoscale Adv.* **3**, 2236 (2021).
248. T. Hu *et al.*, "Demonstration of color display metasurfaces via immersion lithography on a 12-inch silicon wafer," *Opt. Express* **26**, 19548 (2018).
249. A. Belushkin *et al.*, "Rapid and digital detection of inflammatory biomarkers enabled by a novel portable nanoplasmonic imager," *Small* **16**, 1906108 (2020).
250. Y.-C. Liu *et al.*, "Real-time monitoring of single-cell secretion with a high-throughput nanoplasmonic microarray," *Biosens. Bioelectron.* **202**, 113955 (2022).
251. S. W. Moon *et al.*, "Wafer-scale manufacturing of near-infrared metalenses," *Laser Photonics Rev.* 2300929 (2024).
252. G. Prone *et al.*, "Scalable, nanometer-accurate fabrication of all-dielectric metasurfaces with narrow resonances tunable from near infrared to visible wavelengths," *Adv. Photonics Res.* **3**, 2200014 (2022).
253. K. Kim *et al.*, "Facile nanocasting of dielectric metasurfaces with sub-100 nm resolution," *ACS Appl. Mater. Interfaces* **11**, 26109 (2019).
254. A. M. Baracu *et al.*, "Silicon metalens fabrication from electron beam to UV-nanoimprint lithography," *Nanomaterials* **11**, 2329 (2021).
255. M. Song *et al.*, "Versatile full-colour nanopainting enabled by a pixelated plasmonic metasurface," *Nat. Nanotechnol.* **18**, 71 (2023).
256. H. Kang *et al.*, "Emerging low-cost, large-scale photonic platforms with soft lithography and self-assembly," *Photonics Insights* **2**, R04 (2023).
257. J. Kim *et al.*, "8″ wafer-scale, centimeter-sized, high-efficiency metalenses in the ultraviolet," *Mater. Today* **73**, 9 (2024).
258. J. Kim *et al.*, "Scalable manufacturing of high-index atomic layer–polymer hybrid metasurfaces for metaphotonics in the visible," *Nat. Mater.* **22**, 474 (2023).
259. Y. Huang *et al.*, "Wafer-scale self-assembled 2.5D metasurface for efficient near-field and far-field electromagnetic manipulation," *Appl. Surf. Sci.* **601**, 154244 (2022).
260. J. Jiang *et al.*, "Colloidal self-assembly based ultrathin metasurface for perfect absorption across the entire visible spectrum," *Nanophotonics* **12**, 1581 (2023).
261. A. Bonakdar *et al.*, "High-throughput realization of an infrared selective absorber/emitter by DUV microsphere projection lithography," *Nanotechnology* **27**, 035301 (2015).
262. C. Qu and E. C. Kinzel, "Polycrystalline metasurface perfect absorbers fabricated using microsphere photolithography," *Opt. Lett.* **41**, 3399 (2016).
263. X. Yang *et al.*, "Phase-transition microcavity laser," *Nano Lett.* **23**, 3048 (2023).
264. Y. Zhai *et al.*, "Scalable-manufactured randomized glass-polymer hybrid metamaterial for daytime radiative cooling," *Science* **355**, 1062 (2017).
265. A. Agreda *et al.*, "Tailoring iridescent visual appearance with disordered resonant metasurfaces," *ACS Nano* **17**, 6362 (2023).

266. B. Fay, "Advanced optical lithography development, from UV to EUV," *Microelectron. Eng.* **61**, 11 (2002).
267. A. She *et al.*, "Large area metalenses: design, characterization, and mass manufacturing," *Opt. Express* **26**, 1573 (2018).
268. J.-S. Park *et al.*, "All-glass, large metalens at visible wavelength using deep-ultraviolet projection lithography," *Nano Lett.* **19**, 8673 (2019).
269. A. Leitis *et al.*, "Wafer-scale functional metasurfaces for mid-infrared photonics and biosensing," *Adv. Mater.* **33**, 2102232 (2021).
270. Z. Xu *et al.*, "CMOS-compatible all-Si metasurface polarizing bandpass filters on 12-inch wafers," *Opt. Express* **27**, 26060 (2019).
271. Z. Xu *et al.*, "Metasurface-based subtractive color filter fabricated on a 12-inch glass wafer using a CMOS platform," *Photonics Res.* **9**, 13 (2021).
272. T. Hu *et al.*, "CMOS-compatible a-Si metalenses on a 12-inch glass wafer for fingerprint imaging," *Nanophotonics* **9**, 823 (2020).
273. H. Schift *et al.*, "Nanoimprint lithography process chains for the fabrication of micro-and nanodevices," *J. Micro/Nanolithogr. MEMS MOEMS* **13**, 031303 (2014).
274. D. K. Oh *et al.*, "Nanoimprint lithography for high-throughput fabrication of metasurfaces," *Front. Optoelectron.* **14**, 229 (2021).
275. X. Cheng and L. J. Guo, "One-step lithography for various size patterns with a hybrid mask-mold," *Microelectron. Eng.* **71**, 288 (2004).
276. M. K. Chen *et al.*, "Chiral-magic angle of nanoimprint meta-device," *Nanophotonics* **12**, 2479 (2023).
277. V. Bhingardive, L. Menahem, and M. Schvartzman, "Soft thermal nanoimprint lithography using a nanocomposite mold," *Nano Res.* **11**, 2705 (2018).
278. J. K. Kim *et al.*, "Effect of surface tension and coefficient of thermal expansion in 30 nm scale nanoimprinting with two flexible polymer molds," *Nanotechnology* **23**, 235303 (2012).
279. Y. Yao and W. Wu, "All-dielectric heterogeneous metasurface as an efficient ultra-broadband reflector," *Adv. Opt. Mater.* **5**, 1700090 (2017).
280. X. Cao *et al.*, "Tuning metasurface dimensions by soft nanoimprint lithography and reactive ion etching," *Adv. Photon. Res.* **3**, 2200127 (2022).
281. G. Yoon *et al.*, "Single-step manufacturing of hierarchical dielectric metalens in the visible," *Nat. Commun.* **11**, 2268 (2020).
282. H. Choi *et al.*, "Realization of high aspect ratio metalenses by facile nanoimprint lithography using water-soluble stamps," *PhotoniX* **4**, 1 (2023).
283. D. Quan *et al.*, "Dielectric metalens by multilayer nanoimprint lithography and solution phase epitaxy," *Adv. Eng. Mater.* **25**, 2201824 (2023).
284. J. M. Lehn, "Perspectives in supramolecular chemistry—from molecular recognition towards molecular information processing and self-organization," *Angew. Chem. Int. Ed. Engl.* **29**, 1304 (1990).
285. G. Zhang *et al.*, "Flexible, all-dielectric metasurface fabricated via nanosphere lithography and its applications in sensing," *Opt. Express* **25**, 22038 (2017).
286. T. Das Gupta *et al.*, "Self-assembly of nanostructured glass metasurfaces via templated fluid instabilities," *Nat. Nanotechnol.* **14**, 320 (2019).
287. B. Du *et al.*, "Large-area all-dielectric metasurface fabricated by an anodized aluminum oxide template," *Opt. Express* **29**, 10465 (2021).
288. A. A. Kulkarni and G. S. Doerk, "Hierarchical, self-assembled metasurfaces via exposure-controlled reflow of block copolymer-derived nanopatterns," *ACS Appl. Mater. Interfaces* **14**, 27466 (2022).
289. D. Andrén *et al.*, "Large-scale metasurfaces made by an exposed resist," *ACS Photonics* **7**, 885 (2020).
290. Y. S. Tan *et al.*, "High-throughput fabrication of large-scale metasurfaces using electron-beam lithography with SU-8 gratings for multilevel security printing," *Photonics Res.* **11**, B103 (2023).
291. G. Marino *et al.*, "Harmonic generation with multi-layer dielectric metasurfaces," *Nanophotonics* **10**, 1837 (2021).
292. D. Ray *et al.*, "Hybrid metal-dielectric metasurfaces for refractive index sensing," *Nano Lett.* **20**, 8752 (2020).
293. E. Mavrona *et al.*, "Refractive index measurement of IP-S and IP-Dip photoresists at THz frequencies and validation via 3D photonic metamaterials made by direct laser writing," *Opt. Mater. Express* **13**, 3355 (2023).
294. Y. Yang *et al.*, "Graphene-based multilayered metamaterials with phototunable architecture for on-chip photonic devices," *ACS Photonics* **6**, 1033 (2019).
295. J. C. Zhang *et al.*, "Miniature tunable Airy beam optical meta-device," *Opto-Electron. Adv.* **7**, 230171-1 (2024).
296. S. Walia *et al.*, "Flexible metasurfaces and metamaterials: A review of materials and fabrication processes at micro-and nano-scales," *Appl. Phys. Rev.* **2**, 011303 (2015).
297. M. L. Tseng *et al.*, "Two-dimensional active tuning of an aluminum plasmonic array for full-spectrum response," *Nano Lett.* **17**, 6034 (2017).
298. H. Lin *et al.*, "A 90-nm-thick graphene metamaterial for strong and extremely broadband absorption of unpolarized light," *Nat. Photonics* **13**, 270 (2019).
299. N. Kim *et al.*, "Highly angle-sensitive and efficient optical metasurfaces with broken mirror symmetry," *Nanophotonics* **12**, 2347 (2023).
300. K. Ventola *et al.*, "High phase retardation by waveguiding in slanted photonic nanostructures," *Opt. Express* **19**, 241 (2011).
301. Y. Yao *et al.*, "High-aspect-ratio silicon metasurfaces: design, fabrication, and characterization," *Appl. Sci.* **13**, 9607 (2023).
302. Q. Gu *et al.*, "High aspect ratio metamaterials and their applications," *Sensor Actutuators A* **335**, 113376 (2022).
303. K. Tanaka *et al.*, "Chiral bilayer all-dielectric metasurfaces," *ACS Nano* **14**, 15926 (2020).
304. F. Balli *et al.*, "A hybrid achromatic metalens," *Nat. Commun.* **11**, 3892 (2020).
305. C.-F. Pan *et al.*, "3D-printed multilayer structures for high–numerical aperture achromatic metalenses," *Sci. Adv.* **9**, eadj9262 (2023).
306. C. Roques-Carmes *et al.*, "Toward 3D-printed inverse-designed metaoptics," *ACS Photonics* **9**, 43 (2022).
307. Y. Zhou *et al.*, "Multilayer noninteracting dielectric metasurfaces for multiwavelength metaoptics," *Nano Lett.* **18**, 7529 (2018).
308. C. Zhang *et al.*, "Stretchable all-dielectric metasurfaces with polarization-insensitive and full-spectrum response," *ACS Nano* **14**, 1418 (2019).
309. S. M. Kamali *et al.*, "Highly tunable elastic dielectric metasurface lenses," *Laser Photon. Rev.* **10**, 1002 (2016).
310. V. J. Einck *et al.*, "Scalable nanoimprint lithography process for manufacturing visible metasurfaces composed of high aspect ratio TiO_2 meta-atoms," *ACS Photonics* **8**, 2400 (2021).
311. S. W. D. Lim *et al.*, "A high aspect ratio inverse-designed holey metalens," *Nano Lett.* **21**, 8642 (2021).
312. Z. Wang *et al.*, "Bifunctional manipulation of terahertz waves with high-efficiency transmissive dielectric metasurfaces," *Adv. Sci.* **10**, 2205499 (2023).
313. W. Liu *et al.*, "Metasurface enabled wide-angle Fourier lens," *Adv. Mater.* **30**, 1706368 (2018).
314. M. Khorasaninejad *et al.*, "Multispectral chiral imaging with a metalens," *Nano Lett.* **16**, 4595 (2016).
315. Q. Guo *et al.*, "Compact single-shot metalens depth sensors inspired by eyes of jumping spiders," *Proc. Natl. Acad. Sci. USA* **116**, 22959 (2019).

316. J. Zhou *et al.*, "Optical edge detection based on high-efficiency dielectric metasurface," *Proc. Natl. Acad. Sci. USA* **116**, 11137 (2019).
317. F. Zangeneh-Nejad and A. Khavasi, "Spatial integration by a dielectric slab and its planar graphene-based counterpart," *Opt. Lett.* **42**, 1954 (2017).
318. X. Liu *et al.*, "Meta-lens particle image velocimetry," *Adv. Mater.* 2310134 (2023).
319. H. Kwon *et al.*, "Single-shot quantitative phase gradient microscopy using a system of multifunctional metasurfaces," *Nat. Photonics* **14**, 109 (2020).
320. H. Zang *et al.*, "Ultrasensitive and long-range transverse displacement metrology with polarization-encoded metasurface," *Sci. Adv.* **8**, eadd1973 (2022).
321. S. Li *et al.*, "Efficient optical angular momentum manipulation for compact multiplexing and demultiplexing using a dielectric metasurface," *Adv. Opt. Mater.* **8**, 1901666 (2020).
322. Z. Hu *et al.*, "Ultrawide bandgap AlN metasurfaces for ultraviolet focusing and routing," *Opt. Lett.* **45**, 3466 (2020).
323. Y. Fan *et al.*, "Resonance-enhanced three-photon luminesce via lead halide perovskite metasurfaces for optical encoding," *Nat. Commun.* **10**, 2085 (2019).
324. L. Zhang *et al.*, "High-efficiency, 80 mm aperture metalens telescope," *Nano Lett.* **23**, 51 (2022).
325. P. Chakravarthula *et al.*, "Thin on-sensor nanophotonic array cameras," *ACM Trans. Graph.* **42**, 1 (2023).
326. Q. Ma *et al.*, "Information metasurfaces and intelligent metasurfaces," *Photonics Insights* **1**, R01 (2022).
327. Y. Guo *et al.*, "Classical and generalized geometric phase in electromagnetic metasurfaces," *Photonics Insights* **1**, R03 (2022).
328. T. Li *et al.*, "Revolutionary meta-imaging: from superlens to metalens," *Photon. Insights* **2**, R01 (2023).
329. Q. Zhang *et al.*, "Diffractive optical elements 75 years on: from micro-optics to metasurfaces," *Photonics Insights* **2**, R09 (2023).
330. M. K. Chen *et al.*, "Meta-lens in the sky," *IEEE Access* **10**, 46552 (2022).
331. M. K. Chen *et al.*, "A meta-device for intelligent depth perception," *Adv. Mater.* **35**, 2107465 (2023).
332. X. Liu *et al.*, "Underwater binocular meta-lens," *ACS Photonics* **10**, 2382 (2023).
333. G.-Y. Lee *et al.*, "Metasurface eyepiece for augmented reality," *Nat. Commun.* **9**, 4562 (2018).
334. J. Zhou *et al.*, "Two-dimensional optical spatial differentiation and high-contrast imaging," *Natl. Sci. Rev.* **8**, nwaa176 (2021).
335. I. Tanriover, S. A. Dereshgi, and K. Aydin, "Metasurface enabled broadband all optical edge detection in visible frequencies," *Nat. Commun.* **14**, 6484 (2023).
336. A. Komar *et al.*, "Edge detection with Mie-resonant dielectric metasurfaces," *ACS Photonics* **8**, 864 (2021).
337. A. Cordaro *et al.*, "High-index dielectric metasurfaces performing mathematical operations," *Nano Lett.* **19**, 8418 (2019).
338. J. Zhou *et al.*, "Metasurface enabled quantum edge detection," *Sci. Adv.* **6**, eabc4385 (2020).
339. S. Abdollahramezani *et al.*, "Electrically driven reprogrammable phase-change metasurface reaching 80% efficiency," *Nat. Commun.* **13**, 1696 (2022).
340. A. Tripathi *et al.*, "Tunable Mie-resonant dielectric metasurfaces based on VO_2 phase-transition materials," *ACS Photonics* **8**, 1206 (2021).
341. X. Sha *et al.*, "Chirality tuning and reversing with resonant phase-change metasurfaces," *Sci. Adv.* **10**, eadn9017 (2024).
342. H. Weigand *et al.*, "Enhanced electro-optic modulation in resonant metasurfaces of lithium niobate," *ACS Photonics* **8**, 3004 (2021).
343. Y. Liu *et al.*, "On-chip electrically driven tunable meta-lens for dynamic focusing and beam steering," *Laser Photonics Rev.* **17**, 2300330 (2023).
344. A. Komar *et al.*, "Electrically tunable all-dielectric optical metasurfaces based on liquid crystals," *Appl. Phys. Lett.* **110**, 071109 (2017).
345. H. C. Weigand *et al.*, "Nanoimprinting solution-derived barium titanate for electro-optic metasurfaces," *Nano Lett.* **24**, 5536 (2024).
346. Y. Yao *et al.*, "Electrically tunable metasurface perfect absorbers for ultrathin mid-infrared optical modulators," *Nano Lett.* **14**, 6526 (2014).
347. P. Chen *et al.*, "Optical properties of quasi-tetragonal $BiFeO_3$ thin films," *Appl. Phys. Lett.* **96**, 131907 (2010).
348. D. M. Krichevsky *et al.*, "Silicon-based all-dielectric metasurface on an iron garnet film for efficient magneto-optical light modulation in near IR range," *Nanomaterials* **11**, 2926 (2021).
349. J. Zhou *et al.*, "Nonlinear computational edge detection metalens," *Adv. Funct. Mater.* **32**, 2204734 (2022).
350. J. Zhou *et al.*, "Kerr metasurface enabled by metallic quantum wells," *Nano Lett.* **21**, 330 (2020).
351. J. Lee *et al.*, "Giant nonlinear response from plasmonic metasurfaces coupled to intersubband transitions," *Nature* **511**, 65 (2014).
352. I. Kim *et al.*, "Pixelated bifunctional metasurface-driven dynamic vectorial holographic color prints for photonic security platform," *Nat. Commun.* **12**, 3614 (2021).
353. X. Ou *et al.*, "Tunable polarization-multiplexed achromatic dielectric metalens," *Nano Lett.* **22**, 10049 (2022).
354. P. P. Iyer *et al.*, "Uniform thermo-optic tunability of dielectric metalenses," *Phys. Rev. Appl.* **10**, 044029 (2018).
355. M. Bosch *et al.*, "Electrically actuated varifocal lens based on liquid-crystal-embedded dielectric metasurfaces," *Nano Lett.* **21**, 3849 (2021).
356. A. Komar *et al.*, "Dynamic beam switching by liquid crystal tunable dielectric metasurfaces," *ACS Photonics* **5**, 1742 (2018).
357. Y. Xie *et al.*, "Giant enhancement of second-harmonic generation in hybrid metasurface coupled MoS_2 with Fano-resonance effect," *Nanoscale Res. Lett.* **17**, 97 (2022).
358. S. Abdollahramezani *et al.*, "Dynamic hybrid metasurfaces," *Nano Lett.* **21**, 1238 (2021).
359. Z. Li *et al.*, "Hybrid metasurface-based mid-infrared biosensor for simultaneous quantification and identification of monolayer protein," *ACS Photonics* **6**, 501 (2019).
360. Y. Zhu *et al.*, "Optical conductivity-based ultrasensitive mid-infrared biosensing on a hybrid metasurface," *Light Sci. Appl.* **7**, 67 (2018).
361. J. King *et al.*, "Electrically tunable VO_2–metal metasurface for mid-infrared switching, limiting and nonlinear isolation," *Nat. Photonics* **18**, 74 (2024).
362. S.-Q. Li *et al.*, "Phase-only transmissive spatial light modulator based on tunable dielectric metasurface," *Science* **364**, 1087 (2019).
363. Q. Li *et al.*, "Metasurface optofluidics for dynamic control of light fields," *Nat. Nanotechnol.* **17**, 1097 (2022).
364. Q. Ma *et al.*, "Smart metasurface with self-adaptively reprogrammable functions," *Light Sci. Appl.* **8**, 98 (2019).